

Advances in EP and ERP signal processing

ADVANCES IN EP AND ERP SIGNAL PROCESSING

BY

PHILIP CHRAPKA, B.Eng.

A THESIS

SUBMITTED TO THE DEPARTMENT OF ELECTRICAL & COMPUTER ENGINEERING

AND THE SCHOOL OF GRADUATE STUDIES

OF MCMASTER UNIVERSITY

IN PARTIAL FULFILMENT OF THE REQUIREMENTS

FOR THE DEGREE OF

DOCTOR OF PHILOSOPHY

© Copyright by Philip Chrapka, February 9, 2018

All Rights Reserved

Doctor of Philosophy (2018)
(Electrical & Computer Engineering)

McMaster University
Hamilton, Ontario, Canada

TITLE: Advances in EP and ERP signal processing

AUTHOR: Philip Chrapka
B.Eng., (Electrical and Biomedical Engineering)
McMaster University, Hamilton, Canada

SUPERVISOR: Dr. Hubert de Bruin and Dr. Jim Reilly

NUMBER OF PAGES: xviii, 139

*To my wife, Joanna,
and my parents, Kazimierz and Wiesława*

Abstract

Our understanding of brain function is still very limited. Much research is being conducted to further our understanding and develop new treatments, diagnostics and devices that not only could be more effective in helping us deal with neurological and psychiatric disorders and rehabilitation, but also make cognitive enhancement possible. However, none of this is possible without signal processing capabilities to extract information from electroencephalography (EEG) signals and especially event related potentials (ERPs) and evoked potentials (EPs).

This thesis presents new developments in EP artifact rejection, ERP brain source localization and dynamic causal brain network estimation during an ERP.

Chapter 2 presents a new method for reducing contamination from compound muscle action potentials (CMAPs) recorded along with EEG activity during repetitive transcranial magnetic stimulation (rTMS). This development improves the visibility of short latency cortical activity as a result of rTMS.

In the application of brain source localization methods, especially beamforming, head modelling errors can cause significant performance degradation. The robust minimum variance beamformer (RMVB) developed in Chapter 3 improves beamformer performance relative to the MVB and its regularized and eigenspace variations in the face of these head modelling errors. The RMVB specifically optimizes for the

worst-case estimate of the uncertainty.

Lastly, Chapter 4 describes the Adaptive Sparse ERP Tracking (ASET) algorithm for estimating dynamic and causal networks that are involved in processing ERPs. The ASET algorithm is applied to investigate the dynamics in auditory processing, specifically resulting from the β -band and its envelope.

Acknowledgements

First and foremost, I would like to thank Dr. Hubert de Bruin and Dr. Jim Reilly for all their support during graduate school. I am extremely grateful for their advice, encouragement, enthusiasm and patience in my scholarly pursuit.

Thank you to my committee, Dr. John Connolly, Dr. Thia Kirubarajan, and Dr. Laurel Trainor for their insights and suggestions regarding my thesis research. I would like to thank Richard Mah, Dr. John Connolly, Andrew Chang, Dr. Laurel Trainor and Dr. Gary Hasey for sharing their unique and interesting EEG data sets where I could apply my new algorithms as well as taking the time to define and explore useful applications of my thesis research.

I would like to thank the administrative team in the Department of Electrical and Computer Engineering, and specifically show my appreciation for Cheryl Gies for all her assistance throughout my years at McMaster University. I also would like to express my gratitude to my friends and colleagues at McMaster University for sharing their ideas, work and helping me get through my studies.

Thanks to my parents, siblings and cousins for their constant encouragement and support. I want to specifically thank my parents for teaching me to strive for more and to persevere. Last and most importantly, thank you to my wife, Joanna, for her seemingly infinite patience, support, and love.

Notation and abbreviations

| | |
|-------|---|
| AAL | Automated Anatomical Labelling |
| AC | Auditory Cortex |
| ADHD | Attention Deficit Hyperactivity Disorder |
| AIC | Akaike Information Criterion |
| AR | Autoregressive |
| ASET | Adaptive Sparse ERP Tracking |
| BCI | Brain Computer Interfaces |
| BEM | Boundary Element Method |
| BSL | Brain Source Localization |
| CMAP | Compound Muscle Action Potential |
| DLPFC | Dorsolateral Prefrontal Cortex |
| DTF | Directed Transfer Function |
| DWT | Discrete Wavelet Transform |
| ECoG | Electrocorticography |
| EEG | Electroencephalography |
| EPs | Evoked Potentials |
| ERPs | Event-related Potentials |
| EWAIC | Exponentially-Weighted Akaike Information Criterion |

| | |
|-----------|---------------------------------------|
| fMRI | Functional Magnetic Resonance Imaging |
| GMFA | Global Mean Field Average |
| gPDC | Generalized PDC |
| ICA | Independent Component Analysis |
| IT | Inferior Temporal |
| LCMV | Linearly Constrained Minimum Variance |
| LSL | Least-squares Lattice |
| MC | Motor Cortex |
| MCMTQRDSL | Multi-channel Multi-trial QRDSL |
| MDD | Major Depressive Disorder |
| MEG | Magnetoencephalography |
| MNI | Montreal Neurological Institute |
| MQRDSL | Multi-channel QRDSL |
| MRI | Magnetic Resonance Imaging |
| MSE | Mean Squared Error |
| MVB | Minimum Variance Beamforming |
| NIBS | Non-invasive Brain Stimulation |
| OC | Occipital Cortex |
| OCDD | Online Cyclic Coordinate Descent |
| OD | Online Coordinate Descent |
| PC | Parietal Cortex |
| PCA | Principal Component Analysis |
| PDC | Partial Directed Coherence |
| PET | Positron Emission Tomography |

| | |
|-------|---|
| PFC | Prefrontal Cortex |
| PPC | Posterior Parietal Cortex |
| RCs | Reflection Coefficients |
| RLS | Recursive Least Squares |
| RMS | Root Mean Square |
| RMSE | Root-mean-squared Error |
| RMVB | Robust Minimum Variance Beamformer |
| SINR | Signal-to-interference-plus-noise-ratio |
| SNR | Signal-to-noise Ratio |
| ST | Superior Temporal |
| TC | Temporal Cortex |
| tDCS | Transcranial Direct Current Stimulation |
| TMS | Transcranial Magnetic Stimulation |
| tvVAR | Time-varying VAR |
| VAR | Vector Autoregressive |
| VLPFC | Ventrolateral Prefrontal Cortex |
| WMN | Weighted Minimum Norm |

Contents

| | |
|---|------------|
| Abstract | iv |
| Acknowledgements | vi |
| Notation and abbreviations | vii |
| 1 Introduction | 1 |
| 1.1 Electroencephalography (EEG) | 2 |
| 1.2 Evoked and event-related potentials | 4 |
| 1.3 Averaging and artifacts | 5 |
| 1.4 Brain source localization | 6 |
| 1.5 Brain connectivity estimation | 8 |
| 1.6 Organization of thesis | 8 |
| 2 Wavelet-based Muscle Artifact Noise Reduction for Short Latency rTMS Evoked Potentials | 11 |
| 2.1 Introduction | 11 |
| 2.2 Materials and Methods | 15 |
| 2.2.1 Subjects | 15 |

| | | |
|-------|--------------------------|----|
| 2.2.2 | Stimulation | 15 |
| 2.2.3 | EEG Recording | 16 |
| 2.2.4 | EEG Processing | 16 |
| 2.3 | Results | 22 |
| 2.3.1 | Simulation | 22 |
| 2.3.2 | Real Data | 24 |
| 2.4 | Discussion | 30 |
| 2.5 | Conclusions | 34 |

3 Estimating Neural Sources Using a Worst-case Robust Adaptive Beamforming Approach 35

| | | |
|-------|--|----|
| 3.1 | Introduction | 35 |
| 3.2 | Background | 38 |
| 3.3 | Robust Minimum Variance Beamformer | 41 |
| 3.3.1 | Reformulation | 41 |
| 3.3.2 | Bound on the Error Matrix | 44 |
| 3.3.3 | Standard Convex Reformulation | 45 |
| 3.3.4 | Uncertainty Models | 47 |
| 3.4 | Simulations | 50 |
| 3.4.1 | Comparative Algorithms | 53 |
| 3.5 | Experiments | 54 |
| 3.5.1 | Results for the Matched Head Model | 55 |
| 3.5.2 | Mismatched Head Model | 59 |
| 3.6 | Discussion | 67 |
| 3.7 | Conclusion | 71 |

| | | |
|----------|--|-----------|
| 4 | Sparse Dynamic Causal Network Estimation for Event-Related Potentials | 73 |
| 4.1 | Introduction | 73 |
| 4.2 | Background | 77 |
| 4.2.1 | Partial Directed Coherence | 77 |
| 4.2.2 | Reflection Coefficients and Lattice Filters | 78 |
| 4.3 | Adaptive Sparse ERP Tracking (ASET) Algorithm | 80 |
| 4.3.1 | Update equations | 82 |
| 4.3.2 | Online coordinate descent | 83 |
| 4.3.3 | Online cyclic coordinate descent | 85 |
| 4.3.4 | Time-Varying gPDC | 85 |
| 4.3.5 | Parameter Selection | 86 |
| 4.3.6 | Beamforming | 87 |
| 4.4 | Simulations | 90 |
| 4.4.1 | Reflection Coefficient MSE | 91 |
| 4.4.2 | Reflection Coefficient Sparsity | 91 |
| 4.5 | Surrogate Data Analysis | 93 |
| 4.5.1 | Null hypothesis: No coupling | 94 |
| 4.6 | Application | 97 |
| 4.6.1 | Background | 97 |
| 4.6.2 | Methods | 97 |
| 4.6.3 | Anatomical Segmentation | 98 |
| 4.6.4 | Dynamic Connectivity Estimation | 99 |
| 4.6.5 | Results | 101 |

| | | |
|----------|---|------------|
| 4.6.6 | Discussion | 114 |
| 4.7 | Conclusion | 115 |
| 5 | Future Work | 117 |
| 5.1 | rTMS Muscle Artifact Reduction | 117 |
| 5.2 | Robust Beamforming | 118 |
| 5.3 | Dynamic Connectivity Estimation | 119 |
| 6 | Conclusion | 121 |

List of Figures

| | | |
|-----|--|----|
| 2.1 | Average response for 80 stimuli at Broadmann area 10 for a 33 year old male, with data bandpass filtered from 25 to 2000 Hz. | 21 |
| 2.2 | Response to 80 pulses at 10Hz to left B46 for a 21 year old female subject. | 23 |
| 2.3 | Residual from denoising simulated EEG contaminated by an electrically stimulated CMAP using wavelet denoising and digital filtering. . | 24 |
| 2.4 | Comparison of root-mean-squared error (RMSE) in recovering the original simulated EEG signal for digital filtering and the proposed method. | 25 |
| 2.5 | Residual after applying wavelet denoising and digital filtering to the data shown in Figure 2.2. | 26 |
| 2.6 | Residual of wavelet denoising with various mother wavelets (from top: Daubechies 4, Biorthogonal 1.3, Coiflet 2, Coiflet 3) and digital filtering at C3. Original data is shown in Figure 2.2. | 27 |
| 2.7 | Residual of wavelet denoising with various mother wavelets. Original data is shown in Figure 2.2. | 28 |
| 2.8 | Average GMFA over the 5-30 ms interval of residual responses to 10 Hz stimulation at left B46, B09, B10 of the 21 year old female subject. | 29 |

| | | |
|-----|---|----|
| 2.9 | Average GMFA over the 5-30 ms interval of residual responses to 10 Hz stimulation at left B46, B09, B10 for all subjects and processed using wavelet noise reduction with the db4 mother wavelet. | 30 |
| 3.1 | Simulated EEG with a SNR of -15dB, shown as the superposition of all 256 channels. | 52 |
| 3.2 | Performance of various types of beamformer for the matched head model experiment at the location of d_s | 56 |
| 3.3 | Beampatterns for the matched model scenario with an input SNR of -5dB, with respect to dipole d_s . \bullet and \blacksquare mark the locations of dipoles d_s and d_i , respectively. | 57 |
| 3.4 | Beamformer performance for the mismatched head models experiment at the location of d_s | 60 |
| 3.5 | Localization plots over the time interval of 436.4-676.7ms for the mismatched model scenario. The input SNR is -5dB. | 61 |
| 3.6 | Average beamformer output power over the time interval of 436.4-676.7ms for varying degrees of isotropic uncertainty, $\epsilon = 100, 150$ and 200. The input SNR is -5dB. | 62 |
| 3.7 | Beampatterns for the mismatched model scenario, with respect to dipole d_s . The input SNR is -5dB. | 65 |
| 3.8 | Beampatterns for the mismatched model scenario, with respect to dipole \mathbf{d}_s with varying degrees of isotropic uncertainty, $\epsilon = 50, 100, 150$ and 200. The input SNR is -5dB. | 66 |
| 4.1 | Average MSE performance of the ASET algorithm vs. QRD-based methods | 92 |

| | | |
|-----|---|-----|
| 4.2 | Average steady-state MSE performance of filters as a function of reflection coefficient sparsity. | 93 |
| 4.3 | Histogram of cross-channel gPDC values under the null hypothesis for 100 realizations of surrogate data when $t = 367\text{ms}$ and for frequencies between 0-10Hz. The number of elements is represented by a color map, where the hotter color represents a higher number. The resulting thresholds for each frequency are marked by \times . The anatomical region pairs and time sample were selected based on the largest threshold. . | 96 |
| 4.4 | Comparison of gPDC (4.4a) and thresholded gPDC ($\alpha = 0.05$) (4.4b) flows to the left auditory cortex corresponding to the β -band activity itself, with parameters $H = 20$, model order 6, $\gamma = 1e-5$ and $\lambda = 0.99$. Each horizontal band represents the gPDC between 15-25Hz (oriented from top to bottom) and across time -250ms to 1000ms. The magnitude of the gPDC is defined by the intensity of the color. The dashed lines mark the stimulus onset. | 102 |
| 4.5 | Same as Figure 4.4 except $H = 100$ | 103 |
| 4.6 | Mean and ± 1 standard deviation of gPDC flows from the left Temporal Cortex to the left Auditory Cortex at $t = 781\text{ms}$, corresponding to Figure 4.4 and Figure 4.5, in comparison with the thresholds produced by surrogate analysis with the “no coupling” null hypothesis. . | 105 |

| | | |
|-----|---|-----|
| 4.7 | Comparison of gPDC (4.7a) and thresholded gPDC ($\alpha = 0.05$) (4.7b) flows to the left temporal cortex for the β -band envelope, with parameters $H = 100$, model order 5, $\gamma = 1e - 5$ and $\lambda = 0.99$. Each horizontal band represents the gPDC between 0-10Hz (oriented from top to bottom) and across time -250ms to 1000ms. The magnitude of the gPDC is defined by the intensity of the color. The dashed lines mark the stimulus onset. | 106 |
| 4.8 | Comparison of gPDC (4.8a) and thresholded gPDC ($\alpha = 0.05$) (4.8b) flows to the left temporal cortex for the β -band envelope, with parameters $H = 195$, model order 5, $\gamma = 1e - 5$ and $\lambda = 0.99$. Each horizontal band represents the gPDC between 0-10Hz (oriented from top to bottom) and across time -250ms to 1000ms. The magnitude of the gPDC is defined by the intensity of the color. The dashed lines mark the stimulus onset. | 107 |
| 4.9 | Threshold for gPDC flows to the left temporal cortex (TC) for $H = 100$ with respect to the “no coupling” null hypothesis. Each horizontal band represents the gPDC between 0-10Hz (oriented from top to bottom) and across time -250ms to 1000ms. The magnitude of the gPDC is defined by the intensity of the color. The dashed lines mark the stimulus onset. | 108 |

| | | |
|------|--|-----|
| 4.10 | Standard deviation of gPDC flows to the left temporal cortex (TC) for $H = 100$. The standard deviation is computed from 100 runs of the ASET algorithm using a different permutation of ERP trials for each run. Each horizontal band represents the gPDC between 0-10Hz (oriented from top to bottom) and across time -250ms to 1000ms. The magnitude of the gPDC is defined by the intensity of the color. The dashed lines mark the stimulus onset. | 109 |
| 4.11 | Mean and +/- 1 standard deviation of gPDC flows for $H = 100$ from the left Auditory Cortex to the left Temporal Cortex at $t = 781$ ms in comparison with the threshold produced by surrogate analysis with the “no coupling” null hypothesis. | 110 |
| 4.12 | Summary of connectivity between anatomical regions in each hemisphere. The summary is computed by taking the mean of the gPDC over the frequency range of 0-5Hz and over time between -127ms to 1000ms. | 112 |
| 4.13 | Summary of connectivity between anatomical regions in each hemisphere for 2 subjects for $H = 195$. The summary is computed by taking the mean of the gPDC over the frequency range of 0-10Hz and over time between -127ms to 1000ms. | 113 |

Chapter 1

Introduction

A great deal of research is currently being conducted to better understand brain function and to develop better treatments for various neurological and psychiatric disorders, rehabilitation and even cognitive enhancement. Some interesting research areas in this respect include neuro-feedback, computational psychiatry, brain computer interfaces (BCI) and brain stimulation. Neuro-feedback aims to self-regulate brain activity in order to alter cognition and behavior [1]. It can be used as a therapeutic tool in post-stroke recovery, normalize attention deficit hyperactivity disorder (ADHD) or even enhance peak performance [1]. The fledgling field of computational psychiatry concerns itself with using computational tools to decode the pathophysiology of psychiatric disorders with the aim of better diagnostics as well as discovering effective treatments [2], [3]. BCI is capable of detecting patterns of neural activity and translating them into commands for specific devices [4]. It has the potential to aid patients with significant motor disabilities, such as stroke patients [5], quadriplegics [6], cerebral palsy [7] patients, etc., to interact with their environments and provide them with more independence and better quality of life. BCI has also been used in

biometrics to authenticate disabled individuals, in drowsiness and fatigue detection for drivers as well as in neuro-gaming [8]. With all these applications it is no surprise that quite a number of consumer-level wearable electroencephalography (EEG) devices exist, such as the Muse from Interaxon¹, the EMOTIV Epoc+², and NeuroSky MindWave³, that are easy to use, portable, have low energy consumption and wireless connectivity. Non-invasive brain stimulation (NIBS) is used to study and explore large-scale network dynamics and the functional role of specific brain structures by allowing experimenters to perturb them [9]. It can enhance motor skills and cognitive function as well as provide therapeutic effects for patients with neurological and psychiatric disorders [9]. The two most common forms of NIBS are transcranial direct current stimulation (tDCS) and transcranial magnetic stimulation (TMS). All these areas of research rely on EEG and especially the associated signal processing required to extract useful information.

1.1 Electroencephalography (EEG)

EEG measures neural activity through scalp electrodes. The measured signal is a voltage that varies over time and is generally recorded at multiple standardized locations on the head.

Neuronal activity can be generated through two mechanisms: action potentials and postsynaptic potentials. An action potential is a depolarisation of the membrane that travels along the axon of the neuron, from the cell body to the dendrites of the next cell. Initially, the depolarisation causes the cell membrane voltage to change.

¹<http://www.choosemuse.com/>

²<https://www.emotiv.com/epoc/>

³<https://store.neurosky.com/pages/mindwave>

This begins a chain reaction along the axon where one segment depolarisation causes the adjacent membrane to depolarise resulting in a travelling voltage spike or action potential. Once the depolarisation reaches the axon terminals it triggers the release of neurotransmitters into the synapses. The neurotransmitters bind to the postsynaptic cell membrane receptors and cause local depolarization (excitatory) or hyperpolarization (inhibitory) currents depending on the type of neurotransmitter. If enough excitatory synapses have been activated compared to inhibitory and the cell body reaches a specific threshold voltage, the receiving cell generates a new action potential and repeats the process. A single cell's activity cannot be measured at the scalp because the voltages produced are miniscule and susceptible to cancellation in certain conditions.

Neural activity measured on the scalp is the result of local field potentials, which are generally the summation of postsynaptic or action potentials from large groups of neurons [10]. Each action potential and postsynaptic potential creates a dipole whose orientation is defined by current flows into and out of the cell. The summation of a number of these dipoles results in a measurable voltage at the scalp. However, if two nearby dipoles have the same orientation but opposite polarity, the dipoles cancel. Further, if the dipoles appear at different instances in time their individual contribution is too weak to be measured at the scalp. Therefore, local field potentials are constrained by two conditions: the timing and the spatial orientation of the dipoles [10]. In spontaneous brain activity, action potentials generally do not satisfy these two conditions. Therefore, the most likely source of local field potentials are dipoles generated by postsynaptic currents [10], [11]. More specifically, they are most likely generated by cortical pyramidal cells since they are aligned perpendicular to

the surface of the cortex [10].

In comparison to other neural measurement methods like positron emission tomography (PET) and functional magnetic resonance imaging (fMRI), EEG offers much greater temporal resolution. Since EEG is a measure of electrical neural activity it has finer temporal resolution in comparison to fMRI and PET whose measurements are governed by the hemodynamic response and concentrations of radioactive tracers, respectively. In comparison to fMRI, the main disadvantage of EEG is the spatial resolution. Magnetoencephalography (MEG) and electrocorticography (ECoG) measure magnetic and electrical neural activity, respectively, and offer similar temporal resolution. However, they are both expensive and the latter is invasive.

1.2 Evoked and event-related potentials

Evoked potentials (EPs) and event-related potentials (ERPs) are defined as EEG that has a consistent temporal relationship with a specific stimulus (i.e. EP) or reference event (i.e. ERP) with EPs being a more direct response to the stimulus [10]. Their usefulness lies in the fact that they are continuous measures of the neural processing of a stimulus. With various experimental manipulations you can determine which stages of processing are affected and how they are affected. They also provide a neural response when there is no observable behavioral response. EPs and ERPs generally require a large number of trials to measure the effect accurately since they usually have smaller amplitudes than the background neural activity and instrumentation and environmental noise.

1.3 Averaging and artifacts

EEG recordings containing the ERPs and EPs require further signal processing since these waveforms are always embedded in background neural activity. The classic approach is averaging the EEG signal over multiple trials that are time locked to the onset of the stimulus [10]. The assumption with this approach is that each trial contains a "deterministic" waveform response and the background EEG is random and uncorrelated with the response. Ideally, averaging reduces the magnitude of the random EEG noise while enhancing the ERP or EP waveform, thus improving the signal-to-noise ratio (SNR). The amount of noise reduction is a function of the number of trials used in the averaging procedure and the noise magnitude is generally reduced by a factor of \sqrt{N} , where N is the number of trials and the background activity has a Gaussian distribution. However, in practice there is latency jitter in the ERP and EP waveforms. Averaging in the presence of jitter causes the waveform components to "smear out", thus effectively reducing SNR.

EEG recordings can also be exceptionally noisy due to the presence of various biological artifacts like blinks, eye movements, muscle activity, skin potentials and cardiac activity [10], [12]. These are typically much larger in amplitude than EEG, EP and ERP signals and therefore need to be dealt with appropriately. There are two approaches to dealing with artifacts. First, the trial can be inspected and simply rejected if it does not meet certain criteria. This is called *artifact rejection*. Second, it may be possible to estimate the artifact and subtract the influence of the artifact. This is called *artifact correction*. Many methods exist in the literature that are tailored to the peculiarities of each type of artifact and generally fall into these categories: regression, filtering, blind source separation and source decomposition [12].

Linear regression was commonly used for removing EOG and ECG when these reference channel measurements were available [12]. To remove artifacts, simple filtering is not usually very effective because of the overlapping spectra of the artifact and EEG. Therefore, more advanced filtering methods are required like adaptive filtering, which require a reference signal, spatial filtering [13], and Bayes filtering [12]. Blind source separation makes certain statistical assumptions about the correlation or independence between the EEG and the source of the artifact and separates signal components based on these assumptions. Ideally, this method produces components where the artifacts and the EEG have been separated so that the artifacts can be discarded. Principal component analysis (PCA) converts the observed EEG into linearly uncorrelated components [14], whereas independent component analysis (ICA) converts the observed EEG into statistically independent components [15], [16]. The independence assumption tends to be more appropriate for separating EEG and physiological artifacts [12]. Source decomposition methods include wavelets and empirical mode decomposition [12]. These artifact removal methods can also be combined in any number of ways and some can be automated [17].

1.4 Brain source localization

When analyzing ERP or EP data, one is always curious how different neuronal populations in the brain are processing the stimulus. Fortunately we can apply brain source localization (BSL) algorithms to ERP data. By utilizing the scalp electrode positions, a volume conduction model of the head and sophisticated signal processing algorithms, we can infer the time course of neural activity in specific brain regions.

EEG is a summation of all the dipoles present at a particular instance in time.

Since the tissues in the head are a conductive medium, the dipole currents create a potential field throughout the head including the skin surface, which is termed *volume conduction* of the electrical activity [11]. Volume conduction has the effect of low-pass spatial filtering neural brain sources [11]. The main conductive tissues in the head include the brain, skull and the scalp, each of which have an associated resistance. The skull has a higher resistance, by a factor of 20-80, than the other two tissues [11]. When applying BSL algorithms, careful modelling of this volume conductor are required for accurate solutions. The preferred method involves obtaining an individual's structural MRI as well as the digitized positions of the electrodes on their scalp.

BSL algorithms can offer a considerable improvement in the SNR of EEG data and they are effective in removing the effects of volume conduction. In the EEG literature, BSL can be cast in the context of an *inverse problem*, which is stated in the present context as follows:

Given an observed scalp voltage, determine the location and orientations of the source dipoles.

This problem is ill-posed or underdetermined since there are an infinite number of solutions for a given scalp voltage distribution. Making some assumptions, such as spatial smoothness and source sparsity, regarding the distribution of the dipoles can help alleviate this problem. There are many BSL algorithms which include sLORETA [18], [19], minimum norm estimation [20], dipole fitting [21], and beamforming [22]–[25].

1.5 Brain connectivity estimation

A recent trend in neuroscience has begun to focus on the interactions between different brain regions, known as brain connectivity [26]. Brain connectivity leads to complex brain networks that provide the basis for the brain's ability to not only process external stimuli but also develop mental representations of the world [27]. Comparing structural and functional networks reveals that neurological and psychiatric disorders can result from connectivity abnormalities [28].

One approach to resolve the connectivity of neural activity between brain regions is to study the correlations or the frequency domain counterpart, spectral coherence. This is known as functional connectivity. If the goal is to fully characterize the interactions, then this approach provides limited information. Correlations do not distinguish between direct or indirect links between two brain regions [26], since a third region could drive the correlation between the first two regions. Another difficulty is deducing the directionality of the links to determine feedforward and feedback information and hence a measure of causality. This leads us to measures like partial directed coherence (PDC) and the directed transfer function (DTF) that are able to provide this information [26]. The PDC can distinguish direct links and directionality between nodes in a network, whereas the DTF reveals both direct and indirect links.

1.6 Organization of thesis

This thesis covers specific aspects of EP artifact rejection, ERP brain source localization and dynamic brain network connectivity estimation during an ERP.

- **Chapter 2** presents a new method of reducing the noise in the EEG response signal recorded during repetitive transcranial magnetic stimulation (rTMS). This noise is principally composed of the residual stimulus artifact and millivolt amplitude compound muscle action potentials (CMAP) recorded from the scalp muscles and precludes analysis of the cortical evoked potentials, especially during the first 20 ms post stimulus. The proposed method uses the wavelet transform with a fourth order Daubechies mother wavelet and a novel coefficient reduction algorithm based on cortical amplitude thresholds. Four other mother wavelets as well as digital filtering have been tested and the Coiflets 2 and 3 also found to be effective with similar results. The approach has been tested using data recorded from 16 normal subjects during a study of cortical sensitivity to rTMS at different cortical locations using amplitudes, frequencies and sites used in clinical practice to treat major depressive disorder.
- Recently, brain source localization and beamforming methods have played an important role in enhancing the utility of the electroencephalograph (EEG) and/or the magnetoencephalograph (MEG). Source localization methods are in general very sensitive to parameter values used to describe the underlying lead-field matrix, such as head shape, electrode positions, conductivity of various tissues of the head, etc. Errors in these parameter values can cause significant degradation in performance of these algorithms.

Chapter 3 describes the development of a robust minimum variance beamformer (RMVB) specifically for EEG applications that can deal with an arbitrary mismatch between the assumed and true lead field matrix. The approach optimizes the worst-case uncertainty performance, sacrificing a distortionless

response in exchange for more robust performance. The performance of the RMVB is compared with the classic minimum variance beamformer (MVB) as well as its regularized and eigenspace-based variations. The simulation scenarios highlight the superior ability of the RMVB to cope with arbitrary mismatches.

- Event-related potentials (ERPs) are a commonly-used and valuable tool for research in neuroscience and related fields. Of particular interest is the estimation of dynamic networks that the brain uses in the processing of ERPs. In **Chapter 4**, we develop an Adaptive Sparse ERP Tracking (ASET) algorithm that is based on a time-varying multi-channel autoregressive (AR) analysis. Generalized Partial Directed Coherences (gPDCs), which indicate causal (directed) information flow in the brain, are extracted from the AR reflection coefficient parameters. The time-varying gPDC estimates in turn yield a dynamic causal model which is indicative of the brain's processing of the ERP response.

We applied the ASET algorithm to study the dynamic relationship between the auditory cortex and all other regions of the brain, specifically with respect to networks formed from the amplitude modulation of beta-band oscillations in response to an ERP stimulus. The resulting gPDC activity yielded many similarities to a current model of human speech processing [29] and demonstrates the utility of gPDC analysis, especially in terms of the temporal sequencing of neural activity.

Chapter 2

Wavelet-based Muscle Artifact Noise Reduction for Short Latency rTMS Evoked Potentials

2.1 Introduction

Although repetitive transcranial magnetic stimulation (rTMS) of the dorsolateral prefrontal cortex (DLPFC) has been used as a treatment for major depressive disorder (MDD) for nearly two decades [30], the success rate has been relatively low. The current clinical technique obtains an estimate of the stimulus amplitude as a fraction (typically 110%) of the motor cortex threshold of the abductor pollicis brevis upper motor neurons, and an estimate of the stimulus position as 5 cm anterior to this motor stimulus site measured in a sagittal plane. The most clinically effective stimulus parameters are not known and neither the stimulus amplitude nor site may be optimal for that patient's DLPFC stimulation. Researchers have found that the

cortical responses are very dependent on the stimulus site with some sites even having no or very limited responses [31], with prefrontal and motor cortices having different reactivity to TMS [32]. Even the optimum stimulation current direction or coil angle can also vary by at least 45° among subjects [33]. It is also not surprising that the motor threshold varies considerably intra-subject [34] since the motor response is determined not only by the pulse amplitude stimulating the upper motor neurons, but also the other excitatory and inhibitory inputs to the muscle's lower motor neurons.

In order to improve the efficacy of rTMS, it would be beneficial to determine the optimum amplitude, position and coil orientation for each subject given the intra and inter-subject variability of these stimulation parameters. This requires the ability to record and analyze short to medium latency evoked potentials (EPs - within the first 30 ms post stimulus) to determine cortical responses rather than longer latency event related potentials (ERPs) recorded by others, e.g. [32]. The latter are determined by both cortical sensitivity, and primarily, cortical functional connections. However, the very large magnetic field during rTMS at clinical amplitudes saturates the fixed gain EEG input amplifiers unless these are decoupled during the stimulation using techniques such as sample and hold circuitry [35]. More recently variable gain EEG amplifiers with high bit number analog to digital converters have been employed to avoid this problem e.g.[36]. Unfortunately the cortical EPs, occurring especially during the first 20 ms, are difficult to analyze because they are obscured by the residual magnetic artifact signal and the very large (mV) synchronous compound muscle action potential (CMAP) recorded from the stimulated scalp muscles in the DLPFC stimulation field. Many researchers, e.g. [37], ignore the first 20-30 ms and concentrate on longer latency ERPs because of this noise. The challenge has been to

develop techniques that remove all or most of these artifacts without severely affecting the neural responses

The TMS artifact amplitude and duration are heavily dependent on the capacitances of the recording system used as well as electrode lead orientation and electrode/skin impedance. Even for sample and hold recording systems [35] there is a residual artifact when the amplifier is connected again. The TMS artifact has been extensively studied using both biological phantoms and cortical stimulation [36]. It was found that even under ideal conditions using variable gain amplifiers, the artifact is still several volts at 5.8 ms after initiation of the stimulus, but could be extended to 15-20 ms depending on skin/electrode impedance [36]. Independent and principal component analyses (ICA and PCA, respectively) have been used to identify and reduce TMS artifact for both sample and hold and continuously recording systems [38]–[40]. For example, PCA of multiple EEG recordings has been used to create a source model of the residual TMS artifact obtained and then employed to linearly decompose the recorded signal into brain and TMS signals [38]. Another group used ICA to remove the residual TMS artifact [40].

In rTMS treatment for MDD the stimulus site may be over the temporalis muscle (Brodmann area 46) or occipitofrontalis (Brodmann area 10). The signals recorded from electrodes located over these muscles therefore contain large muscle artifacts (CMAPs). Such artifacts are dependent on stimulus amplitude and coil orientation [41]. Cranial muscles underlying the wings of the figure-of-eight coil are often stimulated at clinical amplitudes [41]. In our previous work we assumed much of the muscle artifact signal power is in lower frequencies compared to the high frequency short latency neural responses. However, severely digitally filtering the signal (150

Hz to 2 kHz) could only reliably analyze EPs later than 13 ms and probably removed significant cortical signal as well [42]. Although the CMAP and cortical responses in TMS are triggered by the same impulse, “they are independent stochastic processes with no mutual interaction” and modifications of the ICA technique have been used to successfully identify CMAPs in the recorded signal resulting from TMS [43]. The topographical distribution of the muscle artifact has also been considered together with PCA to remove it [44]. However, in this approach the muscle artifacts are assumed to have higher frequencies than the neural signals and are separated using high pass filtering. This runs contrary to our assumption that short latency EPs contain higher frequencies and our experimental evidence of higher frequency brain activity resulting from rTMS. Several artifact suppression techniques, PCA, wavelet and pre-whitening, have been considered and developed to reduce the artifact to the same amplitude range as the cortical responses prior to removing them with ICA [45].

In this paper we present a novel artifact reduction technique also based on wavelet analysis specifically tailored to extract short latency EPs. This technique performs automatic noise reduction during data collection so that the nurse or technician can change the coil position or stimulus parameters until a significant cortical response is recorded. This technique may also be used as a preprocessing step to further signal analysis such as ICA or PCA since any residual artifact noise will be the same magnitude as the cortical responses. The technique was tested using the EEG data recorded from a group of normal subjects and the revealed neuroelectric responses are described and discussed.

2.2 Materials and Methods

2.2.1 Subjects

Sixteen subjects, 11 male and 5 female, ranging in age from 19 to 59 years (mean age 33.2 ± 14.6) , with no known neuro-psychological conditions volunteered for the study and gave written consent. The study was approved by the Research Ethics Board of St. Joseph's Healthcare, Hamilton, Ontario, Canada.

2.2.2 Stimulation

rTMS was delivered with a Magstim Super Rapid stimulator (The Magstim Co. Ltd., Carmarthenshire, Wales, U.K.) using 400 μs biphasic pulses and a Magstim figure-of-eight air-cooled coil P/N 1640 (0.93 tesla peak magnetic field) held tangentially to the head at each site with the handle held at 45° angle to the mid-sagittal plane. Stimulus amplitudes for left and right hemispheres were chosen to be 110% of the motor thresholds for the abductor pollicis brevis. These thresholds were determined as the minimum amplitudes required to elicit 4 CMAPs of at least 50 μV from these muscles in 6 trials. Anatomical MRI images were obtained for each subject and loaded into a Brainsight stereotactic system (Rogue Research, Inc., Montreal, Canada) to reconstruct a 3 dimensional image of the brain. The three DLPFC areas suggested for treatment of depression, Brodmann areas 9, 10 and 46, were identified and the stimulus sites were chosen as the middle of each area. The Brainsight system also references the center of the stimulating coil position and orientation to the selected cortical site. The left hemisphere sites were stimulated with 80 pulses at 10 Hz, while the right with 60 pulses at 1 Hz. These pulse frequencies were chosen as they

are typically used during clinical practice. Sham stimuli were also delivered at these frequencies with a coil at Brodmann area 46 and an active coil approximately 1m away at 60% of maximum energy to give the acoustic clicks. Each stimulus train was separated by a 1 min rest period.

2.2.3 EEG Recording

Sixteen channels of EEG in the 10-20 configuration (no central electrodes) with linked ear reference were recorded for each stimulus using a custom built EEG system [46] with sample and hold circuitry similar to [35]. The system locked out the amplifiers for 3 ms during which the magnetic pulse was given at 1 ms. The signals were recorded with bandwidth .16 Hz to 2 kHz at 5 kHz sampling rate using gold cup electrodes notched to prevent heating. 70 ms of data were recorded for the left sided 10 Hz stimulation and 100 ms for the right sided. For each train of pulses the signals were averaged and stored for later analysis.

2.2.4 EEG Processing

The data were further processed using MATLAB (The Mathworks, Inc., Natick, Massachusetts, USA). The averaged EEG is composed of a CMAP, cortical evoked responses, some residual background stimulus artifact and hardware generated exponential baseline. Before any further analysis, we first removed the exponential baseline. The baseline was modeled by $y = A \exp(-\lambda x)$, where A describes the amplitude and λ describes the rate of decay. MATLAB's `fminsearch` was used to minimize the squared error between the EEG in all channels and the exponential model over the segment from 25 ms to the end of the recording. The estimated baseline was then

subtracted from the original data.

The CMAP obstructs our ability to observe the cortical response immediately after the stimulus during recording because of its very large magnitude in comparison to the cortical evoked response. It exhibits a longer time course than short and medium latency cortical EPs. Accordingly, we reason that much of the lower frequency content can be attributed to the CMAP as well. It must be stressed again that the function of the noise reduction technique is to allow the clinician to immediately observe cortical sensitivity after e.g. 80 stimuli, not to study the observed signal in detail. This observation justified two approaches: simple digital filtering and wavelet noise reduction.

Digital Filtering

Neural activity in the higher frequency range was isolated using a 60th order zero phase Chebyshev digital filter with a bandpass of 150 Hz to 2 kHz. The lower cutoff frequency was chosen so as to remove as much of the CMAP as possible while having a less effect on the remaining cortical signal.

Wavelet Noise Reduction

EP recordings are typically composed of transient events, which complicates Fourier analysis and as a consequence digital filtering. Utilizing this denoising approach we can overcome certain limitations of digital filtering when dealing with the overlapping bandwidths of the CMAP, cortical evoked responses and residual stimulus artifact. For example, bandpass digital filtering passes high frequency activity up to 2 kHz, yet not all high frequency activity represents the cortical evoked response. Being

highly nonstationary signals, EP recordings are ideally suited for wavelet analysis, [47], which has the ability to localize transient events in time and frequency [48], [49]. Applying a wavelet transform produces a set of wavelet coefficients where each coefficient relates the contribution of a shifted and scaled wavelet to the original waveform. Wavelets have been applied in denoising applications resulting in techniques like VisuShrink, SureShrink and RiskShrink [50], [51]. These denoising methods generally apply the wavelet transform and modify the resulting coefficients based on a thresholding method referred to as a shrinkage function. The signal is then reconstructed with the modified coefficients resulting in a signal with less contaminating noise. Coefficients related to the signal of interest have a large amplitude whereas noise is predominantly represented by smaller amplitude coefficients. Thus, when applying a shrinkage function to wavelet coefficients, those exceeding a threshold correspond to the signal of interest and are left mostly untouched. Conversely, coefficients that fall below the threshold are typically set to zero.

Each channel of the averaged EEG data was decomposed using the discrete wavelet transform (DWT) (2.1).

$$[\mathbf{d}_1, \dots, \mathbf{d}_5, \mathbf{a}_5] = \mathcal{D}(\mathbf{X}) \quad (2.1)$$

where \mathcal{D} is the DWT operator, $\mathbf{X} \in \mathbb{R}^{N \times T}$ is the averaged EEG data matrix with N channels and T samples, \mathbf{d}_j are the detail coefficients at each level $j = 1, \dots, 5$ and \mathbf{a}_5 are the approximation coefficients at level 5. We used the Daubechies with 4 vanishing moments (db4), Coiflets 2 (coif2) and 3 (coif3), Haar and Biorthogonal 1.3 (bior13) mother wavelets.

The shrinkage function, $\delta(c)$, used to modify the coefficients was soft thresholding.

It subtracts the magnitude of the threshold, λ , from any coefficients exceeding that threshold and sets the others to 0, (2.2).

$$\delta^{\text{soft}}(c) = \begin{cases} \text{sgn}(c) (|c| - \lambda_i), & |c| > \lambda_i \\ 0, & |c| \leq \lambda_i \end{cases} \quad (2.2)$$

where c represents each coefficient from a set of coefficients (i.e. one of $\mathbf{d}_1, \dots, \mathbf{d}_5, \mathbf{a}_5$). Each set of coefficients has a threshold $\lambda_i, i = 1, \dots, 6$. It is very difficult to predict the contribution of artifacts and cortical responses to each wavelet coefficient. Rather than unequivocally associating large wavelet coefficients with the artifact, soft thresholding allows us to associate a maximum contribution from the cortical response to each coefficient.

Using these modified coefficients, the signal is then reconstructed using the inverse DWT.

$$\hat{\mathbf{X}} = \mathcal{ID}(\hat{\mathbf{d}}_1, \dots, \hat{\mathbf{d}}_5, \hat{\mathbf{a}}_5) \quad (2.3)$$

where \mathcal{ID} represents the inverse DWT operator, $\hat{\mathbf{d}}_1 \dots \hat{\mathbf{d}}_5, \hat{\mathbf{a}}_5$ represent the thresholded coefficients and $\hat{\mathbf{X}} \in \mathbb{R}^{N \times T}$ is the reconstructed signal.

The CMAP is at least two orders of magnitude larger than the cortical response and its representation in the wavelet coefficient domain will be characterized by large amplitudes. Therefore, this procedure effectively results in removing the cortical evoked responses and background cortical activity from the CMAP. The cortical components are contained within the residual signal, \mathbf{R} , which can be recovered by

subtracting the denoised CMAP, $\hat{\mathbf{X}}$, from the original signal, \mathbf{X} .

$$\mathbf{R} = \mathbf{X} - \hat{\mathbf{X}} \quad (2.4)$$

Preliminary work employing this method was presented in [52].

The residual was further processed using the mean channel (EEG were collected using a linked ear reference) to remove any residual common noise such as 60 Hz and non-zero signals at the ear reference electrodes. This step is performed after denoising to avoid unnecessarily contaminating all the channels with artifactual data as some channels are far less affected by muscle or stimulus artifact.

The wavelet-based methods of [45], [53] are similar to our approach. In general, [45], [53] also assume that large artifacts are represented by large wavelet coefficients. They differ from our approach mostly in the selection of the threshold which is an essential element of the algorithm. [53] selects a threshold proportional to the square root of the median of the wavelet coefficients derived from independent components. [45] follows a suppression approach where a suppression matrix is applied to the original data. The suppression matrix is derived from an estimate of the artifacts, which are in turn determined by a particular number of the largest wavelet components. The number of artifactual components is chosen so that they account for most of the relative error in the mixing matrix from an ICA decomposition.

Our thresholds were based on “oscillatory” data sets. Six subjects in our study exhibited continuous fast oscillatory patterns in the averaged recordings when stimulated at 10 Hz. These patterns, although completely unexpected, and not previously reported in the literature, did not affect the mood or cognitive ability of the subject during stimulation.

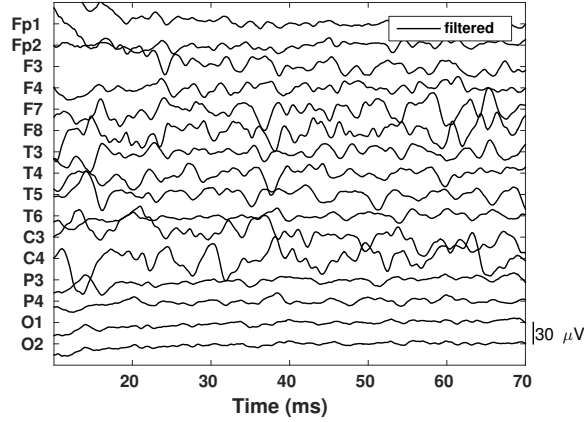


Figure 2.1: Average response for 80 stimuli at Broadmann area 10 for a 33 year old male, with data bandpass filtered from 25 to 2000 Hz.

Figure 2.1 shows oscillations in the 150 to 500 Hz range . It must be noted that this oscillatory pattern is phase locked to the stimulus since this figure is the average of 80 stimuli. Fast and very fast oscillations in the cortex have been described in the literature [54], [55] resulting from oscillatory neural networks responding to strong stimuli. Since CMAPs do not last longer than 20 ms, this sustained activity after 30 ms is likely to be cortical and assumed to be a good estimate of any cortical activity occurring earlier in the evoked response.

The DWT was applied to the unfiltered “oscillatory” data sets producing coefficients representing the cortical evoked response. The maximum of the absolute values of inter-subject coefficients for each set of coefficients ($\mathbf{d}_1, \dots, \mathbf{d}_5, \mathbf{a}_5$) were selected as the thresholds. This choice of thresholds allows us to associate any coefficients exceeding the threshold with the CMAP. In addition, the CMAP has a longer time course than short and medium latency EPs, therefore much of the lower frequency content can be attributed to the CMAP and residual stimulus artifact as well. Therefore the thresholds for the coefficients representing the lowest frequency components

$(\mathbf{d}_5, \mathbf{a}_5)$ were set to zero. The thresholds can be interpreted as an upper bound on the coefficients representing the cortical evoked response. The residual is effectively the cortical response and a suppressed CMAP artifact whose coefficients are limited to the threshold.

2.3 Results

The proposed methods along with digital filtering were applied to all rTMS responses from 16 subjects. The stimulus was presented at 1 ms, however the first 5 ms are not shown to account for the amplifier lockout and early settling. A typical response while stimulating the left hemisphere at B46 and prior to denoising is presented in Figure 2.2, with very large CMAP and the residual stimulus artifacts almost completely obscuring the cortical responses, e.g. in F3. CMAP artifacts were usually greatest when B46 was stimulated since this area lies directly under the temporalis muscle.

Generally the CMAP lasts for less than 30 ms and some researchers have avoided its effects by not stimulating at clinically effective amplitudes, severely lowpass filtering the responses or rejecting responses greater than $50 \mu V$, e.g.[56].

2.3.1 Simulation

The proposed methods were evaluated on a hybrid data set consisting of simulated EEG data and electrically stimulated CMAPs recorded using the same EEG configuration as described in Section 2.2.3. In order to evaluate the effectiveness of the proposed method on this specific type of artifact, it was necessary to record the

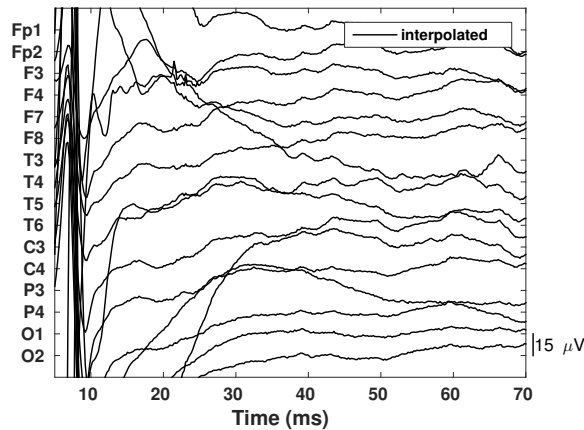


Figure 2.2: Response to 80 pulses at 10Hz to left B46 for a 21 year old female subject.

artifact on its own and without any evoked cortical activity. We recorded average CMAPs from the left hemisphere temporalis and occipitofrontalis muscles by surface stimulating cranial nerves V and VII in the temple area of a 29 year old male subject with 40 100 μs , 20-40 mA pulses at 10 Hz using a DS7A Digitimer Constant Current Stimulator (Digitimer Ltd, Welwyn Garden City, England). These CMAPs were similar to the rTMS evoked responses with no significant frequency content above 300 Hz even in F3. The only difference was that the electrically evoked CMAPs were more spatially localized, which affected the spatial distribution in channels further away from the stimulation site. As mentioned earlier, in rTMS stimulation the posterior temporalis muscle is also stimulated by the wing of the figure of eight coil. This muscle was also stimulated electrically as shown by the large artifact in C3 in Figure 2.3.

The EEG signal was simulated as a sinusoidal wave with a frequency of 200 Hz and an amplitude of 20 μV and was subsequently added to the recorded artifact.

Following the processing steps outlined in Section 2.2, Figure 2.3 compares the

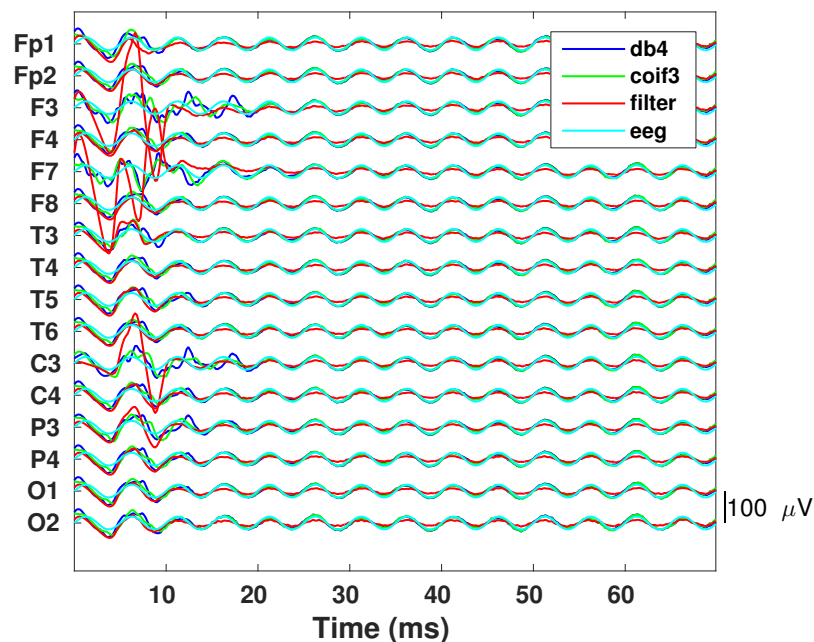


Figure 2.3: Residual from denoising simulated EEG contaminated by an electrically stimulated CMAP using wavelet denoising and digital filtering.

residual from wavelet denoising and digital filtering. Figure 2.4 compares the root-mean-squared error (RMSE) of both methods. Overall, wavelet noise reduction is more effective in suppressing the CMAP than digital filtering especially in channels and time samples that are more affected by the CMAP artifact (see F3, F7, and C3 in Figure 2.4 and their corresponding time series between 0-15 ms in Figure 2.3). These results emphasize the problem of filter transients at the beginning of a record when very large artifacts are present.

2.3.2 Real Data

The results of the proposed method using the data in Figure 2.2 and the Daubechies 4 mother wavelet were compared with digital filtering in Figure 2.5. Although digital filtering was effective in removing baseline fluctuations and limiting the CMAP to

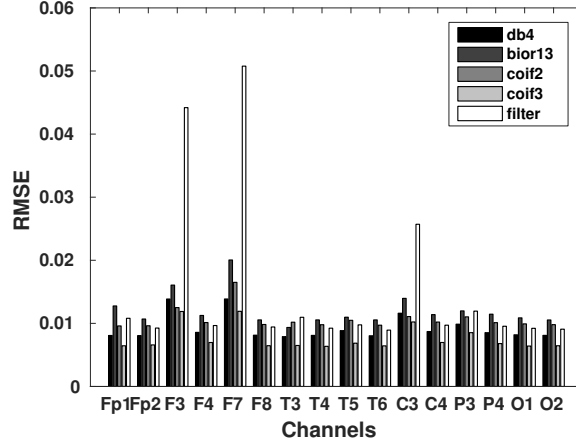


Figure 2.4: Comparison of root-mean-squared error (RMSE) in recovering the original simulated EEG signal for digital filtering and the proposed method.

the first 15 ms, the magnitude of the CMAP was still significantly larger than the rest of the signal making analysis of this region difficult. The left temporal channels and C3 are most affected with the very large CMAP artifact in C3 resulting from scalp muscle stimulation by the outer ring of the figure-of-eight coil [41]. After digital filtering, the remnant of the CMAP in channel C3 is still 1 mV in amplitude.

Focusing on channel C3 from Figure 2.5, Figure 2.6 compares digital filtering with wavelet denoising using different mother wavelets: Daubechies 4, Coiflet 2 and 3, and Biorthogonal 1.3. The Haar wavelet was also investigated but the the results were physiologically unrealistic. Similarly, the Biorthogonal 1.3 wavelet introduced repeated triangular components in the residual. This was most apparent in regions where the residual is expected to contain very little of the CMAP artifact, for example channel C3 between 20-30 ms. Since the Biorthogonal wavelet showed poor performance, it was omitted from the remainder of the results. The other wavelets produced similar results especially the Daubechies 4 and Coiflets 2 and 3. The advantage that wavelet noise reduction offers is clear in this figure. The amplitude of

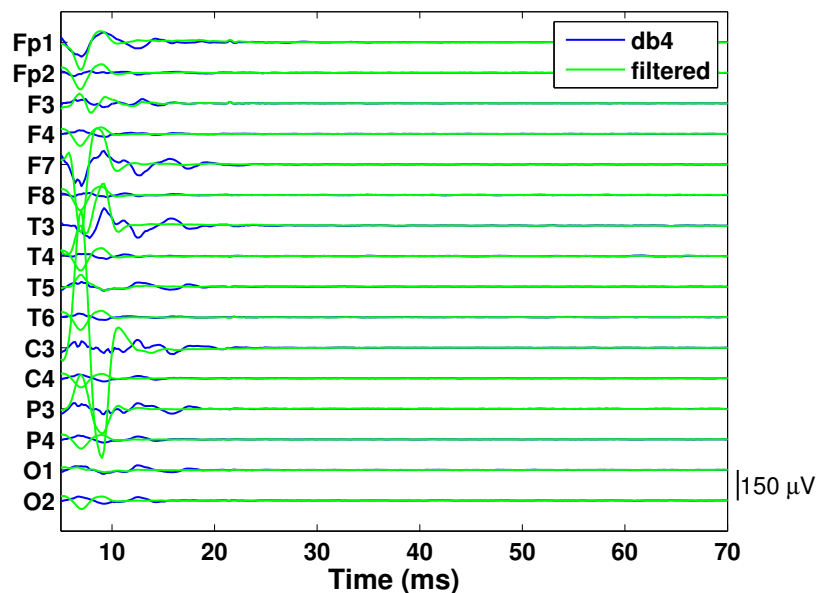


Figure 2.5: Residual after applying wavelet denoising and digital filtering to the data shown in Figure 2.2.

the CMAP is greatly attenuated while much of the remaining signal is left intact.

Figure 2.7 compares the residual from applying wavelet denoising to the data in Figure 2.2 using different mother wavelets. There is general agreement between the residual of the Daubechies 4, Coiflet 2 and Coiflet 3 wavelet denoising methods. The differences between them are approximation errors mainly due to the differences between the shape of the mother wavelet. Although the data have been transformed from linked ear to average reference, this has not been completely effective at removing the signal recorded by the reference electrodes. As can be seen in Figure 2.7, the responses at the occipital and right hemisphere electrodes are highly correlated and probably originate from the reference electrodes. The right hemisphere cortical responses should be delayed from 10-20 ms to account for neural pathway transmission including the corpus callosum [31]. Using the average reference is a common

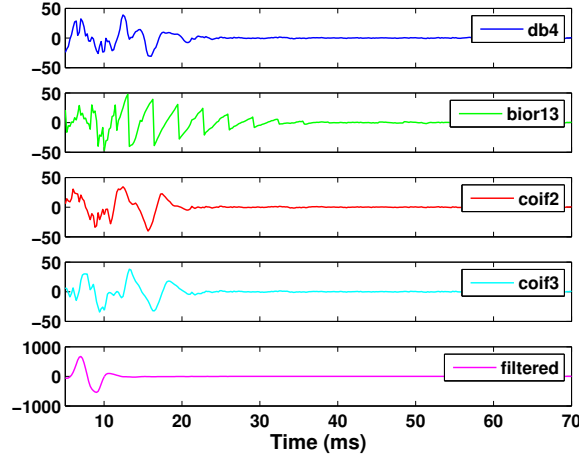


Figure 2.6: Residual of wavelet denoising with various mother wavelets (from top: Daubechies 4, Biorthogonal 1.3, Coiflet 2, Coiflet 3) and digital filtering at C3. Original data is shown in Figure 2.2.

practice in ambient EEG recordings, but it may not always be appropriate for evoked responses since some channels have very strong signals while others have near zero, resulting in a fraction of these strong signals being added to the remaining channels. For most of our subjects, however this was not a problem.

One measure of cortical response to stimulation used in the literature is the global mean field average (GMFA) [57]. It is a measure of the average cortical activity at each sample point and indicates the evoked electrical field strength across the scalp. It is a more general index than peak amplitudes and latencies and is useful for comparing cortical responses when these have complex shapes and differ among subjects. It is calculated as follows:

$$\text{GMFA} = \sqrt{\frac{1}{N} \sum_{i=1}^N (x_i - x_{\text{mean}})^2} \quad (2.5)$$

where N represents the number of channels, x_i is the potential at electrode i , and

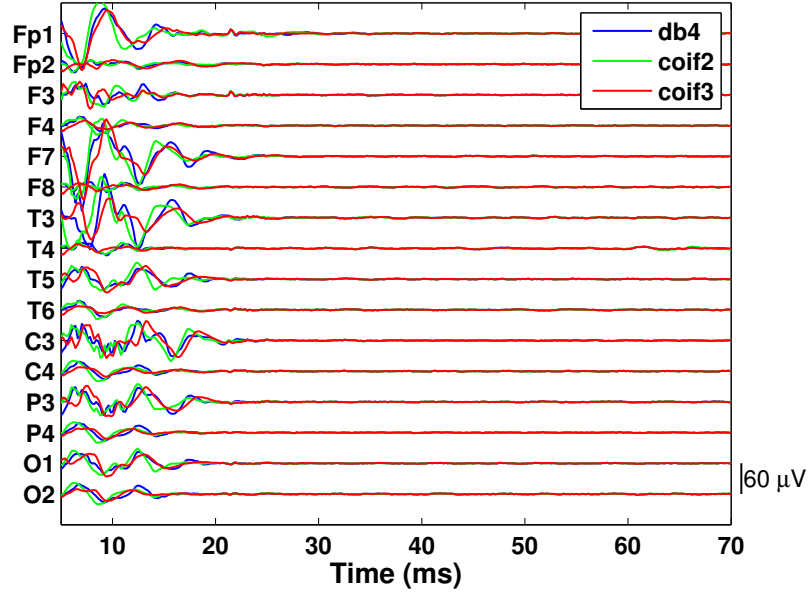


Figure 2.7: Residual of wavelet denoising with various mother wavelets. Original data is shown in Figure 2.2.

x_{mean} is the average of the N channels. The root mean square (RMS) of the GMFA was calculated over the 5-30 ms segment of the recording to quantify the responses. The interval of 5-30 ms includes the cortical response plus any residual CMAP and stimulus artifact.

Figure 2.8 compares the RMS of GMFAs over 5-30 ms obtained using digital filtering, db4 and two Coiflet noise reduction wavelets, for 10 Hz stimulation at left Brodmann areas 46, 10 and 9 for the subject of Figure 2.2. For B46 and B10, digital filtering results in much higher values due to the large residual muscle artifact (see also Figure 2.5), while B09 underlies very little scalp muscle and therefore the response contains little to no CMAP. As expected from Figure 2.7 the three wavelet noise reduction methods result in similar GMFA values for all three areas stimulated. They are all effective at reducing CMAP and residual stimulus artifact from the evoked

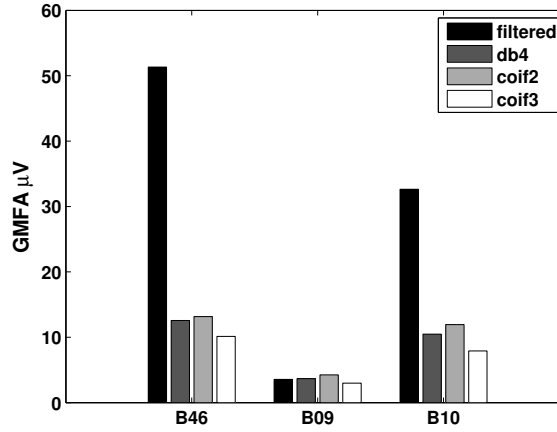


Figure 2.8: Average GMFA over the 5-30 ms interval of residual responses to 10 Hz stimulation at left B46, B09, B10 of the 21 year old female subject.

responses. The evoked responses for the entire subject group were processed using db4 and Coiflet noise reduction and the GMFAs calculated for the 5-30 ms intervals. The results for left hemisphere 10 Hz stimulation and db4 noise reduction, shown in Figure 2.9 demonstrate that there is considerable variation among subjects but also within subjects for the three areas stimulated. To save space, the right side 1 Hz stimulation and two Coiflet noise reduction wavelet results are not shown. Most subjects show that B09 stimulation has smaller responses than B10 and B46 and may be due to lower cortical sensitivity in this area. We cannot conclude this with certainty, however, the simulation results of Figure 2.4 show that the residual error for channels containing muscle artifact is at maximum twice that for channels having no muscle artifact, while Figure 2.8 shows the GMFAs for B46 and B10 are 3 to 4 times the B09 values.

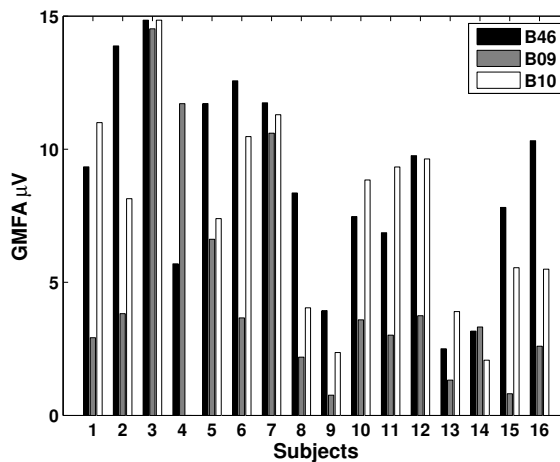


Figure 2.9: Average GMFA over the 5-30 ms interval of residual responses to 10 Hz stimulation at left B46, B09, B10 for all subjects and processed using wavelet noise reduction with the db4 mother wavelet.

2.4 Discussion

Digital filtering has been shown by us and others to be inadequate at removing muscle artifact, especially in the first 30 ms. Further, to achieve a stable baseline in the first 20 ms, the filter has to cut off lower frequency cortical activity. Even with a cutoff of 150 Hz, the 20 ms baseline can be nonzero, e.g. Figure 2.1. In the case of short latency evoked responses, high order digital filters can also introduce transients since the high amplitude data (CMAPs) occur at the very beginning of the record. The ICA approach offers an alternative to removing artifacts [43], but requires visual inspection and selection of the independent components, not a straightforward task. As well, the neural and artifactual activity may not be completely separable and too much neural activity is removed as a result of removing independent components [45]. In denoising techniques including the wavelet method presented here, the challenge is to remove as much artifact as possible without materially affecting the cortical responses. How much of the residual response is residual artifact, principally CMAP, and how much

is truly cortical? Does a large CMAP result in a larger putative cortical response? The simulation results of Figures 2.3 and 2.4, which used real scalp muscle CMAPs, show that digital filtering resulted in large residual artifacts in F3, F7 and C3, while the two best wavelet approaches removed them almost completely without affecting the simulated cortical responses. Further, an examination of Figure 2.5 shows that there is a large residual artifact at C3 and a much smaller response at F7 when using digital filtering from 150 to 2000 Hz. Wavelet noise reduction however, shows a larger response at F7 than at C3 indicating wavelet denoising is more effective at removing CMAPs from the signal than ordinary filtering. As well a greater bandwidth of the underlying cortical response is preserved in wavelet noise reduction as shown by the broader response peaks and lower frequency amplitude. This is further demonstrated in Figure 2.6 where the digital filtering result has much higher amplitude but much shorter response peak. Digital filtering at 150 Hz highpass was necessary to achieve a stable zero baseline in the response interval and obviously removes too much cortical response while being ineffective at removing the CMAP. This is not surprising since wavelets are much better at representing transient signals such as CMAPs and cortical evoked responses.

A second important question is whether the mother wavelet chosen in large part determines the residual response. In our work we examined 5 different mother wavelets. In wavelet denoising applications, when the goal is to recover the residual signal, it is clearly important that the mother wavelet is reasonably matched to the shape of the underlying nonstationary components of the signal. This is not the case for the Haar and Biorthogonal wavelets. However, Figures 2.6 and 2.7 show that the other three mother wavelets have quite similar results despite having different

durations and time history. The peak durations and times are reasonably similar as well as the amplitudes. Although there are small differences in minor peaks they can be considered equally effective at reducing CMAP artifacts and preserving the cortical responses. Although we have not presented peak amplitudes and times for the entire subject set, these can be readily calculated from the residual responses. We have calculated and presented GMFAs for the subject set, which is a popular but relatively gross measure of cortical response. The GMFA is affected very little by the fine detail differences for the three wavelets chosen as shown by Figure 2.8. The simulations show that these wavelets had similar RMSEs with Coiflet 3 consistently having the best results, followed by Daubechies 4. We chose the more common Daubechies 4 wavelet for GMFA presentation as representative of all three wavelets.

Figures 2.5 and 2.6 show that rTMS produces a damped oscillatory response in cortical neurons with frequencies greater than 100 Hz. These responses were observed for almost all subjects for both 1 Hz and 10 Hz stimulus rates. The frequencies are consistent with the continuing oscillatory patterns past 30 ms observed in some subjects e.g Figure 2.1, which are not affected by residual stimulus or CMAP artifacts. Further the oscillations and damping or exponential decay has been observed by Buzsaki and Draguhn [54] from rat hippocampus recordings in response to stimuli. They have further hypothesized that this could be observed from cortical responses to strong stimuli.

The large GMFAs in Figure 2.8 for the filtered responses of B46 and B10 stimulation are due to the large residual muscle artifact (or filter transient) since the CMAPs were very large due to the overlying temporalis and occipitofrontalis muscles. There is little to no muscle over B09 and the CMAPs from these muscles were much smaller

since the muscle stimulation amplitude away from the figure-of-eight coil focal point is much smaller. Figure 2.8 demonstrates the need for measuring short latency evoked potentials during rTMS stimulation for depression, at least during the first session, to determine the best site and stimulation amplitude for that patient. For there to be a positive effect, the cortex must be sufficiently stimulated to send signals to the deeper structures which determine mood. If the cortical response is very small, will there be sufficient neural drive to excite and modify the connections of the deeper structures? For this paper we used the accepted clinical stimulation levels and sites at or near those used in most clinical reports. Figure 2.9 shows that the cortical responses for B09 stimulation are much lower than for B46 and B10 for many subjects. Indeed, for subjects 9 and 15 they are at the background noise level (as determined by the sham results). If they were patients, stimulation at this site might have been ineffective. Further studies will have to be conducted to see if the cortex of B09 is less sensitive to stimulation than the other two sites.

It is interesting to note that for some subjects the clinical level of stimulation resulted in continuous oscillations of the cortex when stimulated at B46 and B10 (e.g. Figure 2.1). These oscillations were also synchronized to the stimulus pulse since the responses are the average of 80 stimuli. As well, for these subjects stimulating the right cortex at 1 Hz at the same stimulus amplitude did not cause continuous oscillations but the commonly seen exponentially decaying oscillatory pattern of Figure 2.7. It seems that higher frequency stimulation rates are required to sustain the oscillations. These patterns have not been reported in the literature (at least at these high frequencies) because most studies have used stimulation rates in the fractions of Hz.

2.5 Conclusions

Wavelet noise reduction has been shown to be more effective than filtering in removing much of the noise due to muscle activity from DLPFC rTMS short latency responses, allowing further quantification and study of these residual responses. Three different wavelets Daubechies 4 and Coiflets 2 and 3 were all effective and resulted in similar responses being revealed in the 5-30 ms post stimulus window. A set of thresholds were established for each mother wavelet from artifact-free and unfiltered segments of cortical signals displaying oscillatory behaviour assumed to be representative of typical rTMS-evoked potentials and used to process all subject data. The wavelet noise reduction method allows the further development of a measurement and signal processing system that can be used by technologically inexperienced staff to customize the optimum amplitude and site of rTMS stimulation for a patient. It also allows the further study of cortical responses and the effects of changing the stimulus amplitude, site and frequency.

Chapter 3

Estimating Neural Sources Using a Worst-case Robust Adaptive Beamforming Approach

3.1 Introduction

Electroencephalography (EEG) is a tool that is widely used to study the electrical activity of different regions in the brain. Its distinctive ability to record neural activity with great temporal resolution is its greatest advantage over other medical imaging technologies. Over the last two decades, there have been a number of developments in signal processing tools for analyzing EEG recordings, many of which have been inspired by work in radar and communications research.

One such problem that has been studied extensively is brain source localization. The goal is to identify regions of spatial activity and isolate source waveforms from any specified region. Other applications of brain source separation include neuro

diagnostics, signal to noise (SNR) improvement, artifact rejection and brain mapping [58]. Signal processing methods developed for this purpose allow researchers to relate cognitive function to various processing centers in the brain. Many algorithms have been designed for this purpose and generally fall into two categories: parametric and non-parametric. Parametric methods include sLORETA [18], [19], weighted minimum norm (WMN) [20], dipole fitting [21], subspace methods like MUSIC [59]. Non-parametric (beamforming) methods like minimum variance beamforming (MVB) [22], regularized MVB [23], [24], eigenspace-based MVB [25], and fast fully adaptive MVB (FFA-MVB) [60].

Existing beamforming methods are very effective in many cases, but they are based on assumptions that may not apply, or are expensive to apply in practice. When beamforming methods are applied in practical settings, many of the assumptions made about the environment, brain sources and the electrode array may no longer be accurate. Specifically, these may include inaccurate head geometries, misaligned electrode positions, inaccurately assumed brain source positions as well as other unknowns. All of these factors affect the computation of the forward head model, which is used to determine the lead field matrices, which in turn define the contribution of an equivalent current dipole to the signals received at the EEG electrodes. Performance of source localization methods degrades rapidly with errors in the lead field matrix that arise when these assumptions do not hold [25]. The result is a mismatch between the lead field matrix generated by our assumed forward model and the actual (true) lead field matrix [61]. The development of a more robust beamformer for brain source localization would provide better performance in response to all of these uncertainties.

The linearly constrained minimum variance beamformer (MVB) is a popular spatial filtering method for localizing brain sources that was introduced in [22]. It provides robust performance when uncertainties are present in the signal look direction [61]. However, it does not provide sufficient robustness in the face of different lead field matrix mismatches like electrode array or head modeling errors. Note that very accurate estimates of the head model and corresponding lead field matrix can be obtained from information provided by a magnetic resonance imaging (MRI) scan. However, even electrode co-registration errors can lead to significant degradation in output SNR [62]. Also from an economic perspective, the use of the MRI is very cost ineffective compared to an exclusively EEG-based beamforming method.

A few techniques exist that attempt to account for arbitrary mismatches between lead field matrices. They include diagonal loading-based [23], [24], [63], [64] and eigenspace-based beamformers [25], [65]. Diagonal loading methods involve regularization which involves a trade off between the SNR of the beamformer output and its spatial resolution [23]. These methods rely on a regularization parameter and the optimal value cannot easily be determined [61]. Eigenspace-based beamformers have been applied to MEG data by [25]. However, they are ineffective when there is a possibility of “subspace swaps”, which are encountered at low SNR when the eigenvalues of the signal subspace are indistinguishable from the eigenvalues of the noise subspace. This phenomenon may also occur in a high dimensional signal-plus-interference subspace, since in this case it may be impossible to accurately determine the number of sources [61].

In this paper, we propose the novel, robust minimum variance beamformer (RMVB) method, which is an extension of the minimum variance beamformer method that is

tolerant to a specified set of errors in the lead field matrix. The performance of the RMVB method is optimized for the worst-case conditions over this set. The proposed method achieves better localization performance than previous non-robust approaches, but trades off a relaxation in the constraint for improved signal extraction. The RMVB method is formulated as a convex optimization problem over a second-order cone, a fact which leads to a very efficient implementation of the method.

Previous work, [61], [66], has applied the same idea to the radar/sonar case. This paper extends this approach to the EEG context.

Section 3.2 presents a brief background to the minimum variance beamformer. The development of the robust minimum variance beamformer is given in Section 3.3. Section 3.4 provides details of the simulations used to demonstrate performance of the proposed RMVB method. Comparative results are presented in Section 3.5. Discussion and Conclusions are given in Sections 3.6 and 3.7, respectively.

3.2 Background

A beamformer is a spatial filter that passes signals originating from a specified (narrow) region of interest (i.e., the "spatial passband") and attenuates signals outside this region. It is described as the inner product of a weight matrix $\mathbf{W}(\mathbf{q}_0) \in \mathbb{R}^{N \times 3}$ for the location of interest, \mathbf{q}_0 , and the EEG signal $\mathbf{x} \in \mathbb{R}^{N \times 1}$ at time k

$$\mathbf{y}(k) = \mathbf{W}(\mathbf{q}_0)^T \mathbf{x}(k) \quad (3.1)$$

resulting in $\mathbf{y} \in \mathbb{R}^{3 \times 1}$ which represents the three components of the source dipole moment at time k and location \mathbf{q}_0 . The determination of \mathbf{W} is described subsequently.

The EEG signal $\mathbf{x}(k) \in \mathbb{R}^N$ is a vector of voltages that are recorded by N EEG electrodes at time k . At each time instant the measured signal is a superposition of L active brain sources. Each brain source is modeled as a dipole, $\mathbf{m}(k, \mathbf{q}_i) = \boldsymbol{\eta}(\mathbf{q}_i) a(k) \in \mathbb{R}^{3 \times 1}$, where $\boldsymbol{\eta}$ is a unit vector which describes the orientation of the source dipole and $a(k)$ is the source amplitude at time k . The contribution from a source at location \mathbf{q}_i to $\mathbf{x}(k)$ is determined by the lead field matrix, $\mathbf{H}(\mathbf{q}_i) \in \mathbb{R}^{N \times 3}$. Thus, \mathbf{x} is given by

$$\mathbf{x}(k) = \sum_{i=0}^L \mathbf{H}(\mathbf{q}_i) \mathbf{m}(k, \mathbf{q}_i) + \mathbf{n}(k) \quad (3.2)$$

where \mathbf{n} represents the background neural activity or noise.

The focus is to attenuate signals originating outside of our location of interest, \mathbf{q}_0 . Thus, (3.2) can be separated as follows

$$\mathbf{x}(k) = \mathbf{H}(\mathbf{q}_0) \mathbf{m}(k, \mathbf{q}_0) + \mathbf{i}(k) + \mathbf{n}(k) \quad (3.3)$$

or equivalently,

$$\mathbf{x}(k) = \mathbf{s}(k) + \mathbf{i}(k) + \mathbf{n}(k) \quad (3.4)$$

where \mathbf{s} represents the signal from the location of interest, \mathbf{i} , represents the interference, i.e. the neural signals that fall outside the location \mathbf{q}_0 . We can find the weight matrix, \mathbf{W} by maximizing the signal-to-interference-plus-noise-ratio (SINR)

$$\text{SINR} = \frac{\text{tr}(\mathbf{W}^T \mathbf{R}_s \mathbf{W})}{\text{tr}(\mathbf{W}^T \mathbf{R}_{i+n} \mathbf{W})}. \quad (3.5)$$

Since the covariance matrix \mathbf{R}_s cannot be measured directly, we approximate the maximization procedure by minimizing only the denominator, which represents the power of the received interference + noise components. Thus, the minimum variance beamformer (MVB) has the objective of minimizing the power of the $\mathbf{i} + \mathbf{n}$ components of the output of the beamformer. The trivial solution $\mathbf{W} = \mathbf{0}$ is avoided by maintaining a distortionless response at the location of interest. As a result the output represents the time varying signal at the location of interest with all other signals suppressed. The optimization problem of (3.5) may therefore be reformulated in the following way:

$$\min_{\mathbf{W}} \quad \text{tr}(\mathbf{W}^T \mathbf{R}_{i+n} \mathbf{W}) \quad (3.6a)$$

$$\text{subject to} \quad \mathbf{W}^T \mathbf{H} = \mathbf{I}. \quad (3.6b)$$

Using Lagrange multipliers, an analytical solution follows [22]

$$\mathbf{W} = \mathbf{R}_{i+n}^{-1} \mathbf{H} [\mathbf{H}^T \mathbf{R}_{i+n}^{-1} \mathbf{H}]^{-1}. \quad (3.7)$$

In practical situations the exact interference-plus-noise covariance matrix, \mathbf{R}_{i+n} , also cannot be measured directly. Instead it is estimated by the sample covariance matrix $\hat{\mathbf{R}}$:

$$\hat{\mathbf{R}} = \frac{1}{K} \sum_{k=1}^K \mathbf{x}(k) \mathbf{x}(k)^T = \frac{1}{K} \mathbf{X} \mathbf{X}^T, \quad (3.8)$$

where $\mathbf{X} \in \mathbb{R}^{N \times K}$ is the EEG data matrix with zero mean.

The MVB is very robust to interfering signals at different locations, however uncertainties in the lead field matrix, \mathbf{H} , cause the performance to degrade.

3.3 Robust Minimum Variance Beamformer

Note that throughout this paper, the notation $\|\cdot\|$ implies the 2-norm of the argument. Our purpose is to develop a beamformer that is robust to the uncertainties in the lead field matrices \mathbf{H} , by optimizing the worst-case performance over a prescribed region of uncertainty. We accommodate uncertainty by relaxing our constraint, which implies we are willing to sacrifice a distortionless response for a potentially better solution in terms of beamformer output SINR. In this case (3.6a) is reformulated as follows:

$$\min_{\mathbf{W}} \quad \text{tr}(\mathbf{W}^T \hat{\mathbf{R}} \mathbf{W}) \quad (3.9a)$$

$$\text{subject to} \quad \left(\mathbf{W}^T \tilde{\mathbf{H}}\right)_{ij} \geq (\mathbf{I})_{ij} \quad \forall \quad \tilde{\mathbf{H}} \in \mathcal{M}, \quad (3.9b)$$

where $(\cdot)_{ij}$ denotes the ij^{th} element of the argument, and $\tilde{\mathbf{H}}$ is the lead field matrix which is subject to uncertainty. \mathcal{M} is a set of lead field matrices describing our knowledge of possible uncertainties, to be defined later. We refer to the solution to this problem as the robust minimum variance beamformer (RMVB) [61], [66].

3.3.1 Reformulation

The constraint in (3.9b) describes an infinite number of matrices $\tilde{\mathbf{H}}$ in \mathcal{M} implying that there are an infinite number of constraints. This renders the problem semi-infinite and unsolvable using standard convex optimization techniques. We now show that the problem can be reformulated into a second-order cone program that is readily

solvable. In this vein, we define the uncertainty set \mathcal{M} as the set of $N \times 3$ matrices satisfying

$$\mathcal{M} = \{[\mathbf{m}_1 \ \mathbf{m}_2 \ \mathbf{m}_3] \mid \mathbf{m}_i = \mathbf{A}_i \mathbf{u} + \mathbf{h}_{0i}, \|\mathbf{u}\| \leq 1\} \quad (3.10)$$

where each of the columns, $\mathbf{m}_i \in \mathbb{R}^{N \times 1}$, represents an uncertainty ellipsoid with center $\mathbf{h}_i \in \mathbb{R}^{N \times 1}$. The matrix $\mathbf{A}_i \in \mathbb{R}^{N \times N}$ defines the physical aspects of the ellipsoid. Its axes are described by the left singular values of \mathbf{A}_i , which are of unit-norm, and are scaled by the respective singular values. The center of the ellipsoid, \mathbf{h}_{0i} , represents the corresponding column from our estimate of the lead field matrix, \mathbf{H}_0 .

Defining \mathcal{M} in terms of \mathbf{A}_i allows flexibility in describing the uncertainty. This version of \mathcal{M} in (3.10) defines an anisotropic uncertainty model, since the extent of the ellipsoid can vary in different dimensions.

We simplify the reformulation by describing the component-wise inequality constraint in vector form

$$\begin{aligned} \min_{\mathbf{W}} \quad & \text{tr}(\mathbf{W}^T \hat{\mathbf{R}} \mathbf{W}) \\ \text{subject to} \quad & \mathbf{w}_j^T \tilde{\mathbf{h}}_i \geq \delta_{ij} \quad \forall \quad \tilde{\mathbf{h}}_i \in \mathbf{m}_i \\ & i, j \in 1, 2, 3 \end{aligned} \quad (3.11)$$

where δ_{ij} represents the Kronecker delta and \mathbf{w}_j represents the j^{th} column of \mathbf{W} .

From (3.11) and using the definition in (3.10), the constraint

$$\mathbf{w}_j^T \tilde{\mathbf{h}}_i \geq \delta_{ij} \quad \forall \quad \tilde{\mathbf{h}}_i \in \mathbf{m}_i, \quad i, j \in 1, 2, 3 \quad (3.12)$$

is equivalent to

$$\mathbf{u}^T \mathbf{A}_i^T \mathbf{w}_j \leq \mathbf{h}_{0i}^T \mathbf{w}_j - \delta_{ij} \quad \forall \quad \mathbf{u} \quad s.t. \quad \|\mathbf{u}\| \leq 1. \quad (3.13)$$

To further simplify the constraint in (3.13), we realize that the inequality will hold for all $\|\mathbf{u}\| \leq 1$ if and only if it holds for the \mathbf{u} that maximizes $\mathbf{u}^T \mathbf{A}_i^T \mathbf{w}_j$. The maximum of an inner product is achieved if \mathbf{u} is a vector in the same direction as $\mathbf{A}_i^T \mathbf{w}_j$ and has the largest magnitude possible, which is limited by the constraint $\|\mathbf{u}\| \leq 1$. Therefore, $\mathbf{u} = \mathbf{A}_i^T \mathbf{w}_j / \|\mathbf{A}_i^T \mathbf{w}_j\|$. Substituting this solution into (3.13), we can rewrite it as

$$\|\mathbf{A}_i^T \mathbf{w}_j\| \leq \mathbf{h}_{0i}^T \mathbf{w}_j - \delta_{ij}. \quad (3.14)$$

Finally the robust beamforming problem can be written as follows

$$\begin{aligned} \min_{\mathbf{W}} \quad & \text{tr}(\mathbf{W}^T \hat{\mathbf{R}} \mathbf{W}) \\ \text{subject to} \quad & \|\mathbf{A}_i^T \mathbf{w}_j\| \leq \mathbf{h}_{0i}^T \mathbf{w}_j - \delta_{ij} \\ & i, j \in 1, 2, 3. \end{aligned} \quad (3.15)$$

Since the constraint does not include the trivial minimizer of the objective, the optimal solution will be achieved when the constraint reaches equality [66], and allows us to rewrite (3.15) as follows

$$\begin{aligned} \min_{\mathbf{W}} \quad & \text{tr}(\mathbf{W}^T \hat{\mathbf{R}} \mathbf{W}) \\ \text{subject to} \quad & \mathbf{h}_{0i}^T \mathbf{w}_j - \|\mathbf{A}_i^T \mathbf{w}_j\| = \delta_{ij} \\ & i, j \in 1, 2, 3. \end{aligned} \quad (3.16)$$

In addition to an anisotropic description of the uncertainty, we can also consider isotropic uncertainty which is described by $\mathbf{A}_i = \epsilon_i \mathbf{I}$. The problem in (3.15) then simplifies to

$$\begin{aligned} \min_{\mathbf{W}} \quad & \text{tr}(\mathbf{W}^T \hat{\mathbf{R}} \mathbf{W}) \\ \text{subject to} \quad & \mathbf{h}_{0i}^T \mathbf{w}_j - \epsilon_i \|\mathbf{w}_j\| = \delta_{ij} \\ & i, j \in 1, 2, 3. \end{aligned} \tag{3.17}$$

In effect, the RMVB beamformer sacrifices the distortionless response available in the MVB for a potential improvement in the output SINR.

3.3.2 Bound on the Error Matrix

Alternatively, we can also describe the set of matrices \mathcal{M} as the sum of the original lead field matrix, \mathbf{H} , with some error, \mathbf{E} ,

$$\mathcal{M} = \{\mathbf{H} + \mathbf{E} \mid \mathbf{E} = [\mathbf{A}_1 \mathbf{u} \ \mathbf{A}_2 \mathbf{u} \ \mathbf{A}_3 \mathbf{u}], \|\mathbf{u}\| \leq 1\}. \tag{3.18}$$

For practicality, it is useful to know how the region of uncertainty is defined and develop bounds on the error matrix, \mathbf{E} . We can easily look at the Frobenius norm of \mathbf{E} along with the fact that $\|\mathbf{u}\| \leq 1$ as follows:

$$\|\mathbf{E}\|_F = \left\| \begin{bmatrix} \|\mathbf{A}_1 \mathbf{u}\| \\ \|\mathbf{A}_2 \mathbf{u}\| \\ \|\mathbf{A}_3 \mathbf{u}\| \end{bmatrix} \right\| \leq \left\| \begin{bmatrix} \|\mathbf{A}_1\| \|\mathbf{u}\| \\ \|\mathbf{A}_2\| \|\mathbf{u}\| \\ \|\mathbf{A}_3\| \|\mathbf{u}\| \end{bmatrix} \right\| \leq \left\| \begin{bmatrix} \|\mathbf{A}_1\| \\ \|\mathbf{A}_2\| \\ \|\mathbf{A}_3\| \end{bmatrix} \right\|. \tag{3.19}$$

The 2-norm of a matrix is equal to the square root of the largest eigenvalue of that matrix; therefore

$$\|\mathbf{E}\|_F \leq (\lambda_{\max}(\mathbf{A}_1) + \lambda_{\max}(\mathbf{A}_2) + \lambda_{\max}(\mathbf{A}_3))^{1/2} \quad (3.20a)$$

$$\triangleq \epsilon. \quad (3.20b)$$

In the case of isotropic uncertainty where $\mathbf{A}_i = \epsilon_i \mathbf{I}$, this simplifies to

$$\begin{aligned} \|\mathbf{E}\|_F &\leq (\epsilon_1^2 + \epsilon_2^2 + \epsilon_3^2)^{1/2} \\ &\triangleq \epsilon. \end{aligned} \quad (3.21)$$

These bounds are useful for describing the extent of error used in the \mathbf{H} matrices in Section 3.5.

3.3.3 Standard Convex Reformulation

The problem in (3.17) is convex and in order to solve the problem we need to reformulate it into a standard convex problem [67]. A similar problem has been dealt with in [61]; here we modify that approach to develop a second order cone formulation suitable for the problem at hand.

To write the problem in standard convex form we let the Cholesky factorization of $\hat{\mathbf{R}}$ be

$$\hat{\mathbf{R}} = \mathbf{U}^T \mathbf{U} \quad (3.22)$$

This allows us to rewrite the objective as

$$\text{tr}(\mathbf{W}^T \hat{\mathbf{R}} \mathbf{W}) = \|\mathbf{UW}\|_F^2 \quad (3.23a)$$

$$= \|\text{vec}(\mathbf{UW})\|^2 \quad (3.23b)$$

where $\text{vec}(\mathbf{A})$ vectorizes the matrix \mathbf{A} .

Now realizing the following problems are equivalent

$$\min \|\text{vec}(\mathbf{UW})\|^2 \Leftrightarrow \min \|\text{vec}(\mathbf{UW})\| \quad (3.24)$$

and if we let $\|\text{vec}(\mathbf{UW})\| \leq t$, we can formulate the equivalent problem

$$\min_{\mathbf{W}, t} t \quad (3.25a)$$

$$\text{subject to } \|\text{vec}(\mathbf{UW})\| \leq t \quad (3.25b)$$

$$\|\mathbf{A}_i^T \mathbf{w}_j\| \leq (\mathbf{w}_j^T \mathbf{h}_{0i} - \delta_{ij}) \quad (3.25c)$$

$$i, j \in (1, 2, 3). \quad (3.25d)$$

All the constraints can be expressed as second order cone constraints. The second order cone, or the Lorentz cone, is defined as

$$Q^m = \{(x, y) \in \mathbf{R}^m \times \mathbf{R} \mid \|x\| \leq y\}. \quad (3.26)$$

So, the problem now becomes

$$\min_{\mathbf{w}, t} t \quad (3.27a)$$

$$\text{subject to } (\mathbf{vec}(\mathbf{UW}), t) \in Q^{3N} \quad (3.27b)$$

$$(\mathbf{A}_i^T \mathbf{w}_j, (\mathbf{w}_j^T \mathbf{h}_{0i} - \delta_{ij})) \in Q^N \quad (3.27c)$$

$$i, j \in (1, 2, 3). \quad (3.27d)$$

This is the final form of the RMVB optimization problem. It is to be noted the formulation is convex, a property which permits a straightforward and efficient implementation using a standard convex solver. In our case we used the `yalmip` package [68].

3.3.4 Uncertainty Models

Isotropic Uncertainty Model

Isotropic uncertainty was modeled by choosing a uniform worst case uncertainty bound, ϵ for all semi-axes of the uncertainty ellipsoid. This essentially imposes a spherical bound on the uncertainty. Thus,

$$\mathbf{A}_i = \epsilon_i \mathbf{I}, \quad (3.28)$$

where ϵ_i is to be determined. The isotropic model is appropriate in cases where there is no *a priori* information available about the uncertainties.

Anisotropic Uncertainty Model

Anisotropic uncertainty allows for more degrees of freedom and more accurate modeling of the uncertainties between lead field matrices. If additional information is available, namely the differences between the actual and estimated lead field matrices, we can develop a more accurate model. In our case, the two lead field matrices are \mathbf{H}_{est} and \mathbf{H}_{true} for the estimated and true models, respectively. Each component of the lead field matrices requires a corresponding \mathbf{A}_i which describes the extent and orientation of the ellipsoid. For simplicity, the index i is omitted in the following development.

The ellipsoid can be constructed as follows. The difference between the corresponding columns of the lead field matrices, \mathbf{b} ,

$$\mathbf{b} = \mathbf{h}_{\text{est}} - \mathbf{h}_{\text{true}} \quad (3.29)$$

indicates the actual uncertainty between both models. The main axis of the ellipsoid can be set along the vector \mathbf{b} with the length of the semi-axis being set to $\|\mathbf{b}\|$. On an empirical basis, we set the remaining $N - 1$ semi-axes to have orthonormal axes and magnitudes α , as follows:

$$\alpha = \min(0.1 \|\mathbf{b}\|, c) \quad (3.30)$$

where c is an upper bound on the uncertainty.

With the above information, we can construct the matrix \mathbf{A} using it's singular

value decomposition

$$\mathbf{A} = \mathbf{U}\mathbf{\Sigma}\mathbf{V}^T \quad (3.31)$$

where \mathbf{U} is an orthonormal basis in \mathbb{R}^N with the first column being $\mathbf{u}_1 = \frac{\mathbf{b}}{\|\mathbf{b}\|}$. The lengths of the semi-axes are described by

$$\mathbf{\Sigma} = \text{diag}(\|\mathbf{b}\|, \alpha, \dots, \alpha) \quad (3.32)$$

and $\mathbf{V} = \mathbf{I}$.

In this paper, results for the anisotropic case were obtained using the method outlined above, where \mathbf{H}_{true} was calculated using the boundary element method from a head with known anatomy. A consideration with regard to the anisotropic model is that the true head anatomy, from which the true lead field matrix is calculated, must be known. Unfortunately this information is not readily available in practice, unless an accurate head anatomy is determined beforehand using MRI images. However this process is expensive and should be avoided if possible. A more convenient means of circumventing this difficulty is to use the lead field matrices derived from a template MRI as the lead field matrix estimate, \mathbf{H}_0 . A template MRI is generally produced from a number K of individual MRI images, so we would compute the uncertainty ellipsoid from those individual MRI images with respect to the template MRI. This may be done by first computing the individual forward head models by applying the boundary element method to each MRI. Next, we would compute the covariance matrix for each lead field matrix component \mathbf{h}_i , by averaging outer products of the

\mathbf{h}_i over all K available head models. The result can then be used for the matrix \mathbf{A}_i .

$$\mathbf{A}_i = \frac{1}{K} \sum_{k=1}^K (\mathbf{h}_{k,i} - \mathbf{h}_{0,i}) (\mathbf{h}_{k,i} - \mathbf{h}_{0,i})^T \quad (3.33)$$

Overall this would produce a model over an approximately uniform sampling of the range of possible human heads.

This method has the advantage that it improves the uncertainty model at the expense of the memory and computational requirements associated with increasing the cardinality of the head model set.

3.4 Simulations

In this paper we base our simulations solely on event related potentials (ERPs). One ERP trial corresponds to an EEG recording that is time-locked to an applied stimulus, which is typically auditory, visual or somatosensory. Our ERP waveforms are simulated in a similar manner as described in [60], [69], where it is assumed that the ERP waveform is a result of phasic bursts of activity in response to the stimulus. Correspondingly, the simulated ERP waveform is modeled as the first half of the period of a sinusoid at 10 Hz, where the peak of the waveform has a temporal jitter to model inter-trial variability.

We restrict our simulations to the ERP case only, since many neuroscience applications require isolating the sources involved in the processing of stimuli, and furthermore the ERP case presents additional challenges for beamforming beyond what is typically encountered for the resting case, since sources may be highly correlated and observation record lengths may be short.

We simulate two dipoles with equal power, one representing the signal of interest and the other an interfering source. The signal dipole, d_s , is placed on the cortex of the left hemisphere near the medial aspect of Brodmann area 6 with coordinates, $[3.22 \ 3.96 \ 10.54]$ cm. The moment of the dipole was oriented along a vector from the center of the brain to the location of the dipole [70]. The temporal location of the peak is normally distributed among the trials, with a mean location of 476.5ms and standard deviation of 20ms. The interfering dipole, d_i , is placed on the cortex of the right hemisphere near the medial aspect of Brodmann area 8 with coordinates, $[5.26 \ -2.36 \ 10.31]$ cm. The signal waveform of the second dipole is identical to the first except for the occurrence of its peak, which is shifted to 636.6ms. This source configuration introduces correlation between the signal and interferer waveforms, a fact which can reduce the performance of certain types of beamformer, yet commonly occurs in practical situations. The orientation of the dipole is $\boldsymbol{\eta}_i = [1/\sqrt{2}; 1/\sqrt{2}; 0]$.

The scalp EEG signals $\mathbf{x}(k) \in \mathbb{R}^N$ are generated from the forward head model $\mathbf{x}(k) = \mathbf{H}\mathbf{s}(k)$, where $\mathbf{s}(k)$ are the dipole source waveforms and \mathbf{H} is the lead field matrix, which for these simulations is generated using the Brainstorm package [71], using a GSN HydroCel EEG cap with $N = 256$ electrodes. The lead field matrix is generated from the default anatomical data provided in Brainstorm using the boundary element method (BEM); specifically, the OpenMEEG toolbox [72]. The brain tissue, the skull and the scalp were modeled with conductivities of 0.33, 0.004 and 0.33, respectively. The head model consists of 15,028 vertices and provides the lead field matrix, \mathbf{H} , at each vertex.

The background neural activity model, which is used to simulate the noise, is added to each channel independently. It is based on the power spectrum of human

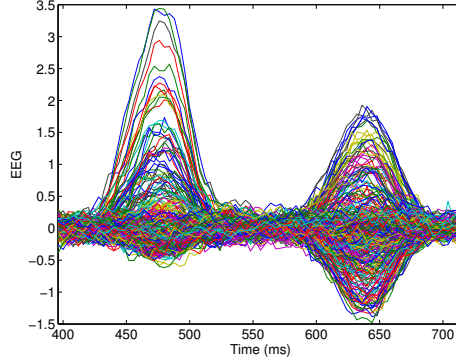


Figure 3.1: Simulated EEG with a SNR of -15dB, shown as the superposition of all 256 channels.

EEG and the methods employed in [69]. The uncorrelated noise is composed of 50 sinusoids with random frequency and phase and generated separately at each electrode. The frequencies of each sinusoid span the range 0-125 Hz with corresponding phases randomly spanning the interval $[0 - 2\pi]$ radians. The amplitude of each sinusoid is adjusted based on the power spectrum of empirical EEG data (at rest) [69]. Further details can also be found in [60].

Each of our simulated data sets consists of a waveform which is an ensemble average of $M = 100$ simulated individual ERP trials. The trials are sampled at $f_s = 250\text{Hz}$, each containing 250 samples. Figure 3.1 shows the ensemble average of the simulated data as the superposition of all 256 channels, where the two peaks correspond to the signal and interfering sources, respectively.

Since the signal portion of the simulated data is approximately stationary over an ERP trial, we can compute the sample covariance matrix by averaging over samples within a specified interval \mathcal{I} within a trial, and over all trials, as follows

$$\hat{\mathbf{R}} = \frac{1}{|\mathcal{I}|M} \sum_{m=1}^M \sum_{k \in \mathcal{I}} \mathbf{x}_m(k) \mathbf{x}_m(k)^T \quad (3.34)$$

where M is the number of trials, $|\cdot|$ denotes cardinality, and \mathcal{I} denotes a time interval, which typically corresponds to the region where the desired signal component is strongest. In our experiments we use all 250 samples for the interval \mathcal{I} . This formulation of the covariance matrix is in agreement with the rule of thumb provided by [73], [74], where the total number of averaged snapshots should be in the interval $[3, 4] \times N$ to ensure a sufficiently stable estimate of the covariance matrix.

The signal to noise ratio (SNR) is adjusted by scaling the ERP signal matrix of each trial. The SNR is calculated according to [25] as follows

$$\text{SNR} = \frac{\text{tr}(\mathbf{R}_s)}{\text{tr}(\mathbf{R}_n)} \quad (3.35)$$

where $\mathbf{R}_s \in \mathbb{R}^{N \times N}$ is the ERP signal covariance matrix and $\mathbf{R}_n \in \mathbb{R}^{N \times N}$ is the EEG noise covariance matrix.

3.4.1 Comparative Algorithms

We evaluate the performance of the RMVB in comparison to the original MVB. We also compare the RMVB with two other algorithms that are considered robust to mismatches in the lead field matrix, namely the regularized MVB [23], [24] and the eigenspace MVB [25], [65].

The regularized MVB simply replaces the sample covariance matrix $\hat{\mathbf{R}}$ with a regularized covariance matrix

$$\hat{\mathbf{R}}_{\text{reg}} = \hat{\mathbf{R}} + \gamma \mathbf{I} \quad (3.36)$$

where γ represents the regularization parameter. Throughout all our simulations, γ

was specified as a fraction of the largest eigenvalue of the sample covariance matrix, i.e. $\gamma = 0.005\lambda_{\max}(\hat{\mathbf{R}})$.

The eigenspace-based filter weight matrix \mathbf{W}_{eig} is formulated by projecting the MVB weight matrix \mathbf{W} onto the signal-plus-interference subspace of the sample covariance matrix. It is readily verified [25] that \mathbf{W}_{eig} is given as

$$\mathbf{W}_{\text{eig}} = \mathbf{E}_s \mathbf{E}_s^T \mathbf{W} \quad (3.37)$$

where \mathbf{E}_s is the matrix whose columns are the eigenvectors corresponding to the signal-plus-interference subspace eigenvalues.

In our experiments, the eigenspace MVB assumes that there is one interfering source, this implies using the two largest eigenvectors ($Q = 2$) to describe the signal-plus-interference subspace. However, in practice $Q = 3$ yields better results since in the finite sample case, the signal subspace spreads out over more dimensions.

3.5 Experiments

In this section we present results demonstrating the performance of the proposed RMVB algorithm relative to our comparison methods, for two separate cases – matched and mismatched. In both cases, the measured signals from the electrodes are simulated using the true forward head model obtained using the boundary element method. In the *matched* head model case, the weight matrix is calculated assuming knowledge of the true lead field matrix, whereas in the *mismatched* case, the weight matrix is obtained using a spherical (less accurate) head model.

3.5.1 Results for the Matched Head Model

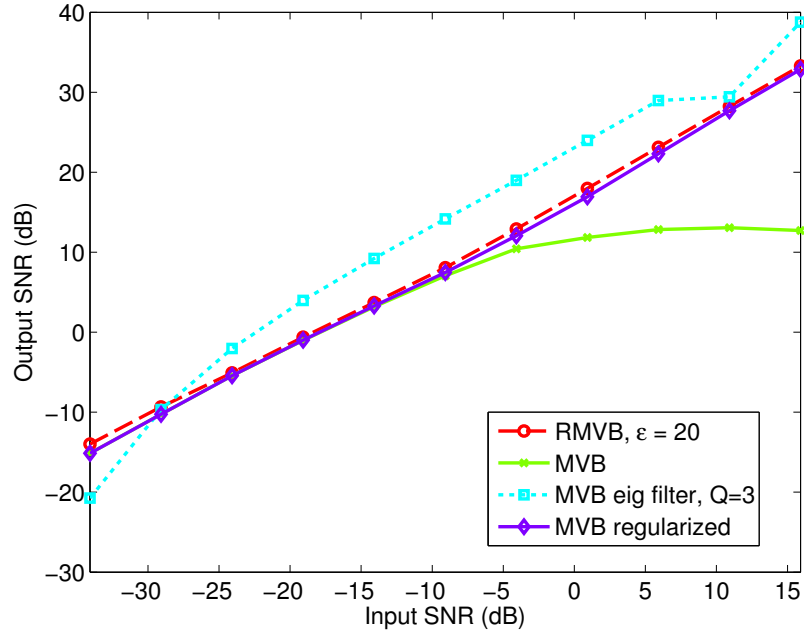
In the matched model scenario the uncertainty in \mathbf{H} is negligible. This justifies a low value for ϵ . In this case we choose the value $\epsilon = 20$, which corresponds on the basis of (3.21) to be approximately 3% of the average Frobenius norm of the lead field matrices. From (3.21), the uncertainty along each lead field axis is then given as $\epsilon_i = \sqrt{\epsilon^2/3}$.

Results: The performance of the beamformers as measured by beamformer output SNR and SINR vs. the input SNR when the beamformers are computed at the location of d_s is displayed in Figure 3.2. These results were generated by first calculating the covariance matrix from the combined simulated signal, interference and noise components. This covariance matrix was used to calculate the beamformer weight matrix \mathbf{W} for each of the beamformer methods considered. Then the signal, interferer and noise components were activated individually in turn and the corresponding electrode components were calculated using the respective forward head model. These electrode components were then fed through the respective beamformer and the respective output powers evaluated, to yield the various ratios shown in Figure 3.2.

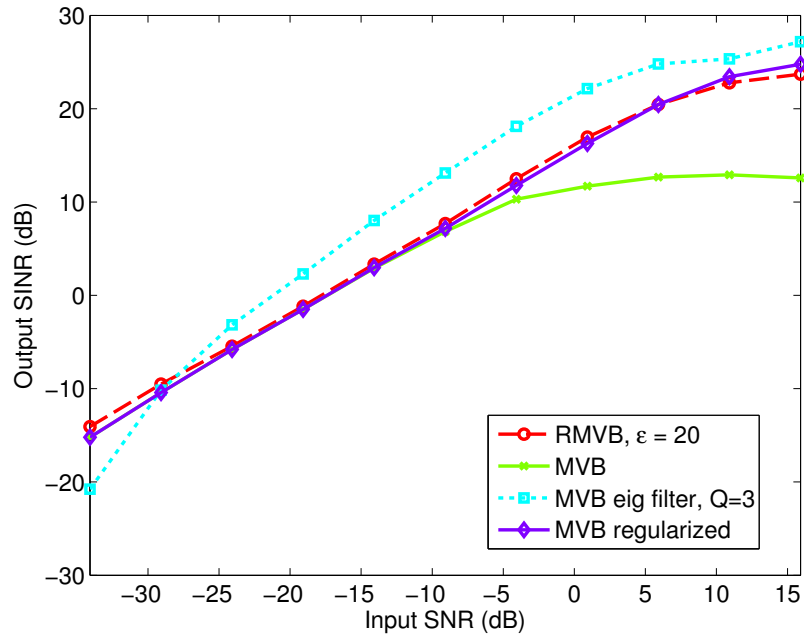
We can further examine the performance of the beamformers by examining their beampatterns. The beampattern is defined as a function of the spatial filter centered at the location \mathbf{q}_0 and can be expressed as follows

$$\mathbf{G}_i = \|\mathbf{W}^T(\mathbf{q}_0) \mathbf{H}(\mathbf{q}_i)\|_F \quad (3.38)$$

where $i = 1, \dots, V$ represents the vertices of the head model. The beampattern represents the gain of the spatial filter centered at \mathbf{q}_0 applied to the sources at each



(a) Beamformer output SNR vs input SNR for the matched case.



(b) Beamformer output SINR vs input SNR for the matched case.

Figure 3.2: Performance of various types of beamformer for the matched head model experiment at the location of d_s .

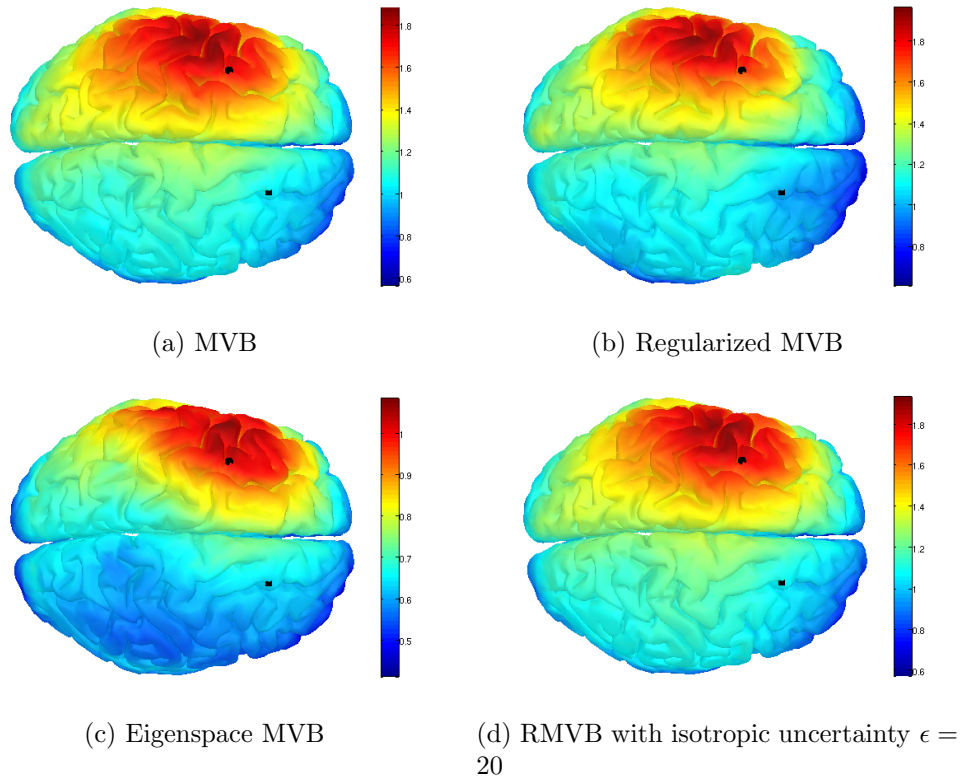


Figure 3.3: Beampatterns for the matched model scenario with an input SNR of -5dB, with respect to dipole d_s . \bullet and \blacksquare mark the locations of dipoles d_s and d_i , respectively.

vertex of the head model. In the case of the MVB, at the center of the spatial filter, $\mathbf{W}(\mathbf{q}_0)^T \mathbf{H}(\mathbf{q}_0) = \mathbf{I}$. Therefore, the gain is $\sqrt{3}$ and represents a distortionless response. With this representation we can further examine the tradeoffs between the various beamformers in our experiments.

The beampatterns for the matched head model experiment are shown in Figure 3.3. Each beampattern is represented by an individual colormap where blue and red represent the lowest gain and highest gain, respectively. In this scenario the beampatterns are very similar, although the eigenspace MVB displays a slightly different beampattern (Figure 3.3c). Generally, a region of high gain exists around the location of dipole d_s and low gain elsewhere especially around the location of dipole d_i . The main difference between the beampatterns is the ratio of the gain at the locations d_s and d_i which is directly related the output SINR of the beamformer.

The results of Figure 3.2 and Figure 3.3 show comparative results for the various beamformers under the ideal case where the head model is known accurately. These figures therefore serve as a reference to compare behaviour in the case of a 3-sphere (mismatched) model. Note that the eigenspace beamformer's performance drops off at low input SNR, because the signal subspace becomes indistinguishable from the noise subspace in these conditions; i.e., subspace swapping. At high input SNR, the performance of the MVB drops off, due to poor conditioning of the covariance matrix and resulting instability in the matrix inversion process.

The regularized beamformer has been designed to avoid this deficit, and these results show it is successful in this respect. Similarly, performance of the eigenspace beamformer levels off at high values of SNR and low values of Q , since in this case there are not enough degrees of freedom to adequately cancel the interference. Note that

in the low/medium range of input SNR, the proposed RMVB beamformer behaves virtually identically to MVB, but its performance does not fall off either at high or low values of SNR.

3.5.2 Mismatched Head Model

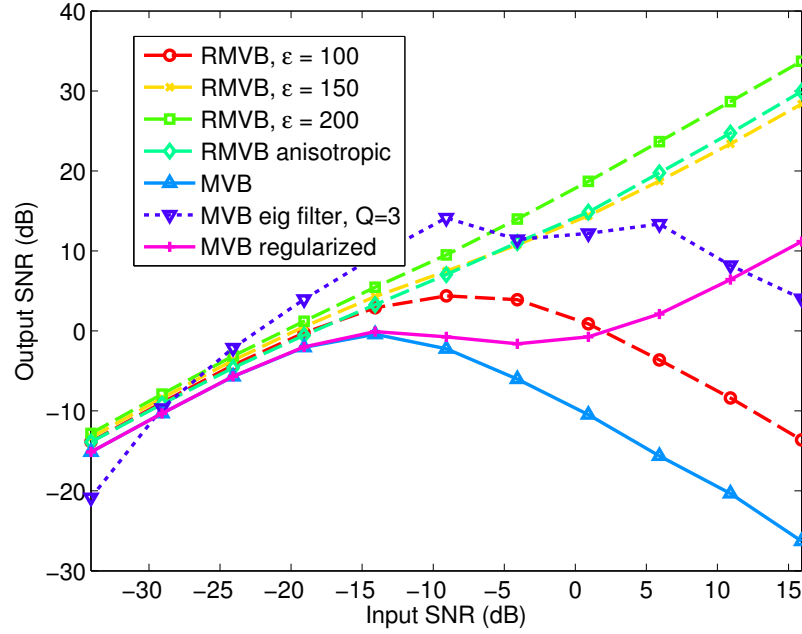
To showcase the particular strengths of the RMVB, we evaluate the beamforming methods in a scenario where the ERP data is processed using an approximate head model (“Mismatched Model” scenario). The mismatch in head models allows us to test the effects of errors in the lead field matrix.

The approximate head model is generated from the same anatomical data as the true head model. This ensures that the lead field matrices from both models could be easily compared since they make use of the same 3-dimensional mesh vertices describing the physical shape of the head. The mismatched or approximate head model is created using the 3-sphere [75] model which uses 3 spheres to model brain tissue, the skull and the scalp with conductivities identical to those of the true BEM model.

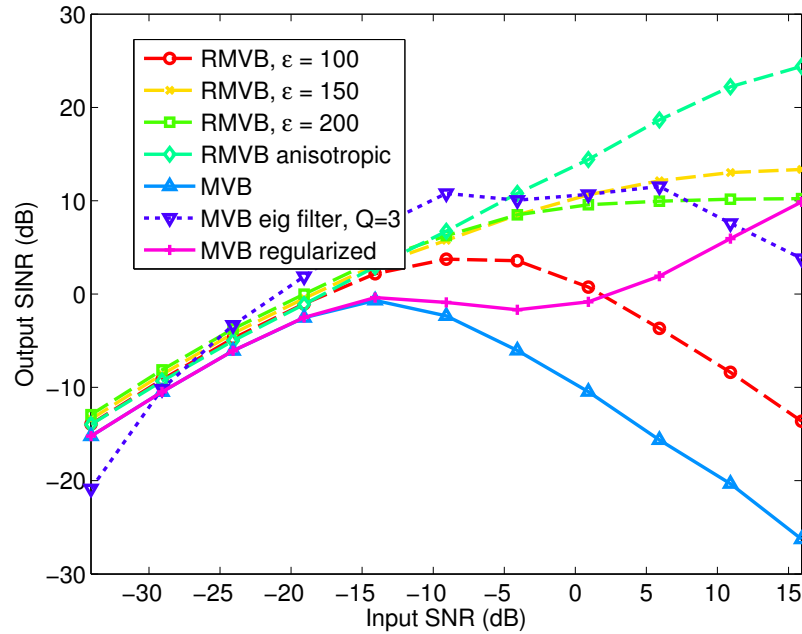
Isotropic RMVB Parameters: The uncertainty in the mismatched case is accommodated in the isotropic RMVB model by setting $\epsilon = 100, 125, 150, 175$ and 200 . From (3.21), the value of $\epsilon = 150$ is roughly equivalent to 20% of the average Frobenius norm of lead field matrices, \mathbf{H} , in the head model.

Anisotropic RMVB Parameters: The anisotropic model is created using the method described in Section 3.3.4, namely $\mathbf{H}_{\text{est}} = \mathbf{H}_{\text{3-sphere}}$ and $\mathbf{H}_{\text{true}} = \mathbf{H}_{\text{BEM}}$.

Results: The performance of the beamformers as measured by their output SNR and SINR vs. the input SNR when the beamformers are computed at the location of



(a) Beamformer output SNR vs input SNR



(b) Beamformer output SINR vs input SNR

Figure 3.4: Beamformer performance for the mismatched head models experiment at the location of d_s .

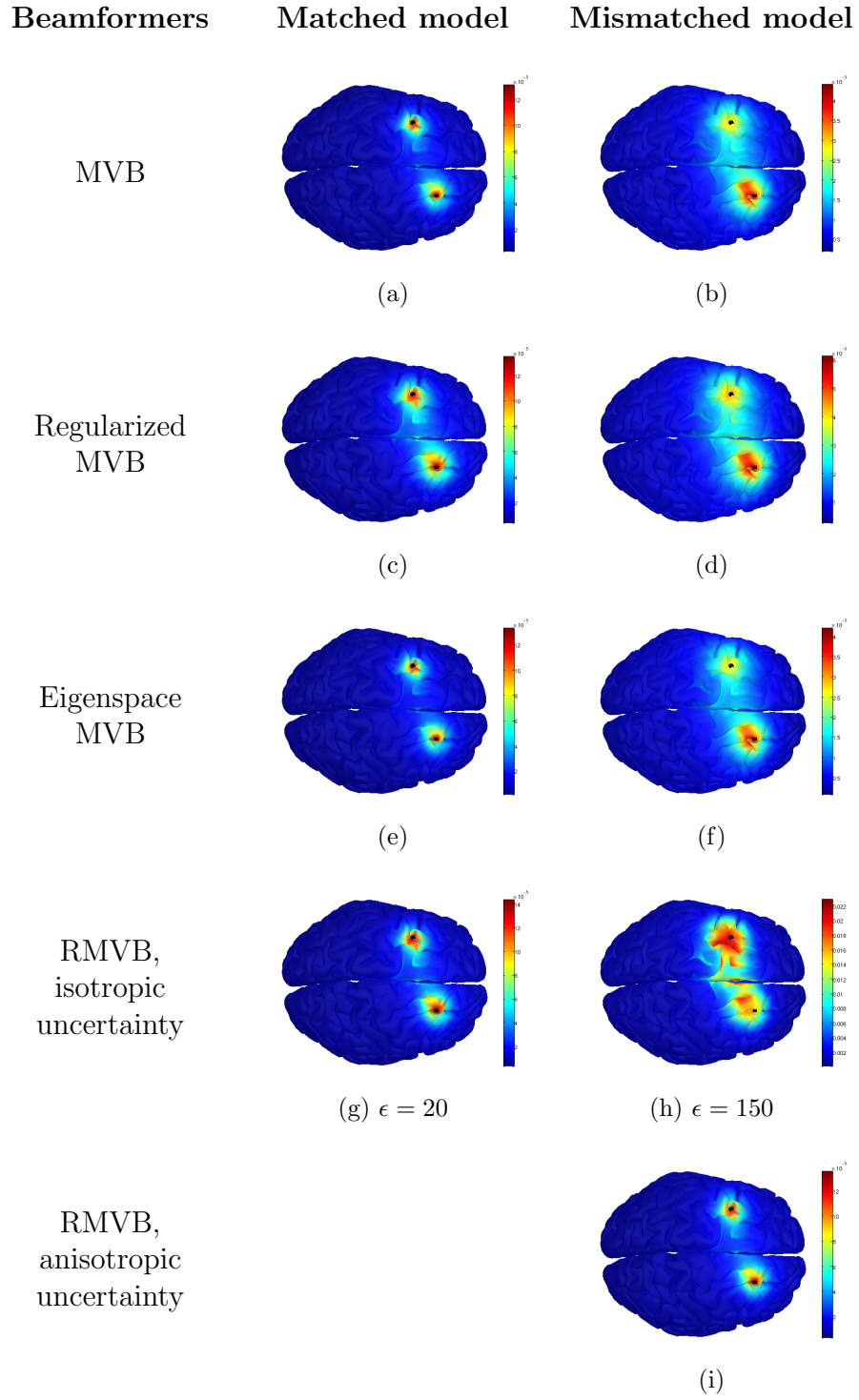


Figure 3.5: Localization plots over the time interval of 436.4-676.7ms for the mismatched model scenario. The input SNR is -5dB.

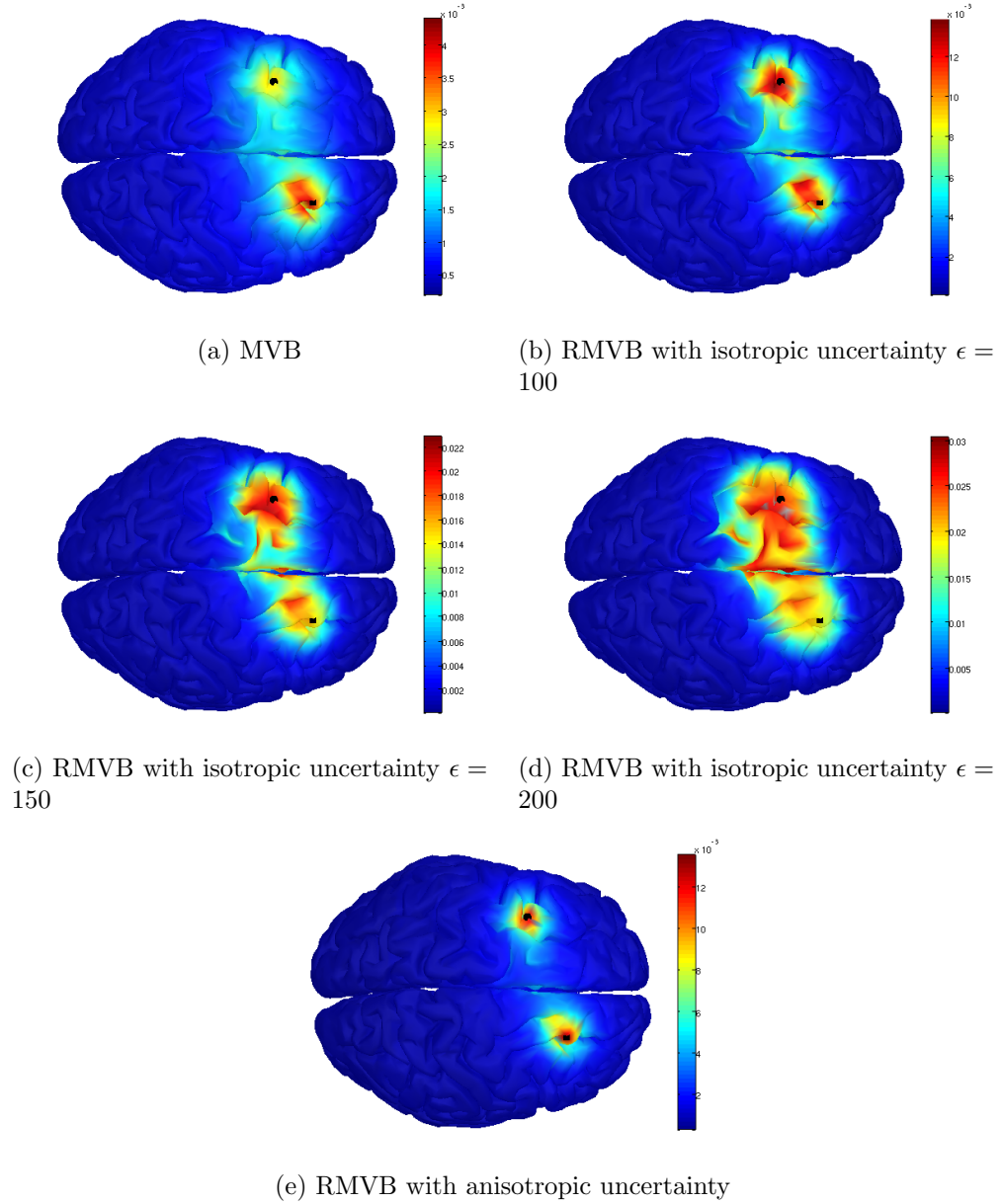


Figure 3.6: Average beamformer output power over the time interval of 436.4-676.7ms for varying degrees of isotropic uncertainty, $\epsilon = 100, 150$ and 200 . The input SNR is -5dB .

d_s is displayed in Figure 3.4. Comparison between this figure and Figure 3.2 shows that the degradation in performance of the MVB and regularized MVB caused by a realistic mismatched head model is indeed significant. It may be observed that the performance of the MVB decays significantly as the input SNR increases above about -15dB. The reason is due to the same phenomenon that caused the dropoff in performance in the matched case; i.e., the instability of the covariance matrix inversion process at high input SNR. However, in the mismatched case, the degradation begins at lower SNR due to the additional error introduced by the inaccurate head model. In contrast, except for the case $\epsilon = 100$, where RMVB is “close” to MVB, it may be observed that the RMVB variations are the only beamformer methods which do not suffer performance degradation in the mismatched case over the entire SNR range considered.

Another means of viewing the degradation in beamformer performance due to a mismatched head model, and the comparative robustness of the RMVB method to this mismatch, is through the localization plots shown in Figure 3.5. These figures represent the beamformer output power at each vertex where each beamformer is computed for that specific vertex. These plots cover the time interval of 436.4-676.7ms. The end points of this interval represent the nominal peak positions of the signal and interferer sources, respectively. It is seen that all beamformers are able to localize both sources, but they differ in the extent of the spatial source power distribution. We see that the effect of the mismatch is to widen the distribution relative to the matched case for all comparison beamformer types considered. Also weak, spurious responses are evident in the regions between the sources. In the mismatched case both the MVB and regularized MVB (Figures 3.5b and 3.5d) slightly underestimate

the power of the dipole d_s , which is represented by \bullet . In the isotropic uncertainty case for $\epsilon = 150$, RMVB also localizes the source power to larger spatial regions as shown in Figure 3.5h in a manner comparable to the other beamformers. However, we see that RMVB with anisotropic uncertainty (Figure 3.5i) has very similar performance to the MVB in the matched head model scenario (Figure 3.5a) and thus does not experience significant degradation in this mismatched case.

In Figure 3.6 we show how the localization performance varies with ϵ . As ϵ becomes too large, the source localization performance decreases. When $\epsilon = 200$ (Figure 3.6d), the RMVB beamformer has a much wider beam and consequently blurs the true location of a cortical source. We see that the localization performance for $\epsilon = 100$ compares favourably with the other beamformers in the presence of mismatch; however again we see that the performance of the anisotropic RMVB case in the presence of a mismatched head model is virtually equivalent to that of the matched case where the head model is known without uncertainty.

The beampatterns for the various beamformers for the mismatched case are shown in Figure 3.7. In these cases the regions of high gain for the MVB, regularized MVB and eigenspace MVB (Figures 3.7a to 3.7c) are not centered over d_s , a fact that can lead to diminished output SINR performance. On the other hand, we see that the eigenspace MVB and the RMVB beampatterns (Figures 3.7c to 3.7e) maintain a region of high gain around d_s , and low gain in the region of the interferer, in spite of the mismatched head model.

Figure 3.8 shows the beampatterns of the RVMB method for varying ϵ in the isotropic case. As ϵ is increased, the RMVB method is able to tolerate larger errors in the lead field matrix and as a result, the region of high gain concentrates more

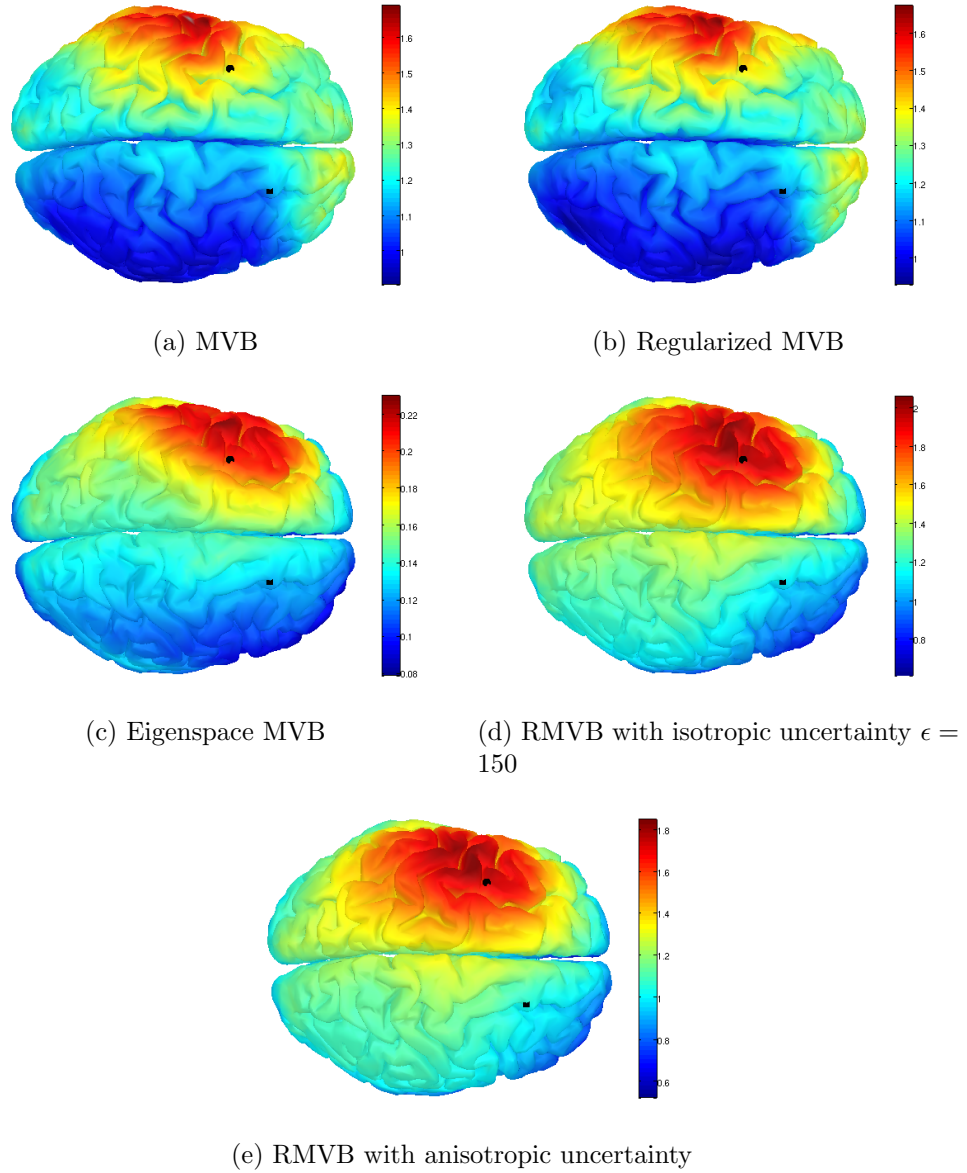


Figure 3.7: Beampatterns for the mismatched model scenario, with respect to dipole d_s . The input SNR is -5dB.

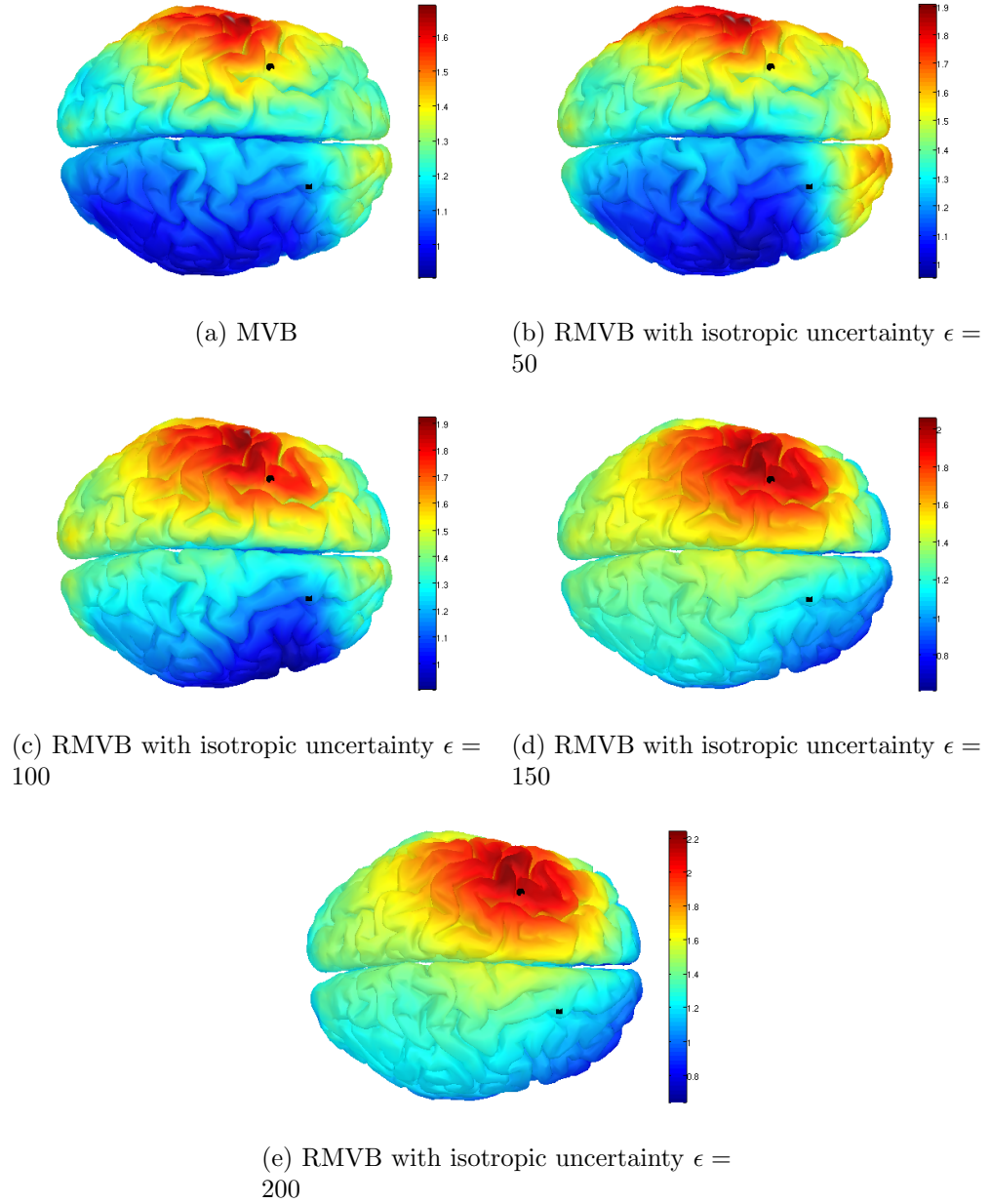


Figure 3.8: Beam patterns for the mismatched model scenario, with respect to dipole \mathbf{d}_s with varying degrees of isotropic uncertainty, $\epsilon = 50, 100, 150$ and 200 . The input SNR is -5dB .

over the actual location of the dipole \mathbf{d}_s .

In this section we have examined the relative performance of the RMVB beamformer in the mismatched case from several perspectives: a) input SNR vs. output SNR and SINR, b) localization characteristics and c) beampatterns. With regard to a), we see that the RMVB has consistent performance across a wide range of input SNR values, whereas the performance of the other methods falls off either at high or low values of SNR, or both. With respect to b), we see that in the anisotropic case, the localization behaviour of the RMVB beamformer in the mismatched case is equivalent to that of the MVB-based beamformers in the matched case. For appropriate values of ϵ , the degradation of the isotropic beamformer in the mismatched case is better than that of the MVB-based methods. Also, it is seen the RMVB beampatterns, unlike those of the MVB methods, consistently maintain regions of highest gain over the source and lowest gain over the the interferer.

3.6 Discussion

In the face of errors in the lead field matrix, the RMVB method has shown improved performance in many cases when compared with the MVB-based methods. RMVB is optimal in the sense that for all the possible lead field matrices that fall within our region of uncertainty, no other spatial filter produces less output power while maintaining an output response at the location of interest that is greater than the identity [66]. In other words, by acknowledging the uncertainty in the analysis, it identifies a region containing the most likely sources that produce the observed measurements.

We examine the situation when the uncertainty in RMVB goes to zero. From (3.10) we see that \mathbf{A} becomes zero in this case. Then from the definition of the

second-order cone from (3.26) and from (3.27c) we see that $\mathbf{w}^T \mathbf{h}_{0i} \geq \delta_{ij}$ in this situation. However (3.27b) implies that $\|\mathbf{W}\|$ should be as small as possible, which implies that $\mathbf{w}^T \mathbf{h}_{0i} = \delta_{ij}$, which is identical to the MVB constraint. Thus we see that the RMVB has the desirable property of becoming equivalent to the MVB as $\epsilon \rightarrow 0$.

The major difference between RMVB and MVB and its variants is in the formulation of the constraints. From (3.15) and (3.16) we see that the MVB constraint $\mathbf{W}^T \mathbf{H} = \mathbf{I}$ is replaced with the form $\mathbf{W}^T \mathbf{H} = \mathbf{I} + \mathbf{\Gamma}$ where $\mathbf{\Gamma}$ is a matrix with positive elements which are dependent on $\|\mathbf{H}\|$ and the characteristic of the uncertainty. This has the effect of forcing $\|\mathbf{W}\|$ to be larger in the RMVB case, so that for any \mathbf{H} within the uncertainty region \mathcal{M} , $\mathbf{w}_i^T \mathbf{h}_j$ is guaranteed to be equal to or greater than δ_{ij} .

In the following, we distinguish between two forms of \mathbf{H} and \mathbf{W} . The subscript “true” when applied to \mathbf{H} implies the actual lead field matrix corresponding to the head under consideration. Here we assume it may be calculated using the boundary element method, with negligible error. The subscript “est” in the present context implies \mathbf{H} is calculated using the 3-sphere head model. When these subscripts are applied to \mathbf{W} , they refer to the weight matrix calculated using \mathbf{H}_{true} and \mathbf{H}_{est} respectively.

Note that for MVB and its variants, the presence of error in \mathbf{H} results in the quantity $\mathbf{W}_{\text{est}}^T \mathbf{H}_{\text{true}}$ to no longer be equal to \mathbf{I} , where unlike the RMVB case, there is no guarantee of a lower bound on the value of each of the constraints. Thus, provided \mathbf{H}_{true} lies within the uncertainty region, RMVB maintains its performance in the presence of error in \mathbf{H} in the sense that the power along each component axis is preserved, whereas with MVB and its variants, the power along each axis can diminish. Thus we see in each case the beamformer outputs become uncalibrated.

In the RMVB case, the lack of calibration always increases or maintains the output power to the calibrated level, whereas in the MVB cases, the output power can either increase or decrease. A decrease in output power in the direction of the desired source can result in a decrease in the SINR and in the resolution of the beamformer. The RMVB formulation establishes a theoretically derived link between the uncertainty and the modified constraint.

We now investigate the effect of a loss of calibration at the beamformer output. For simplicity we assume a single source in the following analysis, since extension to the multi-source case is straightforward. From (3.2) in this case and ignoring noise, we have $\mathbf{x}(k) = \mathbf{H}_{\text{true}}(\mathbf{q})\mathbf{m}(k, \mathbf{q}) = \mathbf{H}_{\text{true}}(\mathbf{q})\eta(\mathbf{q})a(k)$, where η and $\alpha(k)$ are defined in Section 3.2. Since \mathbf{W} is calculated using \mathbf{H}_{est} , the beamformer output is then $\mathbf{y}(k) = \mathbf{W}_{\text{est}}^T \mathbf{x} = \mathbf{W}_{\text{est}}^T \mathbf{H}_{\text{true}}(\mathbf{q})\eta(\mathbf{q})a(k) = \mathbf{G}_{\text{true}}(\mathbf{q})\eta(\mathbf{q})a(k)$ where $\mathbf{G}_{\text{true}} = \mathbf{W}_{\text{est}}^T \mathbf{H}_{\text{true}}$. Thus we can see that the beamformer gain in this case is \mathbf{G}_{true} . However, we must distinguish between \mathbf{G}_{true} and the estimated gain, $\mathbf{G}_{\text{est}} = \mathbf{W}_{\text{est}}^T \mathbf{H}_{\text{est}}$. The loss of calibration can be seen in Table 3.1, which shows the true gain, \mathbf{G}_{true} . The true MVB gain, (upper right in Table 3.1), diverges significantly from the identity matrix with some main diagonal values being considerably less than 1, whereas the true RMVB gains are closer to the identity, thus recovering the true sources more accurately.

Now we can compare the true gain to the estimated gain, \mathbf{G}_{est} , in Table 3.2. In the RMVB case, due to the constraints, all elements of \mathbf{G}_{est} are greater than or equal to the respective identity matrix element. Thus, the RMVB beamformer compensates for the loss of calibration by increasing the gain beyond the nominal value of unity, for \mathbf{H} within the region of uncertainty. For the MVB-based beamformers, the constraint forces the gain to the identity. This is visualized in Table 3.2.

Table 3.1: Values for the quantity $\mathbf{W}_{\text{est}}\mathbf{H}_{\text{true}}$ for various beamformer configurations at dipole location \mathbf{d}_s and input SNR of -5dB.

| | |
|--|---|
| $\begin{bmatrix} 1 & 0 & 0 \\ 0 & 1 & 0 \\ 0 & 0 & 1 \end{bmatrix}$ | $\begin{bmatrix} 0.8552 & -0.1397 & -0.2387 \\ 0.0146 & 0.5167 & -0.3193 \\ -0.0209 & -0.1999 & 0.3861 \end{bmatrix}$ |
| $\mathbf{W}_{\text{true}}^T \mathbf{H}_{\text{true}}$ (MVB) | $\mathbf{W}_{\text{est}}^T \mathbf{H}_{\text{true}}$ (MVB) |
| $\begin{bmatrix} 1.0466 & 0.1200 & 0.0536 \\ 0.1647 & 0.8089 & 0.0429 \\ 0.1139 & 0.1265 & 0.8158 \end{bmatrix}$ | $\begin{bmatrix} 1.0066 & 0.0183 & 0.0108 \\ 0.0163 & 1.0029 & 0.0125 \\ 0.0066 & 0.0177 & 1.0042 \end{bmatrix}$ |
| $\mathbf{W}_{\text{est}}^T \mathbf{H}_{\text{true}}$ (RMVB $\epsilon = 150$) | $\mathbf{W}_{\text{est}}^T \mathbf{H}_{\text{true}}$ (RMVB anisotropic) |

It is important to note that the uncertainty model plays a significant role in determining the performance of the RMVB method. If the assumed uncertainty is much lower or much higher than the actual uncertainty in the data, the performance can degrade. This effect can be seen by looking at the RMVB traces with $\epsilon = 100$ and 200 vs. $\epsilon = 150$ in Figure 3.4b where we see a relative degradation in performance. Thus, choosing the uncertainty level for the isotropic model requires some care. As ϵ increases, the “beam” of the beamformer widens, thus introducing the potential for spurious sources (as seen in Figure 3.6d) or a loss of discrimination of nearby sources.

According to our analysis, an ϵ between 20 and 30% of the average magnitude of the lead field matrices is appropriate when the sources are sparse (about 5cm apart). If the sources are more dense a more conservative uncertainty level is advisable. The anisotropic uncertainty model is amenable to further improvements depending on the availability of data describing the diversity of realistic head models.

The eigenspace MVB generally gives good performance, although on the lower end of the input SNR range, it underperforms due to the subspace swap phenomenon

Table 3.2: Values for the quantity $\mathbf{W}_{\text{est}}^T \mathbf{H}_{\text{est}}$ for various beamformer configurations, at dipole location \mathbf{d}_s and input SNR of -5dB.

| | |
|--|--|
| $\begin{bmatrix} 1 & 0 & 0 \\ 0 & 1 & 0 \\ 0 & 0 & 1 \end{bmatrix}$ | $\begin{bmatrix} 1 & 0 & 0 \\ 0 & 1 & 0 \\ 0 & 0 & 1 \end{bmatrix}$ |
| $\mathbf{W}_{\text{true}}^T \mathbf{H}_{\text{true}} \text{ (MVB)}$ | $\mathbf{W}_{\text{est}}^T \mathbf{H}_{\text{est}} \text{ (MVB)}$ |
| $\begin{bmatrix} 1.2818 & 0.2818 & 0.2818 \\ 0.2419 & 1.2419 & 0.2419 \\ 0.2340 & 0.2340 & 1.2340 \end{bmatrix}$ | $\begin{bmatrix} 1.1677 & 0.1031 & 0.1301 \\ 0.0774 & 1.3694 & 0.1102 \\ 0.1448 & 0.0915 & 1.2271 \end{bmatrix}$ |
| $\mathbf{W}_{\text{est}}^T \mathbf{H}_{\text{est}} \text{ (RMVB } \epsilon = 150)$ | $\mathbf{W}_{\text{est}}^T \mathbf{H}_{\text{est}} \text{ (RMVB anisotropic)}$ |

[61] discussed earlier. Also its performance degrades if the dimension of the signal-plus-interference subspace is high or if the dimension is unknown [61]. In contrast, the performance of the RMVB approach is seen to maintain high relative levels over a wider range of input SNR values.

The average runtime to compute the beamformer weights, \mathbf{W} , for the beamformers MVB, RMVB $\epsilon = 150$ and RMVB anisotropic at a single vertex are 0.30s, 2.82s, and 15.33s, respectively on a single core of an Intel Xeon E5-2640 2.5 GHz processor.

3.7 Conclusion

We have proposed a robust minimum variance beamformer tailored for EEG applications. It is robust to uncertainties in the lead field matrix, which include head model and electrode array inaccuracies. Uncertainty in the lead field matrices is introduced into the RMVB formulation using either an anisotropic or isotropic model. These introduce respectively, an ellipsoidal or circular region of uncertainty, centered

around the columns of the estimated lead field matrix. The RMVB beamformer is implemented as a second order cone optimization problem, which is convex, efficient and straightforward to implement.

When a mismatch exists between the head model used for analysis and the true head model, the RMVB shows performance advantages in comparison to the MVB, regularized MVB and eigenspace MVB methods. These performance gains are with respect to input SNR vs. output SNR and SINR characteristics, localization performance and robustness of the beampattern.

Chapter 4

Sparse Dynamic Causal Network Estimation for Event-Related Potentials

4.1 Introduction

Estimating dynamic functional connectivity of the brain is a topic that has received significant attention in recent years. The electroencephalogram (EEG) has played an important role in this respect, and has been applied in many fields such as neuroscience, neurology, psychiatry and others [26].

The event-related potential (ERP) is the EEG response to some form of repetitive stimulus, often in the form of an auditory pulse or an alternating visual pattern. The time interval over which the ERP response is active is referred to as a *trial*. In this study we concentrate on EEG rather than fMRI data, since the EEG is much easier to dispatch in a practical setting and offers higher temporal resolution than the

fMRI. The ERP is a rich source of information regarding the dynamic connectivity that evolves in the brain while processing external stimuli. Dynamic connectivity in the present context has to do with the estimation of the time-varying, *directed* brain network structure that is involved in the processing of an ERP. The concept of directed connectivity is important, since it gives direction of information flow in the brain and thus provides us with increased insight about its behaviour and network architecture.

A concept closely related to directed connectivity is *causality*, which implies that one node (source) of the network influences another. Specifically, *Granger causality* refers to the case where the past of one time series x_j improves the prediction of another x_i more than x_i itself [26].

A core concept in determining causal connectivity is the vector autoregressive (VAR) model of a network of nodes. In the most general case, the VAR represents a vector of node measurements, $\mathbf{x}(k)$, as a linear combination of the P past node measurements:

$$\mathbf{x}(k) = \sum_{p=1}^P \mathbf{A}_p(k) \mathbf{x}(k-p) + \mathbf{w}(k) \quad (4.1)$$

where $\mathbf{x}(k) \in \mathbb{R}^{N \times 1}$ represents measurements across N nodes at sample k , P is the order of the AR process, $\mathbf{A}_p(k) \in \mathbb{R}^{N \times N}$ represents the p^{th} order VAR coefficients at sample k , $p = 1, \dots, P$ and $\mathbf{w}(k)$ represents the driving white noise with covariance $\Sigma_{\mathbf{w}}$. A number of measures which are useful for network estimation can be computed from the VAR model. These include the directed transfer function (DTF) and the partial directed coherence (PDC) [26]. PDC infers direct causal influences between nodes in a network whereas the DTF describes the cascade of flows through a node

[26]. The PDC assesses causality in the Granger sense and was chosen for this paper since we are interested in direct influences of one source on another.

Much of the literature focuses on functional connectivity under the assumption of stationarity. Suitable VAR estimation methods in this case are presented in [76], [77] and [78]. However in this study we wish to allow for the possibility that the brain sources active in processing the ERP evolve over the epoch. Therefore we cannot assume that stationarity holds, i.e. the VAR estimation process becomes time-varying. We therefore consider adaptive implementations for time-varying VAR (tvVAR) estimation; specifically we choose a variation of the multi-channel adaptive lattice algorithm [79], [80], which is explained in further detail in Section 4.2.

The estimation of the ERP-processing network of the brain is made difficult since the desired EEG components are buried in noise caused by other neural processing activity in the brain. This situation can be improved by assuming that every ERP trial is a realization of the same stochastic process, and therefore the underlying covariance structure associated with the ERP pulse does not vary between trials [26]. In AR analysis, the autoregressive coefficients \mathbf{A}_p in (4.1) are formed using the received signal covariance matrix. Therefore this assumption allows us to improve the stability of the covariance matrix and hence the AR estimates by averaging over multiple epochs [81] and thus improve SNR.

Since the processing of the ERP stimulus does not require all of the brain's resources, we may assume the associated ERP-processing network of the brain is sparse. However, existing methods for estimating tvVAR models [82]–[85] do not incorporate sparsity and perform poorly when the underlying causal network is sparse [86]. In

addition, the dense VAR model requires the estimation of a large number of parameters which in turn requires a large number of measurements for a good estimate. This problem is further exacerbated when a large number of nodes is being considered. Estimation of sparse brain networks has been studied in previous work, but this work has not considered adaptive algorithms that can track sparse signals over time [87].

Since the PDC estimates are sensitive to volume conduction, the ERP data was processed using the regularized Linearly Constrained Minimum Variance (LCMV) Beamformer to isolate sources of activity in the brain and hence suppress the effect of volume conduction. The beamformer outputs replace the raw electrode signals in subsequent analysis. Here the LCMV beamformer algorithm was modified so that the output represents aggregate activity over a finite cortical patch, instead of at a single voxel, in order to reduce the dimensionality of the problem. A further advantage of beamforming in this context is that since the desired source waveforms are isolated at the beamformer output, background noise activity is suppressed, thus improving SNR. Further details of the beamforming procedure are given in Sect. 4.3.6.

In this paper we present a method for estimating the time-varying brain network structures that evolve during the processing of an ERP. The network is derived from the PDC coefficients which are in turn derived from a time-varying, multi-channel least-squares lattice (LSL) autoregressive estimation process that has been modified to encourage sparsity (thereby suppressing spurious connections). Background EEG activity is partially suppressed by modifying the LSL algorithm to exploit averaging over multiple trials and by using a beamforming algorithm to preprocess the raw EEG signals before autoregressive analysis. The proposed method is validated by simulation results and by experiments on real ERP data. These latter results are

compared with those of the recent literature and found to agree well.

4.2 Background

4.2.1 Partial Directed Coherence

Partial directed coherence (PDC) is a frequency dependent measure of directed functional connectivity between multiple time series [26]. It describes the interaction between two time series and discounts the influence of all other $(N - 2)$ time series [88]. The PDC can also be interpreted as a measure of causality in the Granger sense where the past of one time series x_j improves the prediction of another x_i [26].

The PDC of a multivariate time series is defined as a function of the vector autoregressive (VAR) model parameters that adequately describe the multivariate time series. To obtain a dynamic estimate, this paper focuses on estimating a time-varying VAR (tvVAR) model described in (4.1). The VAR model is then transformed into the frequency domain

$$\mathbf{A}(t, \omega) = \sum_{p=1}^P \mathbf{A}_p(t) e^{-j\omega p} \quad (4.2)$$

The PDC from channel j to channel i , $\pi_{i \leftarrow j}(t, \omega)$, is defined as the $(i, j)^{\text{th}}$ element of $\bar{\mathbf{A}}(t, \omega)$ normalized by the total outflow variance from channel j to all channels.

$$\pi_{i \leftarrow j}(t, \omega) = \frac{\bar{A}_{ij}(t, \omega)}{\sqrt{\sum_{n=1}^N |\bar{A}_{nj}(t, \omega)|^2}} \quad (4.3)$$

where $\bar{A}_{ij}(t, \omega)$ is the $(i, j)^{\text{th}}$ element of $\bar{\mathbf{A}}(t, \omega)$ which is defined as follows

$$\bar{\mathbf{A}}(t, \omega) = \mathbf{I} - \mathbf{A}(t, \omega) \quad (4.4)$$

or more specifically

$$\bar{A}_{ij}(t, \omega) = \begin{cases} 1 - A_{ij}(t, \omega) & i = j, \\ -A_{ij}(t, \omega) & i \neq j \end{cases} \quad (4.5)$$

PDC is not scale invariant and can produce misleading estimates when the time series are not normalized. The generalized PDC (gPDC) [89] solves this problem by normalizing the signals by their innovation variances and is defined as follows,

$$g\pi_{i \leftarrow j}(t, \omega) = \frac{\frac{1}{\sigma_{ii}(t)} \bar{A}_{ij}(t, \omega)}{\sqrt{\sum_{n=1}^N \left| \frac{1}{\sigma_{nn}(t)} \bar{A}_{nj}(t, \omega) \right|^2}} \quad (4.6)$$

where $\sigma_{ii}^2(t)$ represents $(i, i)^{\text{th}}$ element of $\Sigma_{\mathbf{w}}(t)$. gPDC is equivalent to PDC when all σ_{ii}^2 are identical.

4.2.2 Reflection Coefficients and Lattice Filters

Estimating AR coefficients directly can be difficult because they are more sensitive to noise and can result in numerically unstable algorithms [79], [80]. Reflection coefficients (RCs) on the other hand are an alternative nonlinear, isomorphic parameterization of AR coefficients which are yielded by the Levinson-Durbin recursion [90], [91]. In the 1-dimensional case, RCs yielded by the Burg algorithm [92] are bounded by the interval $[-1, 1]$, which allows RCs to always produce stable AR filters. RCs

permit an efficient lattice filter implementation [91] that is readily extended into an adaptive framework. RCs are also order recursive, meaning that the next order $p + 1$ of RCs can be computed from those at the p^{th} order, whereas all AR coefficients need to be recomputed if the model order is changed.

The lattice filter at order p is represented by the following equations

$$\mathbf{f}_p(t) = \mathbf{f}_{p-1}(t) - \mathbf{K}_p^b(t)\mathbf{b}_{p-1}(t-1) \quad (4.7)$$

$$\mathbf{b}_p(t) = \mathbf{b}_{p-1}(t-1) - \mathbf{K}_p^f(t)\mathbf{f}_{p-1}(t) \quad (4.8)$$

where $\mathbf{f}_p(t)$ is the forward estimation error of order p at sample t , $\mathbf{b}_p(t)$ is the backward estimation error, $\mathbf{b}_{p-1}(t-1)$ is the delayed backward estimation error and $\mathbf{K}_p^f(t)$ and $\mathbf{K}_p^b(t)$ are the forward and backward reflection coefficient matrices, respectively.

The lattice filter can be made adaptive using a recursive least squares (RLS) algorithm, with its desirable properties such as fast convergence and tracking capability [79], [80]. In the following section we present two different versions of the RLS algorithm for adaptively tracking the forward and backward reflection coefficients throughout an epoch of the ERP signal. Then given the RCs, we can calculate the time-varying AR coefficients, which then can be used to determine the desired PDC coefficients. These in turn describe the time-evolving functional connectivities involved in the brain's processing of the ERP stimulus.

It is worthy of note that some existing versions of the RLS algorithm are based on updates of the QR decomposition via Givens rotations [93], [94] and have a complexity of $\mathcal{O}(PN^2)$ computations per time step. Our two proposed algorithms have complexities of $\mathcal{O}(PHN^2)$ and $\mathcal{O}(PN^3)$ computations per time step (H represents the number of trials), the latter exhibiting faster convergence at the expense of increased

computational demand.

4.3 Adaptive Sparse ERP Tracking (ASET) Algorithm

To develop an algorithm that is more robust to higher dimensionality and EEG background noise, the lattice filter was augmented with an exponentially decaying window, incorporating multiple ERP trials and a penalty term that enforces sparsity of the RCs. The sparsity constraint constrains the effective number of parameters to estimate.

Here we solve for all reflection coefficients by minimizing the following objective functions

$$J(\mathbf{K}_p^b(t)) = \sum_{j=1}^t \lambda^{j-1} \frac{1}{H} \sum_{h=1}^H \|\mathbf{f}_p(h, j)\|_2^2 + \gamma \|\mathbf{K}_p^b(t)\|_1 \quad (4.9)$$

$$J(\mathbf{K}_p^f(t)) = \sum_{j=1}^t \lambda^{j-1} \frac{1}{H} \sum_{h=1}^H \|\mathbf{b}_p(h, j-1)\|_2^2 + \gamma \|\mathbf{K}_p^f(t)\|_1 \quad (4.10)$$

where $p = 1, \dots, P$ represents the model order, $h = 1, \dots, H$ represents the epoch index and $j = 1, \dots, t$ represents the sample index up until the current sample t , λ represents the exponential decay parameter and γ represents the regularization parameter.

To minimize (4.9) and (4.10), we use a series of reformulations to yield a closed-form solution for the reflection coefficient estimates $\hat{\mathbf{K}}_p^b(t)$ and $\hat{\mathbf{K}}_p^f(t)$. The following algorithmic development focuses on the backward coefficients, $\mathbf{K}_p^b(t)$, for brevity. The development for the forward coefficients, $\mathbf{K}_p^f(t)$, is very similar.

Beginning with the objective function (4.9), we use the relation $\text{tr}(\mathbf{x}\mathbf{x}^T) = \|\mathbf{x}\|_2^2$,

$$\hat{\mathbf{K}}_p^b(t) = \arg \min_{\mathbf{K}_p^b} J(\mathbf{K}_p^b(t)) \quad (4.11)$$

$$= \arg \min_{\mathbf{K}_p^b} \sum_{j=1}^t \lambda^{j-1} \frac{1}{H} \sum_{h=1}^H \text{tr}(\mathbf{f}_p(h, j) \mathbf{f}_p^T(h, j)) \quad (4.12)$$

$$+ \gamma \|\mathbf{K}_p^b(t)\|_1 \quad (4.13)$$

Next, we expand the terms inside the trace using (4.7) and discard the terms that do not depend on \mathbf{K}_p^b

$$\hat{\mathbf{K}}_p^b(t) = \arg \min_{\mathbf{K}_p^b} \text{tr} \left([\mathbf{K}_p^b(t)]^T \mathbf{R}_{p-1}^{bb}(t) \mathbf{K}_p^b(t) \right. \quad (4.14)$$

$$\left. - [\mathbf{K}_p^b(t)]^T \mathbf{R}_{p-1}^{bf}(t) - [\mathbf{R}_{p-1}^{bf}(t)]^T \mathbf{K}_p^b(t) \right) \quad (4.15)$$

$$+ \gamma \|\mathbf{K}_p^b(t)\|_1 \quad (4.16)$$

where we make the following simplifying substitutions

$$\mathbf{R}_{p-1}^{bf}(t) = \sum_{j=1}^t \lambda^{j-1} \frac{1}{H} \sum_{h=1}^H \mathbf{b}_{p-1}(h, j-1) \mathbf{f}_{p-1}^T(h, j) \quad (4.17)$$

$$\mathbf{R}_{p-1}^{bb}(t) = \sum_{j=1}^t \lambda^{j-1} \frac{1}{H} \sum_{h=1}^H \mathbf{b}_{p-1}(h, j-1) \mathbf{b}_{p-1}^T(h, j-1) \quad (4.18)$$

Finally, we evaluate the trace

$$\begin{aligned} \hat{\mathbf{K}}_p^b(t) = \arg \min_{\mathbf{K}_p^b} & \sum_{n=1}^N [\mathbf{k}_{p,n}^b(t)]^T \mathbf{R}_{p-1}^{bb}(t) \mathbf{k}_{p,n}^b(t) \\ & - 2 \sum_{n=1}^N [\mathbf{k}_{p,n}^b(t)]^T \mathbf{r}_{p-1,n}^{bf}(t) + \gamma \|\mathbf{K}_p^b(t)\|_1 \end{aligned} \quad (4.19)$$

where

$$\mathbf{r}_{p-1,n}^{bf}(t) \text{ is the } n^{\text{th}} \text{ column of } \mathbf{R}_{p-1}^{bf}(t) \quad (4.20)$$

$$\mathbf{k}_{p,n}^b(t) \text{ is the } n^{\text{th}} \text{ column of } \mathbf{K}_p^b(t) \quad (4.21)$$

4.3.1 Update equations

The expressions for (4.17) and (4.18) can be rewritten in a recursive form as follows

$$\begin{aligned} \mathbf{R}_{p-1}^{bf}(t) &= \lambda \mathbf{R}_{p-1}^{bf}(t-1) \\ &+ \frac{1}{H} \sum_{h=1}^H \mathbf{b}_{p-1}(h, t-1) \mathbf{f}_{p-1}^T(h, t) \\ &= \lambda \mathbf{R}_{p-1}^{bf}(t-1) + \frac{1}{H} \mathbf{B}_{p-1}(t-1) \mathbf{F}_{p-1}^T(t) \end{aligned} \quad (4.22)$$

$$\begin{aligned} \mathbf{R}_{p-1}^{bb}(t) &= \lambda \mathbf{R}_{p-1}^{bb}(t-1) \\ &+ \frac{1}{H} \sum_{h=1}^H \mathbf{b}_{p-1}(h, t-1) \mathbf{b}_{p-1}^T(h, t-1) \\ &= \lambda \mathbf{R}_{p-1}^{bb}(t-1) + \frac{1}{H} \mathbf{B}_{p-1}(t-1) \mathbf{B}_{p-1}^T(t-1) \end{aligned} \quad (4.23)$$

where $\mathbf{F}_{p-1}(t) = [\mathbf{f}_{p-1}(1, t), \dots, \mathbf{f}_{p-1}(H, t)]_{N \times H}$ represents the concatenated forward errors of each trial, and similarly with $\mathbf{B}_{p-1}(t-1)$

4.3.2 Online coordinate descent

Next we develop an adaptive sparse algorithm to recursively compute the solution to (4.19). We follow the online coordinate descent (OCD) approach taken in [95] which updates the solution as the signal changes with time and in its regions of nonzero support. In the development below, we temporarily use the variable \mathbf{k}_n in place of $\mathbf{k}_{p,n}^b$.

Coordinate descent iteratively minimizes the objective function with respect to a single coordinate at each iteration. At iteration i , we optimize with respect to the q^{th} element of \mathbf{k}_n at sample t ,

$$k_{n,q}^{(i)}(t) = \arg \min_k J \left(k_{n,1}^{(i)}(t), \dots, k_{n,q-1}^{(i)}(t), k_{n,q}^{(i-1)}(t), \right. \\ \left. k_{n,q+1}^{(i-1)}(t), \dots, k_{n,Q}^{(i-1)}(t) \right) \quad (4.24)$$

where $q = 1, \dots, Q$, and $Q = N$ is the number of elements in \mathbf{k}_n .

Now we can reformulate the objective function, (4.19), with only the terms depending on the q^{th} element of \mathbf{k}_n . This effectively decouples the solution of $\hat{\mathbf{K}}_p^b$ into N^2 sub-problems.

$$\hat{k}_{n,q}^{\text{OCD}}(t) = \arg \min_{k_{n,q}(t)} \frac{1}{2} R_{p-1,q,q}^{bb}(t) k_{n,q}^2(t) \\ - r_{t,n,q} k_{n,q}(t) + \gamma |k_{n,q}(t)| \quad (4.25)$$

where

$$r_{t,n,q} = r_{p-1,n,q}^{bf}(t) - \sum_{s \neq q} R_{p-1,q,s}^{bb}(t) \hat{k}_s^{\text{OCD}}(t-1) \quad (4.26)$$

Solving (4.25) and (4.26),

$$\hat{k}_{n,q}^{\text{OCD}}(t) = \frac{\text{sgn}(r_{t,n,q})}{R_{p-1,q,q}^{bb}} \max(|r_{t,n,q}| - \gamma, 0). \quad (4.27)$$

$$(4.28)$$

Notice that we have substituted values of $k(\cdot)$ from the previous time step for values that have not yet been computed in the current time step.

Given $\mathbf{R}_{p-1}^{bb}(t)$ and $\mathbf{r}_{p-1}^{bf}(t)$ the complexity is $\mathcal{O}(PN^2)$. However, since the covariance update dominates, the complexity of the full algorithm is $\mathcal{O}(PHN^2)$. The complete algorithm is shown in Algorithm 1.

Algorithm 1 Online coordinate descent

```

 $q = 1$ 
for  $t = 1, \dots, T$  do
  for  $p = 1, \dots, P$  do
    Update  $\mathbf{R}_{p-1}^{bf}(t), \mathbf{R}_{p-1}^{bf}(t)$  using (4.22) and (4.23)
    for  $n = 1, \dots, N$  do
       $\hat{\mathbf{k}}_n = \hat{\mathbf{k}}_{p,n}^b(t-1)$ 
       $r_{t,n,q} = r_{p-1,n,q}^{bf}(t) -$ 
         $\sum_{s \neq q} R_{p-1,q,s}^{bb}(t) \hat{k}_{n,s}(t-1)$ 
       $\hat{k}_{n,q} = \frac{\text{sgn}(r_{t,n,q})}{R_{p-1,q,q}^{bb}} \max(|r_{t,n,q}| - \gamma, 0)$ 
       $\hat{\mathbf{k}}_{p,n}^b(t) = \hat{\mathbf{k}}_n$ 
    end for
  end for
   $q = q + 1$ 
  if  $q > N$  then
     $q = 1$   $\triangleright$  reset  $q$ 
  end if
end for

```

4.3.3 Online cyclic coordinate descent

It is also possible to update each coordinate at every sample index, which leads to the online cyclic coordinate descent (OCCD) form, (see Algorithm 2). This will increase the rate of convergence at the expense of increasing the computational complexity to $\mathcal{O}(PN^3)$. Since the relatively short duration of the ERP epoch requires fast convergence, and since this application affords off-line analysis, we choose the OCCD algorithm as the method of choice in this study. Notice that the equations for updating the k -values in the OCCD case are the same as for the OCD case.

Algorithm 2 Online cyclic coordinate descent

```

for  $t = 1, \dots, T$  do
  for  $p = 1, \dots, P$  do
    Update  $\mathbf{R}_{p-1}^{bf}(t), \mathbf{R}_{p-1}^{bf}(t)$  using (4.22) and (4.23)
    for  $n = 1, \dots, N$  do
       $\hat{\mathbf{k}}_n = \hat{\mathbf{k}}_{p,n}^b(t-1)$ 
      for  $q = 1, \dots, N$  do
         $r_{t,n,q} = r_{p-1,n,q}^{bf}(t) -$ 
           $\sum_{s \neq q} R_{p-1,q,s}^{bb}(t) \hat{k}_{n,s}(t-1)$ 
         $\hat{k}_{n,q} = \frac{\text{sgn}(r_{t,n,q})}{R_{p-1,q,q}^{bb}} \max(|r_{t,n,q}| - \gamma, 0)$ 
      end for
       $\hat{\mathbf{k}}_{p,n}^b(t) = \hat{\mathbf{k}}_n$ 
    end for
  end for
end for

```

4.3.4 Time-Varying gPDC

Finally, to compute the time-varying gPDC, we use the Levinson-Durbin recursion to convert the forward and backward RCs up to a P -th order AR model, at each time step. Then we use expressions (4.2) and (4.6) along with the innovation covariance to

compute the gPDC. The innovation covariance, $\Sigma_{\mathbf{w}}(t)$, required for gPDC is estimated by the normalized forward error covariance,

$$\begin{aligned}\hat{\Sigma}_{\mathbf{w}}(t) &= \bar{\mathbf{R}}_P^{ff}(t) \\ &= \frac{\lambda^{t-1}\mathbf{R}_P^{ff}(1) + \dots + \lambda\mathbf{R}_P^{ff}(t-1) + \mathbf{R}_P^{ff}(t)}{\lambda^{t-1} + \dots + \lambda + 1} \\ &= \frac{1 - \lambda}{1 - \lambda^t} \mathbf{R}_P^{ff}(t)\end{aligned}\tag{4.29}$$

4.3.5 Parameter Selection

The proposed method depends on proper selection of the model order, P , the exponential decay, λ , and the regularization parameter, γ .

Model order was selected based on the Exponentially-Weighted Akaike Information Criterion (EWAIC) [96], which is an adaptive version of the classic Akaike Information Criterion (AIC). The AIC considers a trade off in model fit quality and model complexity, which are represented by the first and second terms, respectively. The expression used to compute the EWAIC is defined below

$$\text{EWAIC}_f(t) = \ln \left(\frac{1 - \lambda}{1 - \lambda^t} \left| \mathbf{R}_P^{ff}(t) \right| \right) + 2 \frac{PN^2}{tH} \tag{4.30}$$

$$\text{EWAIC}_b(t) = \ln \left(\frac{1 - \lambda}{1 - \lambda^t} \left| \mathbf{R}_P^{bb}(t) \right| \right) + 2 \frac{PN^2}{tH} \tag{4.31}$$

where t represents the current sample and \mathbf{R}_P^{ff} and $\mathbf{R}_P^{bb} \in \mathbb{R}^{N \times N}$ represent the forward and backward error covariances at model order P .

There are no straightforward methods for choosing λ and γ . The exponential decay, λ , controls the tracking capability of the filter where a lower value produces quicker adaptability. However, a lower value also produces a larger variance in the

estimates. Large values of the regularization parameter, γ , increase the sparsity of the solution and decrease the variance of the parameter estimates. However, as sparsity increases, the model may underfit the data. Therefore, λ and γ should be chosen depending on the requirements of the application. Further details are given in subsequent sections.

4.3.6 Beamforming

Beamforming is used in this study to reduce the effects of volume conduction, which can give rise to spurious PDC estimates. Also, because a beamformer has the ability to “focus in” on a desired brain source thereby suppressing unwanted EEG activity from other sources, it improves the effective SNR of the respective signal. In this study, the regularized Linearly Constrained Minimum Variance (LCMV) [97] beamformer was used, where the regularization parameter was set to 1% of the average eigenvalue of the covariance matrix.

The forward head model required by the beamformer was computed from the ICBM152 Montreal Neurological Institute (MNI) template [98] to yield an anatomically correct head model. The ICBM152 template is an average of 152 normal MRI scans. This also permits use of an atlas in the MNI coordinate space to selectively partition the brain into anatomical regions which is detailed in Section 4.6.3. We also utilized the fiducials reported in [99] for the ICBM152 template. The volume conduction model was constructed using the dipoli method in FieldTrip [100], with conductivities of the scalp, skull and brain set to 0.33, 0.33/80 and 0.33, respectively.

The source model consisted of a discrete 3-dimensional grid of points with a spacing of 1cm which produced a lead field matrix at each grid point. This yielded

approximately 1800 potential sources, each corresponding to a potential input channel for our filter. The large dimensionality of this data would be unmanageable in further analysis. We therefore reduce the dimensionality of the source space using the cortical patch basis model [101], which integrates the signal over a pre-defined region (the “cortical patch”) into a single source. The patches are defined according to established anatomical regions as discussed further in Section 4.6.3. The composite measured signal $\mathbf{s}_j(k)$ over the j th patch P_j is given by the expression

$$\mathbf{s}_j(k) = \int_{\theta \in P_j} \mathbf{H}(\theta) \mathbf{m}(\theta) a(\theta, k) d\theta$$

where $\mathbf{H}(\theta)$ is the lead field matrix at a position on the cortex specified by an angular vector θ , $\mathbf{m}(\theta)$ is the source dipole moment, and $a(\theta, k)$ represents the time-variation of the source specified by angle θ . Because we have spatially discretized the problem, we can approximate the above model as

$$\begin{aligned} \mathbf{s}_j(k) &\approx \sum_{\theta_j \in P_j} \mathbf{H}(\theta_j) \mathbf{m}(\theta_j) a(\theta_j, k) \\ &= \mathbf{H}_j \mathbf{a}_j(k) \end{aligned}$$

where the θ_j are the angular coordinates that correspond to the set of grid points within patch P_j . The matrix $\mathbf{H}_j = [\mathbf{H}(\theta_1) \mathbf{m}(\theta_1), \dots, \mathbf{H}(\theta_{N_j}) \mathbf{m}(\theta_{N_j})]$ where N_j is the number of sources in the j th patch, and $\mathbf{a}_j(k) = [a(\theta_1, k), \dots, a(\theta_{N_j}, k)]^T$.

We can reduce the dimensionality of the problem by modeling \mathbf{H}_j with a low rank

approximation in the following way

$$\mathbf{H}_j \approx \mathbf{U}_j \mathbf{B}_j^T$$

where \mathbf{U}_j is a full column-rank matrix with n_j columns, and \mathbf{B}_j is a matrix of coefficients to be determined. Typically $n_j \ll n$, where n is the number of columns of \mathbf{H}_j . The received signal $\mathbf{s}_j(k)$ may then be approximated by $\hat{\mathbf{s}}_j(k)$ as

$$\begin{aligned} \mathbf{s}_j(k) &\approx \hat{\mathbf{s}}_j(k) \\ &= \mathbf{U}_j \mathbf{B}_j^T \mathbf{a}_j(k). \end{aligned}$$

The normalized mean-squared error between $\mathbf{s}_j(k)$ and $\hat{\mathbf{s}}_j(k)$ with respect to \mathbf{U}_j is minimized by choosing the columns of \mathbf{U}_j to be the n_j principal left singular vectors of \mathbf{H}_j . To apply the patch basis model as part of the LCMV beamformer refer to eqs. (17-19) in [101].

In summary, the proposed algorithm adaptively tracks gPDC parameters within the time frame of an ERP epoch and thus allows us to track the brain network involved in the processing of the ERP stimulus. First, the raw electrode signals are processed through a network of multiple beamformers that isolate brain source signals emitting from a contiguous set of regions of the cortex. These beamformer outputs are then modelled as a time-varying multi-channel AR process, realized in a least-squares lattice configuration. The respective time-varying reflection coefficients are transformed into AR coefficients, from which the time-varying gPDC coefficients are obtained. The gPDC coefficients represent the directed information flow between brain sources and thus indicate functional connectivity. The method incorporates

averaging over multiple epochs so that the ERP signal components are added coherently, whereas the background EEG components add incoherently. This, in addition to the beamforming operation, increases the SNR of the ERP signal to acceptable levels. Sparsity regularization is also incorporated to improve stability of the gPDC estimates. Time adaptation is performed in an OCCD framework which updates all elements of the forward and backward reflection coefficient matrices in each time step over the ERP epoch. We refer to the proposed method as the *adaptive sparse ERP tracking* (ASET) algorithm.

4.4 Simulations

We compare the performance of the ASET algorithm to the multi-channel QRDLSL (MQRDLSL) [93], [94] and the multi-channel multi-trial QRDLSL (MCMTQRDLSL) lattice filter algorithms. Adaptation in time of the MQRDLSL method is based on the QR decomposition of the forward and backward error matrices. The MCMTQRDLSL method is a multi-trial extension of the MQRDLSL algorithm where the covariance matrix updates include information from multiple ERP trials.

The data used for the comparison was a simulated stationary 10 channel VAR(8) process. The VAR process was specified by sampling RC values from a uniform distribution, $\mathcal{U}(-1, 1)$, and according to specific coefficient sparsity parameters. Each co-channel VAR process was created such that 40% of the RCs were non-zero. The cross-channel RC coefficients were selected such that 5% of the RCs were non-zero.

The VAR data was generated by reconfiguring the lattice filter to become an VAR synthesizer utilizing the RC coefficients generated in the previous step, as described in [102, pg. 179]. The configuration is represented by the following equations, which

are nearly identical to (4.7)

$$\mathbf{f}_{p-1}(t) = \mathbf{f}_p(t) + \mathbf{K}_p^b(t)\mathbf{b}_{p-1}(t-1) \quad (4.32)$$

$$\mathbf{b}_p(t) = \mathbf{b}_{p-1}(t-1) - \mathbf{K}_p^f(t)\mathbf{f}_{p-1}(t) \quad (4.33)$$

The filter input, $\mathbf{f}_p(t)$, is fed white noise and the output, $\mathbf{f}_0(t)$, produces the VAR process.

The white noise was sampled from a $\mathbf{w} \sim \mathcal{N}(\mathbf{0}, 0.1\mathbf{I})$ normal distribution.

4.4.1 Reflection Coefficient MSE

We compare the performance of the ASET algorithm as described by the mean squared error (MSE) of the estimated RC values in Figure 4.1. We also compared the performance to the Nuttall-Strand algorithm, which produces a single estimate of the RCs with all 1000 samples. The MSE in Figure 4.1 is an average of 5 simulation runs. The filter parameters were identical for all filters. The model order was set to 8 and γ was tuned to 4.55 in order to minimize the MSE of the estimated RC values. The parameter H , the number of averaged trials, is 5. We also compared the steady state performance of the ASET algorithm for 2 values of $\lambda = 0.9, 0.99$.

4.4.2 Reflection Coefficient Sparsity

We further compare the MSE performance when the reflection coefficient sparsity level changes in the underlying VAR process in Figure 4.2. VAR processes were generated as described earlier, except with a change in the percentage of non-zero cross-channel RC coefficients. The following percentages were used: 1, 5, 10, 20, 50 and 80. The

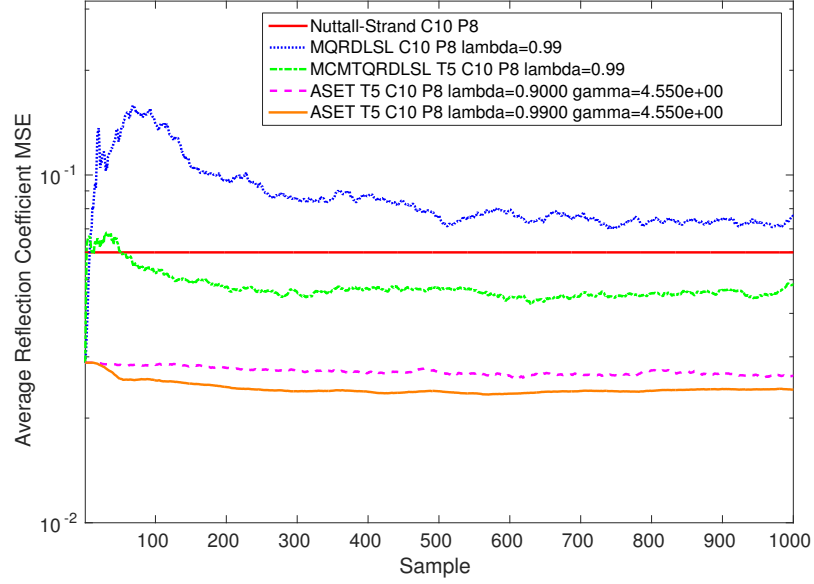


Figure 4.1: Average MSE performance of the ASET algorithm vs. QRD-based methods

MSE in Figure 4.2 is an average of 5 simulation runs. Again, H is set to 5 and λ is set to 0.99.

We can see from Figure 4.1 and Figure 4.2 that the ASET algorithm performs significantly better than its QRD counterparts, both from the speed of convergence and MSE perspectives. From Figure 4.1, we can see that the performance of ASET is roughly 1/3 of an order of magnitude improved over that of the MCMTQRDLSL method. The ASET algorithm is capable of providing good RC estimates with very few samples, especially when compared with the Nuttall-Strand algorithm. This improvement is due in part because ASET can exploit the sparsity inherent in the problem. Also apparent from the QRD curves is the performance improvement due to averaging over multiple trials. Also we see from Figure 4.2 that the performance of ASET exceeds the QRD methods by roughly half an order of magnitude, particularly for high sparsity levels (i.e. a low number of non-zero coefficients).

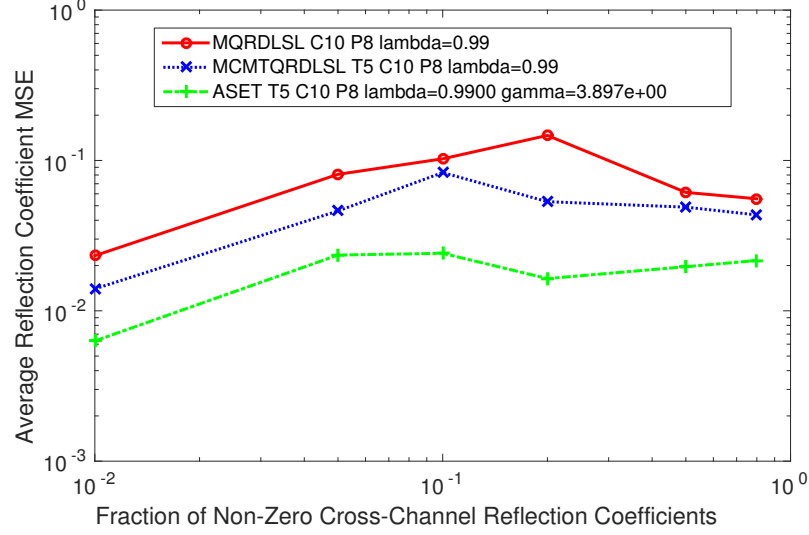


Figure 4.2: Average steady-state MSE performance of filters as a function of reflection coefficient sparsity.

4.5 Surrogate Data Analysis

The noisy nature of the ERP data can give rise to false positives in the gPDC estimates. It is therefore necessary to devise a statistical test to determine whether the estimated gPDC coefficients values are significant. In this vein we use numerical methods based on surrogate data [103] to determine a 95% threshold value on the distribution of the gPDC coefficients under the null hypothesis. It therefore follows that any estimated gPDC value produced by the ASET algorithm above this threshold is statistically significant.

Although the theoretical distribution of the gPDC has been derived previously when no coupling is present [104], these results may be unreliable in our scenario due to the non-stationarity of ERP data. When generating surrogate data, it is important to only modify the property of the signal that forms the basis of the null hypothesis and maintain all other properties of the signal being investigated.

We evaluate the significance of the results under the “no-coupling” null hypothesis which is explained below.

4.5.1 Null hypothesis: No coupling

Many methods that generate surrogate data assume stationarity and are thus inappropriate in this scenario [103], [105], [106]. An implicit assumption in dynamic connectivity estimation is the non-stationarity of the ERP data over time. Accordingly, the null hypothesis is modelled by a tvVAR process to fully preserve the spectral properties of the ERP data, following a similar approach to [107]. We take the “no coupling” null hypothesis to correspond to the case where VAR cross-channel coefficients are zero. In this case the true cross-channel gPDC coefficient values are also zero.

The surrogate data is generated on the basis of the real experimental data described in Section 4.6.2. We used the ASET algorithm to estimate the multichannel tvVAR coefficients from this data, where in the surrogate case, each channel is processed individually as a single-channel AR process. Thus we estimate multiple single-channel AR processes instead of a single multi-channel process, where cross-couplings are ignored. To generate data for the null hypothesis, we assign the estimated RCs into each respective channel. This produces a tvVAR process where all the cross-channel coefficients, and hence the corresponding gPDCs, are zero. The surrogate data itself was then generated from this tvVAR model according to (4.32) and (4.33) as described in Section 4.4.

The driving white noise was sampled from a normal distribution with zero mean and a diagonal covariance scaled by the power of the forward estimation errors of the

originally filtered data, as shown in (4.34).

$$\mathbf{w}_j(k) \sim \mathcal{N}(\mathbf{0}, \mathbf{C}_w) \quad (4.34)$$

$$\mathbf{C}_w = \text{diag}(\sigma_1^2, \dots, \sigma_n^2, \dots, \sigma_N^2) \quad (4.35)$$

$$\sigma_n^2 = \text{var}(f_{P,n}(k)) \quad (4.36)$$

$$k = 1, \dots, K, \quad n = 1, \dots, N$$

where j is the index for the surrogate sample and k is the time index. Surrogate data analysis was conducted with 100 surrogate data series and a significance level of $\alpha = 0.05$.

This surrogate data was then analyzed by the standard ASET algorithm where the cross-channel couplings were not constrained to zero. An approximation to the underlying gPDC distribution under the null hypothesis can be obtained from the estimated gPDC values in the form of a histogram. From this, the threshold for a significance level of $\alpha = 0.05$ was computed for each data point at all frequency bins, time samples and channels. Thus by selecting only gPDC values above the threshold, we are 95% confident the estimates are significant.

An example of the distribution of gPDC between regions is shown in Figure 4.3. The specific anatomical pair and time sample was selected based on the largest threshold produced by the steps described above to show the distribution underlying the most conservative threshold level. The null hypothesis is readily shown by the high concentration of small gPDC values.

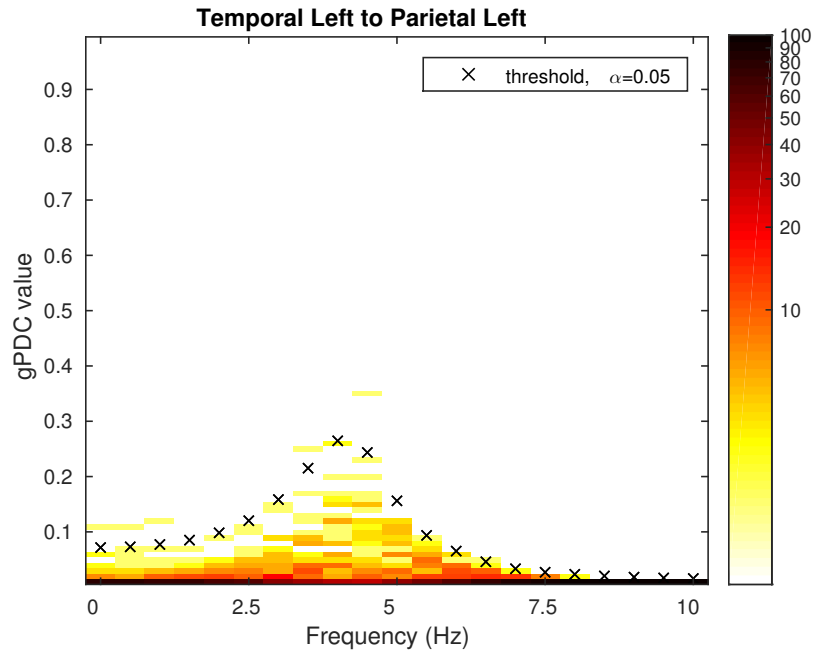


Figure 4.3: Histogram of cross-channel gPDC values under the null hypothesis for 100 realizations of surrogate data when $t = 367\text{ms}$ and for frequencies between 0-10Hz. The number of elements is represented by a color map, where the hotter color represents a higher number. The resulting thresholds for each frequency are marked by \times . The anatomical region pairs and time sample were selected based on the largest threshold.

4.6 Application

4.6.1 Background

Cognitive prediction of upcoming events hinges on the ability to extract temporal regularities from external stimuli [108], [109]. This predictive timing is essential for many human behaviors including understanding speech and music. Predictive timing is achieved through the process of entrainment, where neural oscillations synchronize with temporally regular external stimuli. It is common knowledge that auditory rhythm and rhythmic movement go hand in hand; however, the underlying neural mechanisms of auditory-motor communication are poorly understood. It has been observed that the *modulation* of β amplitude follows the tempo of sound stimulation [108]. β -band oscillations also reflect change in the status of sensorimotor functions and do not require movement to be present [108]. In the following sections we use the ASET algorithm to further study the dynamic relationship between the auditory cortex and all other regions of the brain, specifically with respect to networks formed from the amplitude modulation of β -band oscillations.

4.6.2 Methods

We applied the ASET algorithm to ERP data collected during an auditory oddball sequence which consisted of an isochronous stream of standard and deviant tones. Piano tones C4 (262Hz) and B4 (494Hz) were used as the standard and deviant tones, respectively. The inter-onset interval was set to 500ms and 3600 tones were presented in each session where the deviant tone had an occurrence rate of 10%. The EEG was sampled at 2048Hz (filtered DC to 417Hz) using a 128-channel Biosemi Active Two

amplifier (Biosemi B.V., Amsterdam). The electrode array positions were digitized using an electromagnetic position tracking system (Polhemus Fastrak) prior to EEG collection and the data was referenced to the vertex electrode. Further details are given in [109].

The ERP data was preprocessed in a similar fashion as in [109]. In order to remove data with artifacts, the *raw continuous* ERP data was filtered using a 3rd order Butterworth band pass filter (1-60Hz). The filtered data was segmented into long epochs of -500 to 1000ms, where 0ms represents the stimulus onset, resulting in a segment containing 3 contiguous ERP trials. According to this filtered data, any epochs where the signal exceeded a threshold of $60\mu V$, with respect to the baseline signal between -100-0ms for more than 10% of the epoch, were rejected from the β -band filtered data. To extract the β -band data, the *raw continuous* data was band pass filtered with a 4th order Butterworth filter (15-25Hz) and epoched. We only considered sequences that contained 3 consecutive standard tones.

Next, the data was preprocessed prior to application of the ASET algorithm. Since in this study we consider networks formed from the envelope of the β -band signal, the envelope was extracted by computing the magnitude of the analytic signal using the Hilbert transform and the mean was removed. Extracting the envelope in this manner avoids producing edge artifacts at the first sample of the actual data. Each channel was then normalized to unit variance.

4.6.3 Anatomical Segmentation

The Automated Anatomical Labelling (AAL) atlas was utilized to produce anatomically labelled patches [110]. By using standardized anatomical regions, the atlas

provides a means to reduce anatomical variability between subjects. The atlas contains 116 anatomical regions and is specified in the MNI coordinate space. These regions of the atlas were grouped into gross anatomical regions for both left and right hemispheres. The gross regions considered are: prefrontal cortex (PFC), motor cortex (MC), basal ganglia, insula, parietal cortex (PC), temporal cortex (TC), occipital cortex (OC), limbic, cerebellum as well as an additional medial cerebellum region. Since in general a beamformer's ability to isolate deep sources decreases with depth, certain regions were excluded from the remaining analysis. The excluded regions include: basal ganglia, insula, limbic and cerebellum. Furthermore, to enhance the interpretation of the connectivity analysis in relation to the auditory cortex (AC), both left and right AC were included as independent regions and mutually exclusive to all other regions. The AC region was specified as a sphere with a radius of 2cm with the center determined by source localization of the subject specific P1 response as described in [109].

The subsequent connectivity analysis treats each hemisphere separately since the literature suggests only low levels of cross-hemispheric communication in auditory processing [29]. This procedure significantly reduces the number of cross-channel coefficients that require estimation.

4.6.4 Dynamic Connectivity Estimation

The ASET algorithm explained in Section 4.3 was used to estimate the reflection coefficients. In order to minimize the filter initialization effects, the source space signals were prefixed with a temporally reversed copy of itself. In this way the initial value of covariance estimate for the RC estimation process would approach the covariance

matrix at the first sample of the actual data. After the application of the ASET algorithm, this prefixed data is discarded and only the second half of the data is considered when computing the gPDC.

As an additional topic of interest, we also applied the ASET algorithm to the β signal itself, rather than only to the envelope of the β -band signal.

The exponential decay parameter, λ , was chosen as 0.99 in order to reduce the variance of the filter output. Since the signal was oversampled relative to the β -band and its envelope, there was little concern with a reduction of tracking capability with a relatively high λ . Further, values of $H = 20$, $H = 100$ and $H = 195$ epochs (as in (4.22) and (4.23)) were used in the analysis. Analysis for the β band signal itself use values $H = 20, 100$, whereas since the β -band envelope is a noisier signal, values $H = 100, 195$ were used in this case. The filter was evaluated over a few values of the regularization parameter, $\gamma = 1e-3, 1e-4, 1e-5$ and $1e-6$. The final choice of γ was based on the percentage of results surviving the surrogate analysis step since a high percentage indicates more stable results. For $H = 20$, we considered the additional criteria of similarity to the gPDC results when $H = 100$. The final choice for γ for all of the analyses utilized $\gamma = 1e-5$.

An AR model order of 6 was selected for both right and left hemispheres for the β -band signal and order 5 was selected for the β -band envelope according to the procedure described in Section 4.3.5.

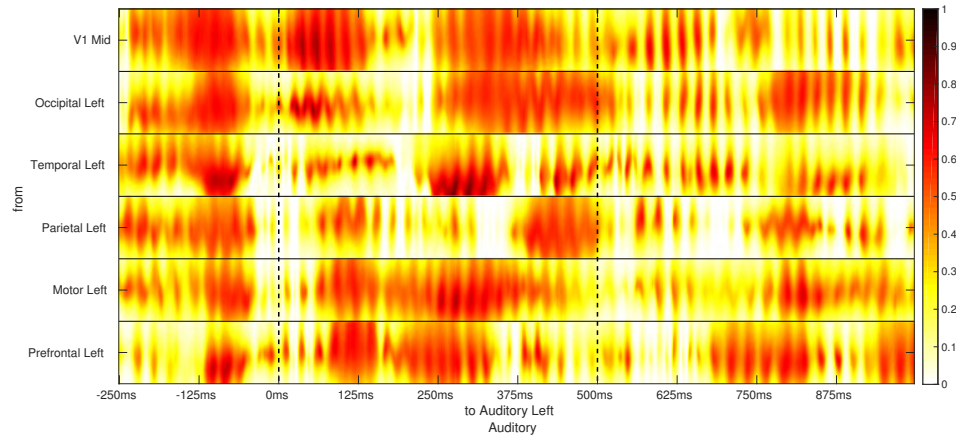
The estimated reflection coefficients were then used to compute the gPDC. The reflection coefficients were first downsampled by a factor of 4 in the temporal domain and the gPDC was computed for 2048 frequency bins.

4.6.5 Results

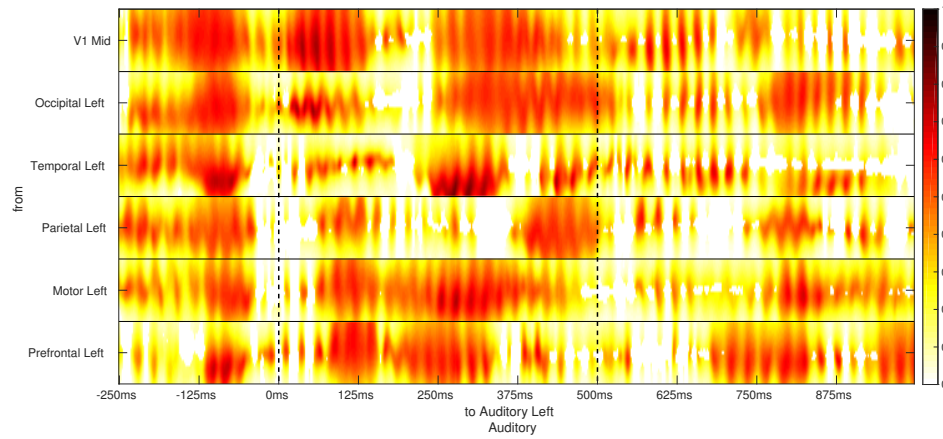
The auditory experimental protocol is designed for the study of the flows into and out of the AC and its associated regions. We also observed stronger gPDC flows in the left hemisphere. In this respect, we focus on the dynamic gPDC from various channels to the left AC and the left TC.

The time-frequency plots of Figures 4.4, 4.5, 4.7 and 4.8 give a partial depiction of the evolution of the dynamic neural networks that are active in the processing of auditory stimuli. Figures 4.4 and 4.5 show gPDC flows for the β -band signal itself, whereas Figures 4.7 and 4.8 show gPDC flows corresponding to the β -band *envelope* signal. A complete representation of flows would require a plot “to” each of the seven brain regions – in this study we show only the most significant gPDC flows for the sake of brevity. Nevertheless, from the selected figures it is possible to discern the dynamic behaviour of the various connections at play. Each horizontal band represents the dynamic gPDC estimate in a specific frequency range oriented with the smallest frequency at the top of the band. The frequency range of 15-25Hz and 0-10Hz are used in Figures 4.4 and 4.5 and Figures 4.7 and 4.8, respectively. They show the gPDC flowing from the anatomical region indicated on the left axis to the anatomical region indicated on the bottom axis. Of the three consecutive standard trials, the figures show only the second half of the first trial (-250-0ms) and the full second (0-500ms) and third trials (500-1000ms). This is due to lack of filter convergence as well as the effects of the trial preceding the first trial under study which can take the form of a standard or deviant trial. The dashed lines represent the onset of the auditory stimulus.

Figures 4.4 and 4.5 show the gPDC flows resulting from β -band activity itself.

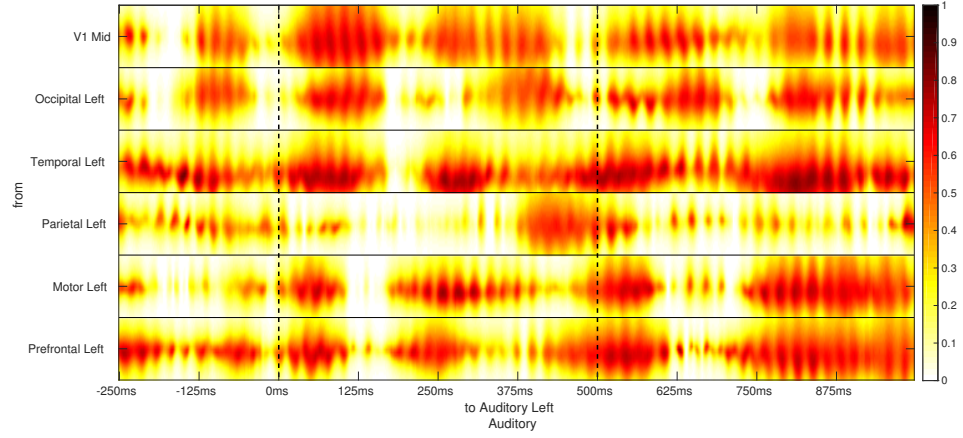


(a) gPDC flows to Left Auditory Cortex

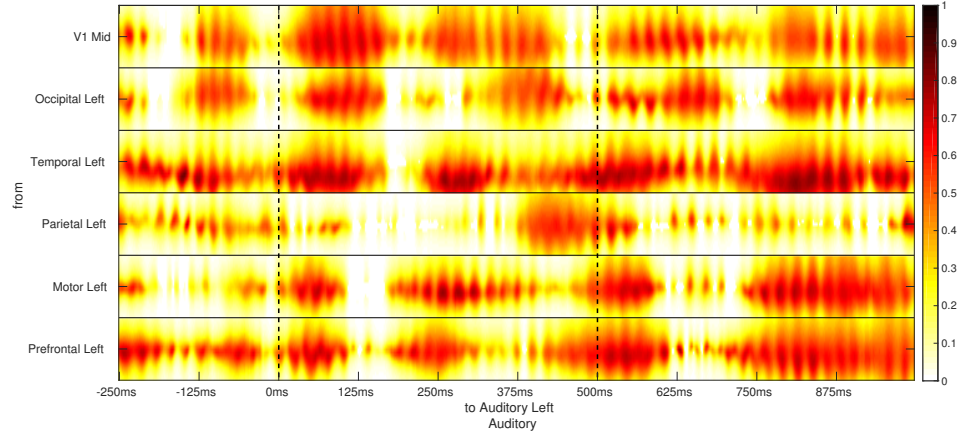


(b) Thresholded gPDC flows to Left Auditory Cortex according to the “no-coupling” null hypothesis

Figure 4.4: Comparison of gPDC (4.4a) and thresholded gPDC ($\alpha = 0.05$) (4.4b) flows to the left auditory cortex corresponding to the β -band activity itself, with parameters $H = 20$, model order 6, $\gamma = 1e - 5$ and $\lambda = 0.99$. Each horizontal band represents the gPDC between 15-25Hz (oriented from top to bottom) and across time -250ms to 1000ms. The magnitude of the gPDC is defined by the intensity of the color. The dashed lines mark the stimulus onset.



(a) gPDC flows to Left Auditory Cortex



(b) Thresholded gPDC flows to Left Auditory Cortex according to the “no-coupling” null hypothesis

Figure 4.5: Same as Figure 4.4 except $H = 100$.

Figure 4.4 shows the overall gPDC flows to the left AC when considering 20 epochs, ($H = 20$), and compares the effects of the surrogate data analysis. Overall, there are minimal differences between the original gPDC estimate (Figure 4.4a) and the thresholded gPDC estimate (Figure 4.4b). Figure 4.5 further compares the same activity and analysis when considering 100 epochs ($H = 100$). Despite the lower number of epochs used in the analysis, Figure 4.4 shows very similar gPDC activity as Figure 4.5. When $H = 100$, there is generally higher resolution in both the time and frequency dimensions.

These figures show the periodic bands of coherent activity on a number of scales. E.g., Figure 4.4 shows about 40 local gPDC peaks within a 1-second interval, corresponding to the 20 Hz centre frequency of the β -band signal, since there are both a positive and a negative peak per cycle. These peaks are also surprisingly synchronous with the stimulus. Figure 4.5 shows a clear picture of temporal variation in the gPDC of a single band over the evolution of an ERP. The temporal variation is also very similar between trials resulting from the same stimulus. The gPDC flow of β -band activity to the AC is significant from all anatomical regions. The TC produces the strongest gPDC flow and the PC produces the weakest.

Figure 4.6 shows the mean and standard deviation of the gPDC from the left TC to the left AC at a single time sample, $t = 781\text{ms}$, over 100 different permutations of epochs compared with the thresholds produced by surrogate analysis with the “no coupling” null hypothesis. When $H = 20$, the standard deviation is approximately 3 times as large as when $H = 100$. Furthermore, for the $H = 100$ case, the gPDC values are more concentrated around their centre frequency of 20 Hz, indicating higher resolution in frequency in this situation. The standard deviation in Figure 4.11 is

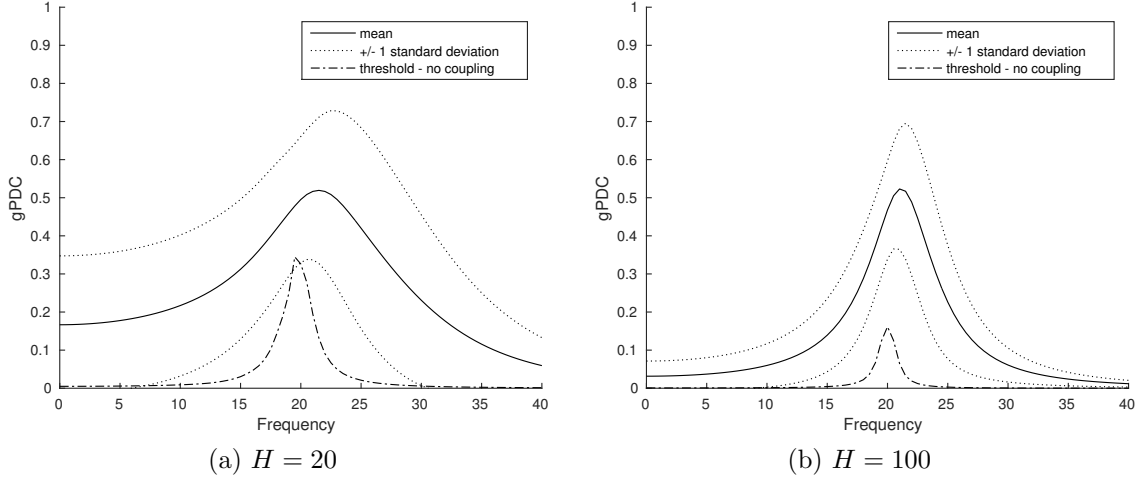
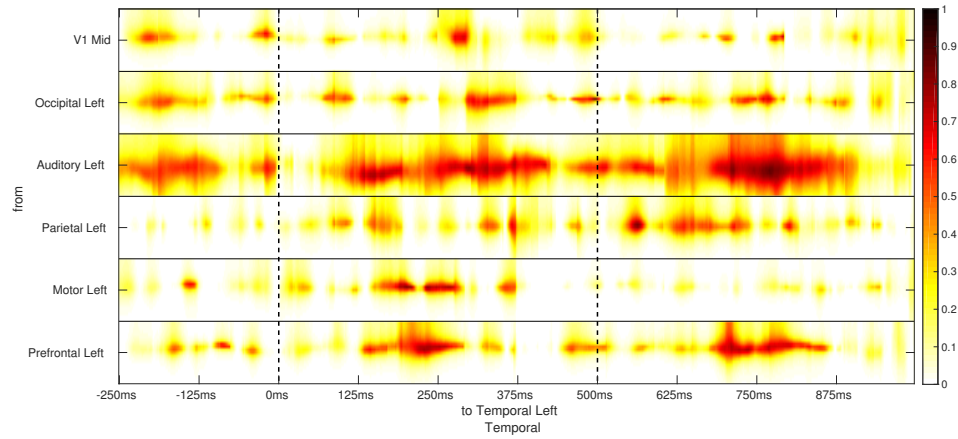


Figure 4.6: Mean and ± 1 standard deviation of gPDC flows from the left Temporal Cortex to the left Auditory Cortex at $t = 781\text{ms}$, corresponding to Figure 4.4 and Figure 4.5, in comparison with the thresholds produced by surrogate analysis with the “no coupling” null hypothesis.

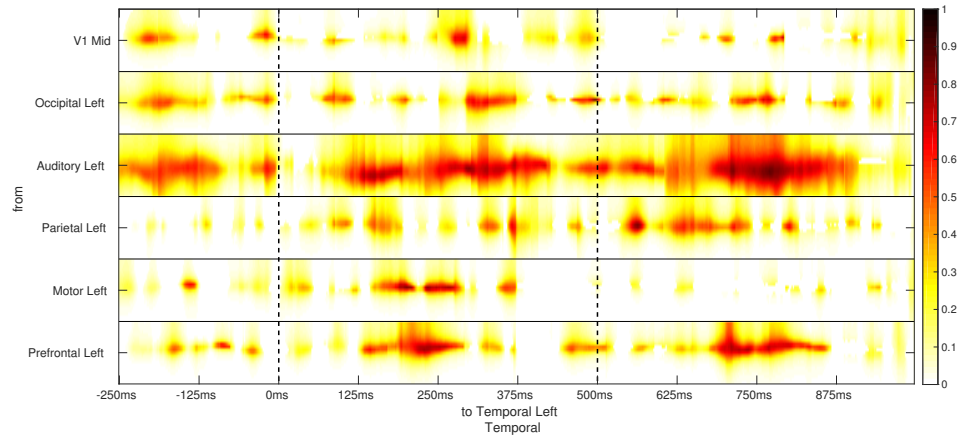
comparable to the results in [105]. More importantly, the $H = 100$ case shows that the $\pm 1\sigma$ band is well separated from the surrogate threshold, indicating that the gPDC estimates in this case are indeed stable.

From this point onwards in this presentation, we shift our focus to the analysis of the β -band envelope using $H = 100$ and $H = 195$, rather than the analysis of the β -band signal itself, which used $H = 20$ and $H = 100$. In this case, the frequency band of interest of the envelope signal is from 0 - 10 Hz. In this vein, Figure 4.7 shows the effect of the thresholding resulting from the surrogate data analysis, for gPDC flows to the left TC for $H = 100$ epochs.

The effect of thresholding can be seen by comparing Figure 4.7a to Figure 4.7b. It can be seen that practically all of the gPDC activity does exceed the threshold value, again indicating the statistical significance of these estimated gPDC values. The fact we have presented evidence that the results are significant suggests that

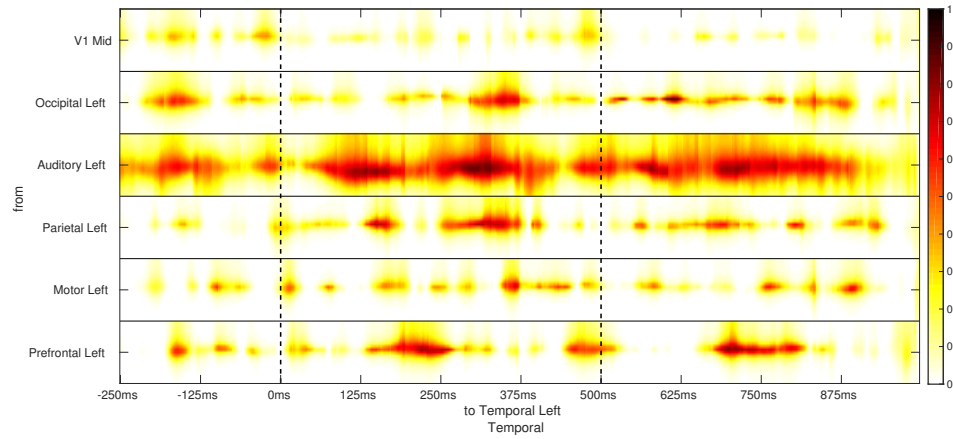


(a) Unthresholded gPDC flows to Left Temporal Cortex

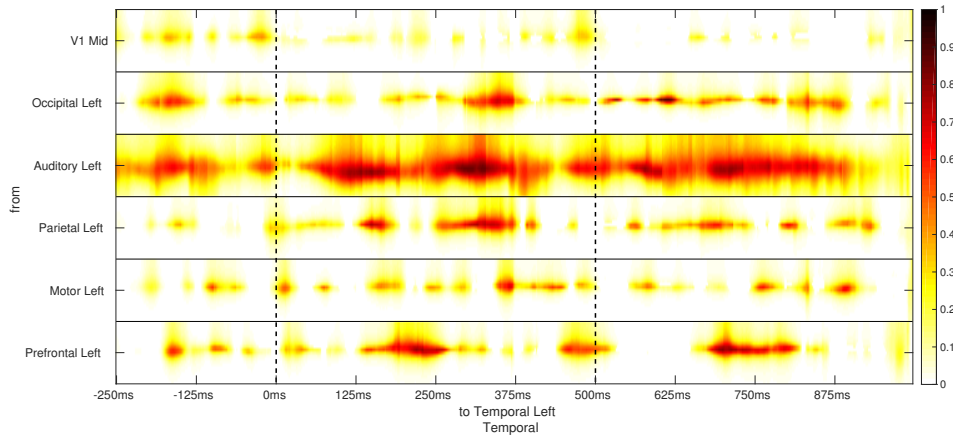


(b) Thresholded gPDC flows to Left Temporal Cortex according to the "no-coupling" null hypothesis

Figure 4.7: Comparison of gPDC (4.7a) and thresholded gPDC ($\alpha = 0.05$) (4.7b) flows to the left temporal cortex for the β -band envelope, with parameters $H = 100$, model order 5, $\gamma = 1e - 5$ and $\lambda = 0.99$. Each horizontal band represents the gPDC between 0-10Hz (oriented from top to bottom) and across time -250ms to 1000ms. The magnitude of the gPDC is defined by the intensity of the color. The dashed lines mark the stimulus onset.



(a) Unthresholded gPDC flows to Left Temporal Cortex



(b) Thresholded gPDC flows to Left Temporal Cortex according to the “no-coupling” null hypothesis

Figure 4.8: Comparison of gPDC (4.8a) and thresholded gPDC ($\alpha = 0.05$) (4.8b) flows to the left temporal cortex for the β -band envelope, with parameters $H = 195$, model order 5, $\gamma = 1e - 5$ and $\lambda = 0.99$. Each horizontal band represents the gPDC between 0-10Hz (oriented from top to bottom) and across time -250ms to 1000ms. The magnitude of the gPDC is defined by the intensity of the color. The dashed lines mark the stimulus onset.

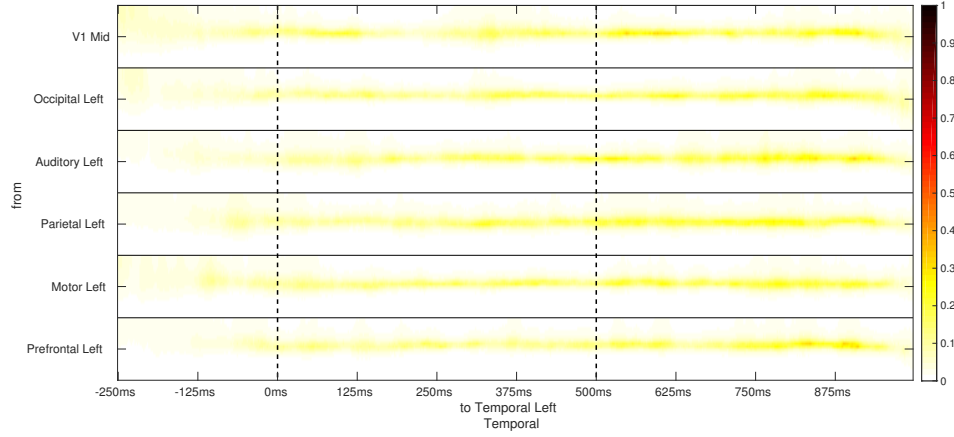


Figure 4.9: Threshold for gPDC flows to the left temporal cortex (TC) for $H = 100$ with respect to the “no coupling” null hypothesis. Each horizontal band represents the gPDC between 0-10Hz (oriented from top to bottom) and across time -250ms to 1000ms. The magnitude of the gPDC is defined by the intensity of the color. The dashed lines mark the stimulus onset.

the proposed methodology warrants further investigation of the β -band connectivity behaviour from a neuroscience perspective.

Figure 4.8 presents the same comparison of the dynamic gPDC flows as Figure 4.7 except in this case, $H = 195$ epochs. gPDC flow to the left TC mainly originates from the AC and PFC with minor contributions from the MC, PC, OC and V1. The contributions from the AC and PFC are also very similar between trials. On the other hand, the gPDC flow from the MC is different between trial 2 and trial 3. This issue is further investigated in Figures 4.10 and 4.11. The main similarity with Figure 4.7 is the pronounced gPDC flow to the AC and PFC.

Overall, the results for $H = 100$ resemble those for $H = 195$, and consequently we may infer that the selected values for the filter parameters, λ and γ , are suitable for this application.

Figure 4.9 shows the threshold values used in Figure 4.7 as a function of time and

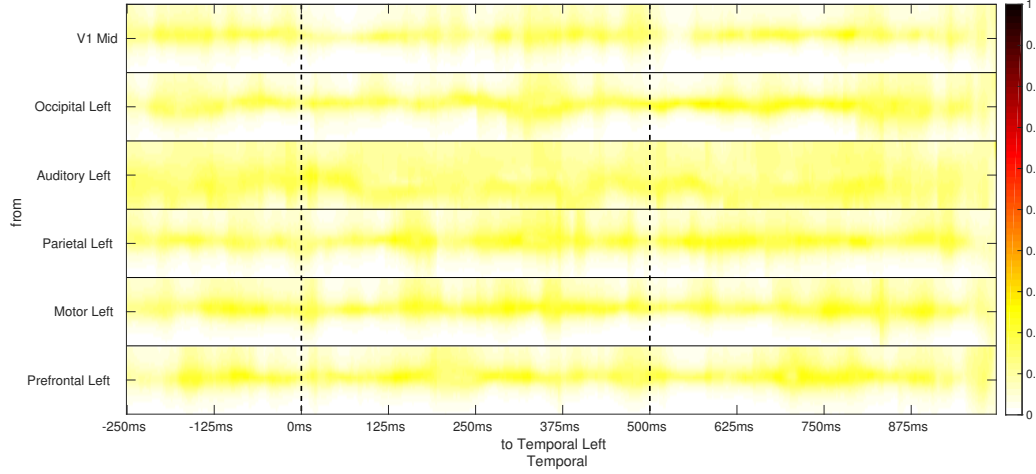


Figure 4.10: Standard deviation of gPDC flows to the left temporal cortex (TC) for $H = 100$. The standard deviation is computed from 100 runs of the ASET algorithm using a different permutation of ERP trials for each run. Each horizontal band represents the gPDC between 0-10Hz (oriented from top to bottom) and across time -250ms to 1000ms. The magnitude of the gPDC is defined by the intensity of the color. The dashed lines mark the stimulus onset.

frequency. The “no coupling” threshold (Figure 4.9) tends to be non-zero only around the most dominant frequency and very small elsewhere. Since the null hypothesis produces small thresholds, we see again that the ASET algorithm, with the specific choice of parameters used, tends to produce statistically significant estimates.

To further evaluate the stability of the gPDC estimates, Figure 4.10 shows the standard deviation of the dynamic gPDC flow to the left AC over 100 different permutations of epochs. Each permutation is a random selection of H epochs from the preprocessed ERP data. In the case of $H = 100$ (Figure 4.10), the standard deviation does not exceed 0.15 with an average value of 0.0547 and is mostly concentrated around the 5Hz band. The average σ -value of 0.0547 suggests that the results of e.g. Figure 4.7 are an accurate depiction of the gPDC flow in this case. The average standard deviation over all samples and all anatomical pairs is 0.0331. Similar or better

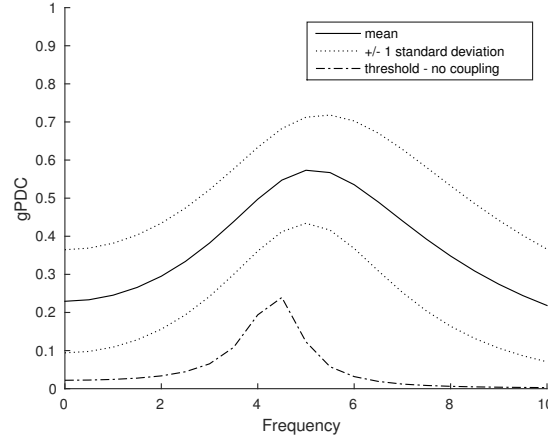


Figure 4.11: Mean and ± 1 standard deviation of gPDC flows for $H = 100$ from the left Auditory Cortex to the left Temporal Cortex at $t = 781\text{ms}$ in comparison with the threshold produced by surrogate analysis with the “no coupling” null hypothesis.

results were observed for other seed locations. There were not enough epochs to produce the same analysis with $H = 195$ since only 195 epochs survived the preprocessing steps for this specific subject.

To further place the thresholds and standard deviation into perspective, Figure 4.11 shows the mean and standard deviation of the gPDC from the left AC to the left TC at a single time sample, $t = 781\text{ms}$, over 100 different permutations of trials compared with the thresholds produced by surrogate analysis with the “no coupling” null hypothesis. There are similarities to Figure 4.6, (which shows β -band activity itself, rather than β -band envelope activity) namely, the dispersion of the gPDC centered around a peak at approximately 5Hz. The dispersion about the mean is larger for the β -envelope case; this shows that the gPDC coefficients from the β -envelope signal are noisier than those from the β signal itself. There were not enough epochs to produce the same analysis with $H = 195$.

Since the subjects were not engaged in any active tasks during the data collection

process, the attention of the subjects may not be uniform over the entire experiment. This lack of attention could be a factor leading to the significant levels of inter-trial variability as demonstrated in e.g., Figure 4.7. Nevertheless, Figure 4.10 indicates that the variance over different permutations of epochs is reasonable. Figure 4.11 further demonstrates that the distribution of gPDC is well separated from the surrogate analysis threshold. The inter-trial variability diminishes as more epochs are utilized in the analysis, e.g., Figure 4.8.

Figure 4.12 summarizes the gPDC connectivity between all anatomical regions in the left (Figures 4.12a and 4.12c) and right hemispheres (Figures 4.12b and 4.12d) utilizing $H = 100$ and 195 epochs. A gross connectivity model from Figures 1 and 5 of [29] is replicated in Figure 4.12e for ease of comparison. The dynamic gPDC is summarized by taking the mean of the gPDC over the frequency range of 0-10Hz and over time between -127ms to 1000ms.

In the left hemisphere (Figures 4.12a and 4.12c), gPDC flows mostly to the TC and some to the AC and OC. gPDC flows to the TC are mainly from the AC with minor contributions from the PFC, PC and OC. In the right hemisphere (Figures 4.12b and 4.12d), gPDC flows mostly to the AC originating from the PFC, MC, PC and TC. There are reciprocal gPDC flows between the OC and V1 and from the AC to the PFC.

Figure 4.13 compares the overall gPDC connectivity patterns for 2 of the subjects of the subjects studied, for $H = 195$. Comparing the gPDC flows in the left hemisphere (Figures 4.13a and 4.13c), there are strong similarities in the gPDC flows to the TC from the AC, PFC, PC and OC. Subject 5 shows a few more strong flows from the TC to the AC as well as from the MC to the AC and TC. Similarly, comparing the

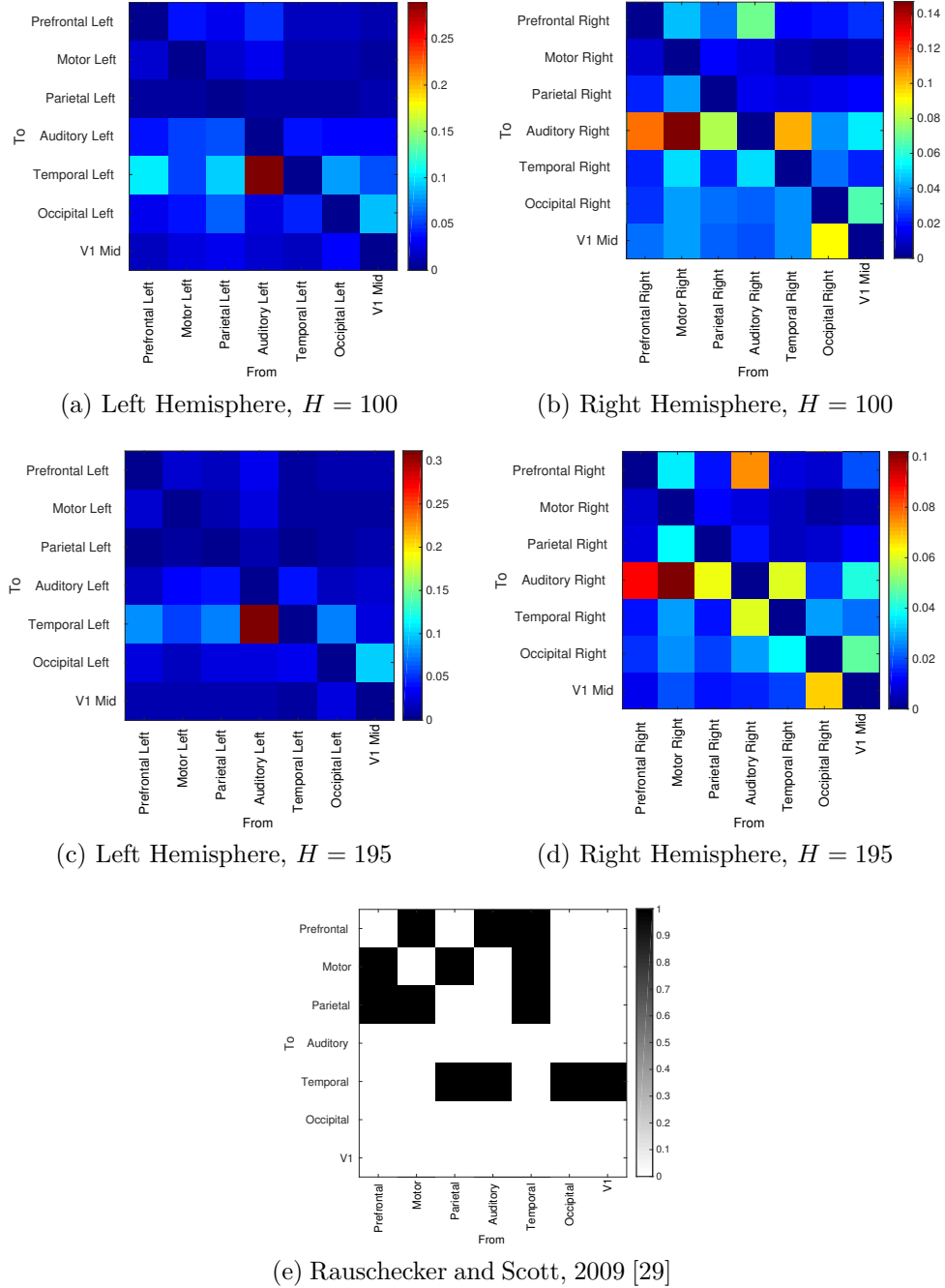


Figure 4.12: Summary of connectivity between anatomical regions in each hemisphere. The summary is computed by taking the mean of the gPDC over the frequency range of 0-5Hz and over time between -127ms to 1000ms.

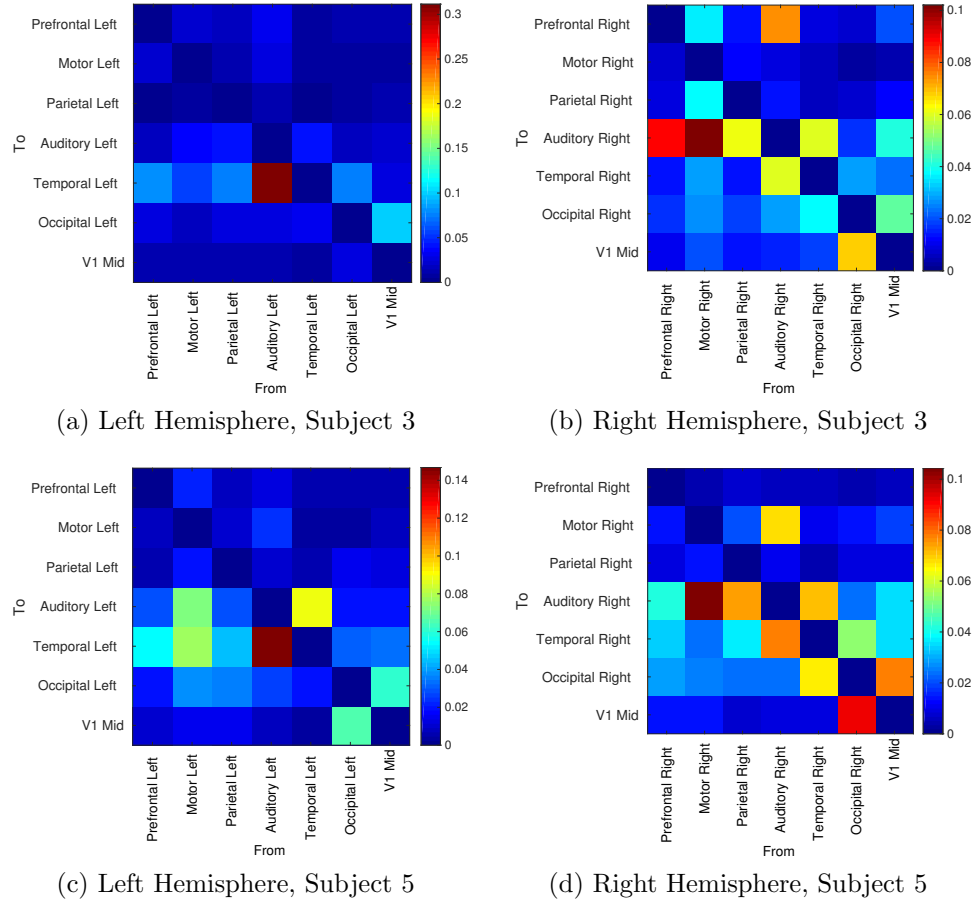


Figure 4.13: Summary of connectivity between anatomical regions in each hemisphere for 2 subjects for $H = 195$. The summary is computed by taking the mean of the gPDC over the frequency range of 0-10Hz and over time between -127ms to 1000ms.

gPDC flows in the right hemisphere (Figures 4.13b and 4.13d), both subjects show strong flow to the AC from the MC, PC and TC, from AC to TC, and reciprocal flows between OC and V1. Subject 5 shows additional gPDC flow from the TC to OC, and AC to MC.

4.6.6 Discussion

It is difficult to directly validate the observed gPDC flows with a model of human processing of auditory stimuli in the literature since the activity may differ based on the experimental protocol, the chosen frequency range under study and whether the envelope of the signal is of greater interest. Nevertheless, [29] has proposed a model based on nonhuman primates that describes human speech processing which can serve as a reasonable comparison. The model describes a dual processing scheme that is divided into “what” and “where” pathways (see Figure 1 in [29]). The simplified “what” pathway travels from AC through the superior temporal (ST) region and the ventrolateral prefrontal cortex (VLPFC). The ST region also provides input to the VLPFC. The simplified “where” pathway travels from AC to the posterior parietal cortex (PPC) and the dorsolateral prefrontal cortex (DLPFC). The PPC also provides input to the DLPFC. The visual pathway has a similar organization as well. The primary visual cortex (V1) provides input to the inferior temporal (IT) region and the PPC for the “what” and “where” pathways, respectively. The results shown in Figure 4.12 show similarities in the active regions, namely AC, PFC, PC and TC. Our results show involvement of the MC as well which is also mentioned in [29] (see Figure 5 in [29]).

Our results show some agreement with the more expanded connectivity scheme of

Figure 5 in [29], which is summarized in Figure 4.12e. Comparing the connectivity for $H = 195$ in the left hemisphere (Figure 4.12c), gPDC flows mainly to the TC and shows some agreement with the expected activity from the proposed model. There is some gPDC flow from the PFC to the TC that is not indicated by the model. Comparison of the right hemisphere (Figure 4.12b) shows a significant contrast to the proposed model. Most of the gPDC flows to the AC, which is not suggested by the model. There is also considerable gPDC flow to the AC from the MC. On the other hand, there is agreement in gPDC flow from MC to PC and PFC, as well from AC to TC and PFC. There is not much evidence in our results, utilizing $H = 195$ trials, of flows to the MC or the PC. Flows from the TC to PFC, MC and PC are also not present in our results. The flows that are not evidenced by our results may simply not be observable with the signal under study, namely the β power envelope.

Figure 4.13 offers a guess at 2 potential configurations for auditory-motor communication. The results in the right hemisphere of Subject 3 (Figure 4.13b) indicate that the AC receives input from the MC directly as well as indirectly via the PFC. The AC also provides feedback to the PFC. On the other hand, the right hemisphere of Subject 5 (Figure 4.13d) indicates that the AC and MC have a direct bi-directional flow of information and the AC receives input from the PFC.

4.7 Conclusion

We have proposed a sparse dynamic causal network estimation algorithm tailored to the analysis of ERPs. The algorithm computes the dynamic generalized PDC based on the reflection coefficients estimated by an adaptive multi-trial multi-channel sparse online lattice filter (ASET). The use of multiple ERP trials, a sparsity constraint

and a beamforming capability increase the effective SNR of the problem and endows the algorithm with an improvement in the reflection coefficient MSE of at least one quarter of an order of magnitude over the classic MQRDLSL algorithm. The accuracy of the ASET algorithm is evidenced by surrogate data analysis and evaluation of the standard deviations of the gPDC estimates.

We evaluated the dynamic gPDC activity from ERPs elicited by a standard tone during an auditory oddball experimental protocol, focusing mainly on the β -band and its envelope. We compared this dynamic gPDC activity to a current model of human speech processing [29]. Although the model is not limited to the β -band and its envelope, the comparison yielded similarities in regions of gPDC activity as well as some of the directions of gPDC flow. There were also a few differences in the flow of gPDC that were not postulated by the model, namely the right-sided gPDC flows to the AC as well as direct gPDC flows from the left PFC to the left TC. The results also provided a much richer and dynamic view of gPDC activity than exists in the literature and provides enhanced information as to the temporal sequencing of neural activity.

Chapter 5

Future Work

5.1 rTMS Muscle Artifact Reduction

A major limitation of the work presented in Chapter 2 is that the noise reduction algorithm is developed based on data that is already ensemble averaged. The process of ensemble averaging losses information that could be useful in distinguishing between a neural EP and the CMAP. More specifically, reducing noise in the EEG produced by rTMS stimulation could be further improved by utilizing single trial measurements to develop a method based on second order statistics. In my experience, I observed that beamforming produces much lower quality results when the covariance matrix is computed from EEG data that is ensemble averaged versus single trial data.

If the above mentioned improvement could eliminate the CMAP artifact, it would be interesting to explore how the rTMS stimulus propagates through the brain. The trace of stimulated neural activity could be compared with neural fiber tracks derived from diffusion tensor imaging (DTI) data to further investigate which parts of the brain are being affected leading to more effective treatment parameters.

5.2 Robust Beamforming

There are many avenues yet to be explored in robust beamforming for ERP applications. First, a different relaxation method can be applied to the objective function to achieve a more specific definition of robustness. Second, the anisotropic uncertainty model could be improved in any number of ways. One idea is to specify the anisotropic error as the variance of a large number of MRIs with respect to the average ICBM152 template. This would produce a richer and more realistic error model and it could also be further expanded to make the model age specific.

Third, the forward head model could be specified in a probabilistic fashion. This is an extension of the idea in the previous paragraph, which models the distribution of head models only with the mean and variance. The idea can be extended to better model the distribution of head models. To make use of this model, the RMVB constraints would have also to be specified using a probabilistic approach. This formulation would optimize for the average head model error instead of the worst-case error, producing a less conservative solution. This would be a great improvement on the template MRI method of analysis.

Building on this idea, it would be interesting to see if it's feasible to build a generative model that takes a 3D scan of an individual's head shape and produces an equivalent probabilistic forward head model. With recent machine learning advances, it seems it would be quite possible [111]. These developments would make the analysis process much simpler since there would be no need for co-registration of the electrode positions to a template MRI, which can be a significant source of error. In general, improving the accuracy of the forward head model has the potential of drastically improving the accuracy of brain source localization analysis without increasing the cost.

Furthermore, without the need of an MRI in most scenarios this would significantly reduce the cost and complexity of EEG data collection and analysis.

5.3 Dynamic Connectivity Estimation

The ASET algorithm can be further extended by utilizing a group LASSO approach [86]. Group lasso assumes that a specific set of the variables being estimated are correlated, so they should be considered as a group. One option to incorporate this idea is to assume that interactions between anatomical regions are sparse. Therefore you would consider all the reflection coefficients from channel i to channel j as a group. Alternatively, a larger number of finer anatomical regions can be considered where groups can be selected by the group LASSO approach based on their correlation. Along this line of thought, sparsity constraints allow for good estimates on high dimensional data. The performance of the ASET algorithm has not been benchmarked against the size of the problem. This could yield an upper bound on the number of anatomical regions that can be considered accurately and perhaps yield some new insights on how to further improve the ASET algorithm.

Along these lines it would be ideal to not partition brain regions by anatomical regions *a priori*. Instead, brain sources produced through beamforming should be clustered based on similarities in their neural activity as well as proximity. This would define a dynamic functional map. The difficulty lies in the number of resulting clusters and the ability of the ASET algorithm to still achieve good estimates.

The accuracy of the ASET algorithm depends heavily on a good estimate of forward and backward error covariances. Improving the covariance estimation method would yield better error covariance estimates and in turn better reflection coefficient

estimates [112]–[114].

Reflection coefficients or partial directed coherence could be utilized as features in machine learning applications in neuroscience, especially to differentiate various neurological conditions, like depression and schizophrenia, or predict improvement in coma patients. Some approaches include tensor classification [115], tensor compression and then classification [116] or a kernelized support tensor machine for classification [117].

The algorithm presented in Chapter 4 is limited by its linearity — it assumes that the system under study is linear. A nonlinear approach would be able to model nonlinear interactions which are very likely to be present in the brain like cross frequency interactions [118] which are likely to have serious effects on neural processing. This could be achieved using kernel adaptive filtering [119] or Gaussian processes (GPs) [120]. Gaussian processes specifically allow for estimating a distribution over continuously-valued functions from discrete data. This is an intriguing idea not only for improving the ASET algorithm but also for brain source localization and connectivity analysis as the resulting GP model would be a continuously-valued distribution of activity. Another logical step would be to utilize probabilistic head models, described in Section 5.2, in conjunction with GPs describing the neural activity. Finally, GPs provide a probabilistic framework eliminating the need for parameter tuning as well as post-hoc verification of the results (i.e. surrogate analysis) which is very time-consuming in the case of the ASET algorithm.

Chapter 6

Conclusion

With the right advanced signal processing algorithms, much information can be extracted from EP and ERP data. This thesis details developments in three significant stages of EP and ERP signal processing which are typically sequentially dependent.

Chapter 2 presented a new method for reducing contamination from CMAPs recorded along with EEG activity during rTMS. The wavelet denoising approach offers a better alternative to digital filtering according to the RMSE. This development improves the visibility of short latency cortical activity as a result of rTMS which can be further investigated to improve stimulation parameters in rTMS and in turn improve its effectiveness as a neural stimulation modality.

In the application of brain source localization methods, especially beamforming, head modelling errors can cause significant performance degradation. The RMVB developed in Chapter 3 improves beamformer performance relative to the MVB and its regularized and eigenspace variations in the face of these head modelling errors. The RMVB specifically optimizes for the worst-case estimate of the uncertainty and sacrifices a distortionless response for robustness.

Lastly, Chapter 4 describes the Adaptive Sparse ERP Tracking (ASET) algorithm for estimating dynamic and causal networks that are involved in processing ERPs. The algorithm assumes that the brain network utilized in processing ERPs is sparse and augments its accuracy by utilizing information from multiple trials in its estimate. It also incorporates a beamformer that extracts the average brain activity over cortical patches which helps to reduce the dimensionality of the problem and improve the SNR of the signal. We further applied the ASET algorithm to investigate the dynamics in auditory processing, specifically resulting from the β -band and its envelope. The results showed many similarities to a current model of human auditory processing. It also showed causal connectivity between regions that were not identified by the model. These can serve as subjects of further investigation.

It is my hope that these contributions will help in further understanding the human brain.

Bibliography

- [1] S. Enriquez-Geppert, R. J. Huster, and C. S. Herrmann, “EEG-neurofeedback as a tool to modulate cognition and behavior: a review tutorial,” *Front. Hum. Neurosci.*, vol. 11, 2017.
- [2] P. R. Montague, R. J. Dolan, K. J. Friston, and P. Dayan, “Computational psychiatry,” *Trends in Cog. Sci.*, vol. 16, no. 1, pp. 72–80, 2012.
- [3] X.-J. Wang and J. H. Krystal, “Computational Psychiatry,” *Neuron*, vol. 84, no. 3, pp. 638–654, 2014.
- [4] M. Bamdad, H. Zarshenas, and M. A. Auais, “Application of BCI systems in neurorehabilitation: a scoping review,” *Disability and Rehabilitation: Assistive Technology*, vol. 10, no. 5, pp. 355–364, 2015.
- [5] S. Silvoni, A. Ramos-Murguialday, M. Cavinato, C. Volpato, G. Cisotto, A. Turolla, F. Piccione, and N. Birbaumer, “Brain-computer interface in stroke: a review of progress,” *Clin EEG Neurosci*, vol. 42, no. 4, pp. 245–252, 2011.
- [6] S. M. Grigorescu, T. Lüth, C. Fragkopoulos, M. Cyriacks, and A. Gräser, “A BCI-controlled robotic assistant for quadriplegic people in domestic and professional life,” *Robotica*, vol. 30, no. 3, pp. 419–431, 2012.

- [7] G. Pires, U. Nunes, and M. Castelo-Branco, “Statistical spatial filtering for a P300-based BCI: tests in able-bodied, and patients with cerebral palsy and amyotrophic lateral sclerosis,” *Journal of neuroscience methods*, vol. 195, no. 2, pp. 270–281, 2011.
- [8] G. Udovicić, A. Topić, and M. Russo, “Wearable technologies for smart environments: A review with emphasis on BCI,” in *Software, Telecommunications and Computer Networks (SoftCOM), 2016 24th International Conference On*, IEEE, 2016, pp. 1–9.
- [9] E. Dayan, N. Censor, E. R. Buch, M. Sandrini, and L. G. Cohen, “Noninvasive brain stimulation: from physiology to network dynamics and back,” *Nature neuroscience*, vol. 16, no. 7, pp. 838–844, 2013.
- [10] S. J. Luck, *An Introduction to the Event-Related Potential Technique*. MIT Press, 2005.
- [11] P. L. Nunez and R. Srinivasan, *Electric Fields of the Brain*. Oxford University Press, Jan. 2006.
- [12] J. A. Urigüen and B. Garcia-Zapirain, “EEG artifact removal—state-of-the-art and guidelines,” *J. Neural Eng.*, vol. 12, no. 3, p. 031 001, 2015.
- [13] N. Ille, P. Berg, and M. Scherg, “Artifact correction of the ongoing EEG using spatial filters based on artifact and brain signal topographies,” *J. Clin. Neurophys.*, vol. 19, no. 2, pp. 113–124, 2002.
- [14] P. Berg and M. Scherg, “Dipole modelling of eye activity and its application to the removal of eye artefacts from the EEG and MEG,” *Clin. Physics Physiol. Meas.*, vol. 12, no. A, p. 49, 1991.

- [15] T.-P. Jung, S. Makeig, C. Humphries, T.-W. Lee, M. J. Mckeown, V. Iragui, and T. J. Sejnowski, "Removing electroencephalographic artifacts by blind source separation," *Psychophysiology*, vol. 37, no. 2, pp. 163–178, 2000.
- [16] C. J. James and C. W. Hesse, "Independent component analysis for biomedical signals," *Phys. Meas.*, vol. 26, no. 1, R15, 2004.
- [17] H. Nolan, R. Whelan, and R. Reilly, "FASTER: fully automated statistical thresholding for EEG artifact rejection," *J. Neurosci. Methods*, vol. 192, no. 1, pp. 152–162, 2010.
- [18] R. D. Pascual-Marqui, C. M. Michel, and D. Lehmann, "Low resolution electromagnetic tomography: a new method for localizing electrical activity in the brain.," *Int. J. Psychophysiol.*, vol. 18, no. 1, pp. 49–65, 1994.
- [19] R. D. Pascual-Marqui, "Standardized low-resolution brain electromagnetic tomography (sLORETA): technical details.," *Methods Find. Exp. Clin. Pharmacol.*, vol. 24 Suppl D, pp. 5–12, 2002.
- [20] M. Hamalainen and R. Ilmoniemi, "Interpreting magnetic fields of the brain: minimum norm estimates," *Med. Biol. Eng. Comput.*, vol. 32, no. 1, pp. 35–42, 1994.
- [21] M. Scherg and D. V. Cramon, "Two bilateral sources of the late AEP as identified by a spatio-temporal dipole model," *Electroenceph. clin. Neurophysiol.*, vol. 62, no. 1, pp. 32–44, 1985.
- [22] B. Van Veen, W. van Drongelen, M. Yuchtman, and A. Suzuki, "Localization of brain electrical activity via linearly constrained minimum variance spatial filtering," *IEEE Trans. Biomed. Eng.*, vol. 44, no. 9, pp. 867–880, 1997.

- [23] S. Robinson and J. Vrba, "Functional neuroimaging by synthetic aperture magnetometry (SAM)," in *Proc. of the 11th Int. Conference on Biomagnetism*, 1998.
- [24] J. Gross and A. Ioannides, "Linear transformations of data space in MEG," *Phys. Med. Biol.*, vol. 44, pp. 2081–2097, 1999.
- [25] K. Sekihara and S. Nagarajan, "Application of an MEG eigenspace beamformer to reconstructing spatio-temporal activities of neural sources," *Hum. Brain Mapp.*, vol. 15, pp. 199–215, 2002.
- [26] K. Sameshima and L. A. Baccala, *Methods in Brain Connectivity Inference through Multivariate Time Series Analysis*, en. CRC Press, Mar. 2014.
- [27] E. Bullmore and O. Sporns, "Complex brain networks: graph theoretical analysis of structural and functional systems.," *Nature reviews. Neuroscience*, vol. 10, no. 3, pp. 186–98, Mar. 2009.
- [28] M. Rubinov and O. Sporns, "Complex network measures of brain connectivity: uses and interpretations.," *NeuroImage*, vol. 52, no. 3, pp. 1059–69, Sep. 2010.
- [29] J. P. Rauschecker and S. K. Scott, "Maps and streams in the auditory cortex: nonhuman primates illuminate human speech processing," *Nat Neurosci*, vol. 12, no. 6, pp. 718–724, Jun. 2009.
- [30] A. Pascual-Leone, B. Rubio, F. Pallardó, and M. D. Catalá, "Rapid-rate transcranial magnetic stimulation of left dorsolateral prefrontal cortex in drug-resistant depression," en, *The Lancet*, vol. 348, no. 9022, pp. 233–237, Jul. 1996.

- [31] S. Komssi, H. J. Aronen, J. Huttunen, M. Kesäniemi, L. Soinne, V. V. Nikouline, M. Ollikainen, R. O. Roine, J. Karhu, S. Savolainen, and R. J. Ilmoniemi, “Ipsi- and contralateral EEG reactions to transcranial magnetic stimulation,” eng, *Clin Neurophysiol*, vol. 113, no. 2, pp. 175–184, Feb. 2002.
- [32] S. Kähkönen, J. Wilenius, S. Komssi, and R. J. Ilmoniemi, “Distinct differences in cortical reactivity of motor and prefrontal cortices to magnetic stimulation,” *Clin Neurophysiol*, vol. 115, no. 3, pp. 583–588, Mar. 2004.
- [33] D. Balslev, W. Braet, C. McAllister, and R. C. Miall, “Inter-individual variability in optimal current direction for transcranial magnetic stimulation of the motor cortex,” eng, *J. Neurosci. Methods*, vol. 162, no. 1-2, pp. 309–313, May 2007.
- [34] E. M. Wassermann, “Variation in the response to transcranial magnetic brain stimulation in the general population,” eng, *Clin Neurophysiol*, vol. 113, no. 7, pp. 1165–1171, Jul. 2002.
- [35] J. Virtanen, J. Ruohonen, R. Näätänen, and R. J. Ilmoniemi, “Instrumentation for the measurement of electric brain responses to transcranial magnetic stimulation,” eng, *Med Biol Eng Comput*, vol. 37, no. 3, pp. 322–326, May 1999.
- [36] D. Veniero, M. Bortoletto, and C. Miniussi, “TMS-EEG co-registration: on TMS-induced artifact,” eng, *Clin Neurophysiol*, vol. 120, no. 7, pp. 1392–1399, Jul. 2009.

- [37] V. Nikouline, J. Ruohonen, and R. J. Ilmoniemi, “The role of the coil click in TMS assessed with simultaneous EEG,” eng, *Clin Neurophysiol*, vol. 110, no. 8, pp. 1325–1328, Aug. 1999.
- [38] V. Litvak, S. Komssi, M. Scherg, K. Hoechstetter, J. Classen, M. Zaaroor, H. Pratt, and S. Kahkonen, “Artifact correction and source analysis of early electroencephalographic responses evoked by transcranial magnetic stimulation over primary motor cortex,” eng, *Neuroimage*, vol. 37, no. 1, pp. 56–70, Aug. 2007.
- [39] E. ter Braack, B. de Jonge, and M. van Putten, “Reduction of TMS induced artifacts in EEG using principal component analysis,” *IEEE Trans. Neural Syst. Rehabil. Eng.*, vol. 21, no. 3, pp. 376–382, May 2013.
- [40] M. Hamidi, H. A. Slagter, G. Tononi, and B. R. Postle, “Brain responses evoked by high-frequency repetitive TMS: an ERP study,” *Brain Stimul*, vol. 3, no. 1, pp. 2–17, Jan. 2010.
- [41] T. Mutanen, H. Mäki, and R. J. Ilmoniemi, “The effect of stimulus parameters on TMS–EEG muscle artifacts,” *Brain Stimulation*, vol. 6, no. 3, pp. 371–376, May 2013.
- [42] H. de Bruin, G. Hasey, and J. Hemily, “Dorsolateral prefrontal cortex sensitivity to rTMS,” eng, *Conf Proc IEEE Eng Med Biol Soc*, vol. 2011, pp. 1997–2000, 2011.
- [43] R. J. Korhonen, J. C. Hernandez-Pavon, J. Metsomaa, H. Mäki, R. J. Ilmoniemi, and J. Sarvas, “Removal of large muscle artifacts from transcranial

- magnetic stimulation-evoked EEG by independent component analysis,” en, *Med Biol Eng Comput*, vol. 49, no. 4, pp. 397–407, Apr. 2011.
- [44] H. Mäki and R. J. Ilmoniemi, “Projecting out muscle artifacts from TMS-evoked EEG,” *NeuroImage*, vol. 54, no. 4, pp. 2706–2710, Feb. 2011.
- [45] J. C. Hernandez-Pavon, J. Metsomaa, T. Mutanen, M. Stenroos, H. Mäki, R. J. Ilmoniemi, and J. Sarvas, “Uncovering neural independent components from highly artifactual TMS-evoked EEG data,” *Journal of Neuroscience Methods*, vol. 209, no. 1, pp. 144–157, Jul. 2012.
- [46] H. de Bruin, M. Archambeault, T. Trinh, and G. Hasey, “Recording EEG during repetitive trans-cranial magnetic stimulation,” in *BIOSIGNALS*, 2009, pp. 265–272.
- [47] V. J. Samar, A. Bopardikar, R. Rao, and K. Swartz, “Wavelet analysis of neuroelectric waveforms: a conceptual tutorial,” eng, *Brain Lang*, vol. 66, no. 1, pp. 7–60, Jan. 1999.
- [48] I. Daubechies, *Ten lectures on wavelets*. SIAM: Society for Industrial and Applied Mathematics, 1992, vol. 61.
- [49] S. Mallat, *A wavelet tour of signal processing*. Academic Press, 1999.
- [50] D. L. Donoho and J. M. Johnstone, “Ideal spatial adaptation by wavelet shrinkage,” en, *Biometrika*, vol. 81, no. 3, pp. 425–455, Sep. 1994.
- [51] D. L. Donoho and I. M. Johnstone, “Adapting to unknown smoothness via wavelet shrinkage,” *Journal of the American Statistical Association*, vol. 90, no. 432, pp. 1200–1224, Dec. 1995.

- [52] P. Chrapka, H. de Bruin, and G. Hasey, "Application of wavelet based denoising techniques to rTMS evoked potentials," in *2012 Annual International Conference of the IEEE Engineering in Medicine and Biology Society (EMBC)*, Aug. 2012, pp. 4736–4739.
- [53] N. P. Castellanos and V. A. Makarov, "Recovering EEG brain signals: artifact suppression with wavelet enhanced independent component analysis," *eng, J. Neurosci. Methods*, vol. 158, no. 2, pp. 300–312, Dec. 2006.
- [54] G. Buzsáki and A. Draguhn, "Neuronal oscillations in cortical networks," *en, Science*, vol. 304, no. 5679, pp. 1926–1929, Jun. 2004.
- [55] G. Buzsáki and F. L. d. Silva, "High frequency oscillations in the intact brain," *Progress in Neurobiology*, High Frequency Oscillations in Cognition and Epilepsy, vol. 98, no. 3, pp. 241–249, Sep. 2012.
- [56] P. Lioumis, D. Kicić, P. Savolainen, J. P. Mäkelä, and S. Kähkönen, "Reproducibility of TMS-evoked EEG responses," *eng, Hum Brain Mapp*, vol. 30, no. 4, pp. 1387–1396, Apr. 2009.
- [57] D. Lehmann and W. Skrandies, "Reference-free identification of components of checkerboard-evoked multichannel potential fields," *Electroencephalography and Clinical Neurophysiology*, vol. 48, no. 6, pp. 609–621, Jun. 1980.
- [58] S. Baillet, J. Mosher, and R. Leahy, "Electromagnetic brain mapping," *Sig. Proc. Mag.*, vol. 18, no. 6, 2001.
- [59] J. Mosher, P. Lewis, and R. Leahy, "Multiple dipole modeling and localization from spatio-temporal MEG data," *IEEE Trans. Biomed. Eng.*, vol. 39, no. 6, pp. 541–557, 1992.

- [60] M. Ravan, J. Reilly, and G. Hasey, "Minimum Variance Brain Source Localization for Short Data Sequences," *IEEE Trans. Biomed. Eng.*, vol. 61, no. 2, pp. 535–546, 2014.
- [61] S. A. Vorobyov, A. B. Gershman, and Z.-Q. Luo, "Robust adaptive beamforming using worst-case performance optimization: A solution to the signal mismatch problem," *IEEE Sig. Proc.*, vol. 51, no. 2, pp. 313–324, 2003.
- [62] S. S. Dalal, S. Rampp, F. Willomitzer, and S. Ettl, "Consequences of EEG electrode position error on ultimate beamformer source reconstruction performance," *Front. Neurosci.*, vol. 8, pp. 1–7, 2014.
- [63] H. Cox, R. Zeskind, and M. Owen, "Robust adaptive beamforming," *IEEE Trans. Acoust., Speech, Signal Processing*, vol. 35, no. 10, pp. 1365–1376, 1987.
- [64] B. Carlson, "Covariance matrix estimation errors and diagonal loading in adaptive arrays," *IEEE Trans. Aerosp. Electron. Syst.*, vol. 24, no. 4, pp. 1–4, 1988.
- [65] D. Feldman and L. Griffiths, "A projection approach for robust adaptive beamforming," *IEEE Sig. Proc.*, vol. 42, no. 4, pp. 867–876, 1994.
- [66] R. Lorenz and S. Boyd, "Robust minimum variance beamforming," *IEEE Trans. Sig. Proc.*, vol. 53, no. 5, pp. 1684–1696, 2005.
- [67] S. Boyd and L. Vandenberghe, *Convex Optimization*. Cambridge: Cambridge University Press, 2009.
- [68] J. Lofberg, "YALMIP: A toolbox for modeling and optimization in MATLAB," in *Proc. IEEE International Symposium on Computer Aided Control Systems Design*, Taipei, Taiwan, 2004, pp. 284–289.

- [69] N. Yeung, R. Bogacz, C. B. Holroyd, and J. D. Cohen, "Detection of synchronized oscillations in the electroencephalogram: An evaluation of methods," *Psychophysiology*, vol. 41, no. 6, pp. 822–832, 2004.
- [70] M. Dümpelmann, T. Ball, and A. Schulze-Bonhage, "sLORETA allows reliable distributed source reconstruction based on subdural strip and grid recordings," *Hum. Brain Mapp.*, vol. 33, no. 5, pp. 1172–88, 2012.
- [71] F. Tadel, S. Baillet, J. C. Mosher, D. Pantazis, and R. M. Leahy, "Brainstorm: a user-friendly application for MEG/EEG analysis," *Comp. Intell. Neurosci.*, vol. 2011, pp. 1–13, 2011.
- [72] A. Gramfort, T. Papadopoulos, E. Olivi, and M. Clerc, "OpenMEEG: open-source software for quasistatic bioelectromagnetics," *Biomed. Eng. Online*, vol. 9, no. 45, pp. 1–20, 2010.
- [73] J. Capon and N. R. Goodman, "Probability distributions for estimators of the frequency-wavenumber spectrum," *Proc. IEEE*, vol. 58, no. 10, pp. 1785–1786, 1970.
- [74] T. C. Liu and B. van Veen, "Multiple window based minimum variance spectrum estimation for multidimensional random fields," *IEEE Trans. Sig. Proc.*, vol. 40, no. 3, pp. 578–589, 1992.
- [75] P. Berg and M. Scherg, "A fast method for forward computation of multiple-shell spherical head models," *Electroenceph. clin. Neurophysiol.*, vol. 90, no. 1, pp. 58–64, 1994.

- [76] A. H. Nuttall, "Multivariate linear predictive spectral analysis employing weighted forward and backward averaging: A generalization of Burg's algorithm," DTIC Document, Tech. Rep., 1976.
- [77] O. Strand, "Multichannel complex maximum entropy (autoregressive) spectral analysis," *IEEE Transactions on Automatic Control*, vol. 22, no. 4, pp. 634–640, Aug. 1977.
- [78] J. P. Burg, "Maximum entropy spectral analysis.," in *37th Annual International Meeting.*, Society of Exploration Geophysics, 1967.
- [79] B. Friedlander, "Lattice filters for adaptive processing," *Proceedings of the IEEE*, vol. 70, no. 8, pp. 829–867, Aug. 1982.
- [80] J. A. Apolinário, Ed., *QRD-RLS Adaptive Filtering*, en. Springer US, 2009.
- [81] M. Ding, S. L. Bressler, W. Yang, and H. Liang, "Short-window spectral analysis of cortical event-related potentials by adaptive multivariate autoregressive modeling: data preprocessing, model validation, and variability assessment," en, *Biol Cybern*, vol. 83, no. 1, pp. 35–45, Jun. 2000.
- [82] E. Möller, B. Schack, M. Arnold, and H. Witte, "Instantaneous multivariate EEG coherence analysis by means of adaptive high-dimensional autoregressive models," *Journal of Neuroscience Methods*, vol. 105, no. 2, pp. 143–158, Feb. 2001.
- [83] L. Astolfi, F. Cincotti, D. Mattia, F. De Vico Fallani, A. Tocci, A. Colosimo, S. Salinari, M. Marciani, W. Hesse, H. Witte, M. Ursino, M. Zavaglia, and F. Babiloni, "Tracking the Time-Varying Cortical Connectivity Patterns by

- Adaptive Multivariate Estimators,” *IEEE Transactions on Biomedical Engineering*, vol. 55, no. 3, pp. 902–913, Mar. 2008.
- [84] T. Milde, L. Leistritz, L. Astolfi, W. H. R. Miltner, T. Weiss, F. Babiloni, and H. Witte, “A new Kalman filter approach for the estimation of high-dimensional time-variant multivariate AR models and its application in analysis of laser-evoked brain potentials,” *NeuroImage*, vol. 50, no. 3, pp. 960–969, Apr. 2010.
- [85] L. Sommerlade, M. Thiel, B. Platt, A. Plano, G. Riedel, C. Grebogi, W. Mader, M. Mader, J. Timmer, and B. Schelter, “Time-Variant Estimation of Connectivity and Kalman Filter,” in *Methods in Brain Connectivity Inference through Multivariate Time Series Analysis*, CRC Press, 2014, pp. 161–177.
- [86] A. Bolstad, B. D. V. Veen, and R. Nowak, “Causal Network Inference Via Group Sparse Regularization,” *IEEE Transactions on Signal Processing*, vol. 59, no. 6, pp. 2628–2641, Jun. 2011.
- [87] S. Haufe, K.-R. Mueller, G. Nolte, and N. Kraemer, “Sparse Causal Discovery in Multivariate Time Series,” in *JMLR Workshop and Conference Proceedings*, vol. 6, 2008.
- [88] L. A. Baccalá and K. Sameshima, “Partial directed coherence: a new concept in neural structure determination,” *en, Biol Cybern*, vol. 84, no. 6, pp. 463–474, May 2001.
- [89] L. A. Baccala, K. Sameshima, and D. Y. Takahashi, “Generalized Partial Directed Coherence,” in *2007 15th International Conference on Digital Signal Processing*, Jul. 2007, pp. 163–166.

- [90] J. Durbin, "The Fitting of Time-Series Models," *Revue de l'Institut International de Statistique / Review of the International Statistical Institute*, vol. 28, no. 3, pp. 233–244, 1960.
- [91] S. L. Marple, *Digital Spectral Analysis: With Applications*. Prentice-Hall Englewood Cliffs, NJ, 1987, vol. 5.
- [92] S. Haykin and S. Kesler, "Prediction-error filtering and maximum-entropy spectral estimation," in *Nonlinear Methods of Spectral Analysis*, Springer, 1979, pp. 9–72.
- [93] P. Lewis, "QR-based algorithms for multichannel adaptive least squares lattice filters," *IEEE Transactions on Acoustics, Speech and Signal Processing*, vol. 38, no. 3, pp. 421–432, Mar. 1990.
- [94] B. Yang and J. F. Bohme, "Rotation-based RLS algorithms: unified derivations, numerical properties, and parallel implementations," *IEEE Transactions on Signal Processing*, vol. 40, no. 5, pp. 1151–1167, May 1992.
- [95] D. Angelosante, J. A. Bazerque, and G. B. Giannakis, "Online Adaptive Estimation of Sparse Signals: Where RLS Meets the ℓ_1 -Norm," *IEEE Transactions on Signal Processing*, vol. 58, no. 7, pp. 3436–3447, Jul. 2010.
- [96] J. W. Taylor, "Exponentially weighted information criteria for selecting among forecasting models," *International Journal of Forecasting*, vol. 24, no. 3, pp. 513–524, Jul. 2008.
- [97] K. Buckley, "Spatial/Spectral filtering with linearly constrained minimum variance beamformers," *IEEE Transactions on Acoustics, Speech, and Signal Processing*, vol. 35, no. 3, pp. 249–266, Mar. 1987.

- [98] J. Mazziotta, A. Toga, A. Evans, P. Fox, J. Lancaster, K. Zilles, R. Woods, T. Paus, G. Simpson, B. Pike, C. Holmes, L. Collins, P. Thompson, D. MacDonald, M. Iacoboni, T. Schormann, K. Amunts, N. Palomero-Gallagher, S. Geyer, L. Parsons, K. Narr, N. Kabani, G. L. Goualher, D. Boomsma, T. Cannon, R. Kawashima, and B. Mazoyer, “A probabilistic atlas and reference system for the human brain: International Consortium for Brain Mapping (ICBM),” *Philosophical Transactions of the Royal Society B: Biological Sciences*, vol. 356, no. 1412, pp. 1293–1322, Aug. 2001.
- [99] S. Cutini, P. Scatturin, and M. Zorzi, “A new method based on ICBM152 head surface for probe placement in multichannel fNIRS,” *NeuroImage*, vol. 54, no. 2, pp. 919–927, Jan. 2011.
- [100] R. Oostenveld, P. Fries, E. Maris, and J.-M. Schoffelen, “FieldTrip: Open source software for advanced analysis of MEG, EEG, and invasive electrophysiological data,” *Computational intelligence and neuroscience*, vol. 2011, p. 156 869, Jan. 2011.
- [101] T. Limpiti, B. D. V. Veen, and R. T. Wakai, “Cortical patch basis model for spatially extended neural activity,” *IEEE Transactions on Biomedical Engineering*, vol. 53, no. 9, pp. 1740–1754, Sep. 2006.
- [102] S. S. Haykin, *Adaptive Filter Theory*, 4th. Prentice Hall, 2001.
- [103] J. Theiler, S. Eubank, A. Longtin, B. Galdrikian, and J. D. Farmer, “Testing for nonlinearity in time series: the method of surrogate data,” *Physica D: Nonlinear Phenomena*, vol. 58, no. 1-4, pp. 77–94, 1992.

- [104] B. Schelter, M. Winterhalder, M. Eichler, M. Peifer, B. Hellwig, B. Guschlbauer, C. H. Lücking, R. Dahlhaus, and J. Timmer, “Testing for directed influences among neural signals using partial directed coherence.,” *Journal of neuroscience methods*, vol. 152, no. 1-2, pp. 210–9, Apr. 2006.
- [105] L. Faes, G. D. Pinna, A. Porta, R. Maestri, and G. Nollo, “Surrogate data analysis for assessing the significance of the coherence function,” *IEEE transactions on biomedical engineering*, vol. 51, no. 7, pp. 1156–1166, 2004.
- [106] C. Wilke, L. Ding, and B. He^{ast\$}, “Estimation of Time-Varying Connectivity Patterns Through the Use of an Adaptive Directed Transfer Function,” *IEEE Transactions on Biomedical Engineering*, vol. 55, no. 11, pp. 2557–2564, Nov. 2008.
- [107] L. Faes, H. Zhao, K. H. Chon, and G. Nollo, “Time-varying surrogate data to assess nonlinearity in nonstationary time series: application to heart rate variability,” *IEEE transactions on biomedical engineering*, vol. 56, no. 3, pp. 685–695, 2009.
- [108] T. Fujioka, L. J. Trainor, E. W. Large, and B. Ross, “Internalized Timing of Isochronous Sounds Is Represented in Neuromagnetic Beta Oscillations,” en, *J. Neurosci.*, vol. 32, no. 5, pp. 1791–1802, Feb. 2012.
- [109] A. Chang, D. J. Bosnyak, and L. J. Trainor, “Unpredicted Pitch Modulates Beta Oscillatory Power during Rhythmic Entrainment to a Tone Sequence,” *Front Psychol*, vol. 7, Mar. 2016.
- [110] N. Tzourio-Mazoyer, B. Landeau, D. Papathanassiou, F. Crivello, O. Etard, N. Delcroix, B. Mazoyer, and M. Joliot, “Automated Anatomical Labeling of

- Activations in SPM Using a Macroscopic Anatomical Parcellation of the MNI MRI Single-Subject Brain,” *NeuroImage*, vol. 15, no. 1, pp. 273–289, Jan. 2002.
- [111] D. J. Rezende, S. A. Eslami, S. Mohamed, P. Battaglia, M. Jaderberg, and N. Heess, “Unsupervised learning of 3d structure from images,” in *Advances in Neural Information Processing Systems*, 2016, pp. 4996–5004.
- [112] Y. Chen, A. Wiesel, Y. C. Eldar, and A. O. Hero, “Shrinkage algorithms for MMSE covariance estimation,” *IEEE Trans. Sig. Proc.*, vol. 58, no. 10, pp. 5016–5029, 2010.
- [113] Y. Chen, A. Wiesel, and A. O. Hero, “Robust shrinkage estimation of high-dimensional covariance matrices,” *IEEE Trans. Sig. Proc.*, vol. 59, no. 9, pp. 4097–4107, 2011.
- [114] D. Bartz and K.-R. Müller, “Covariance shrinkage for autocorrelated data,” in *Advances in Neural Information Processing Systems 27*, Z. Ghahramani, M. Welling, C. Cortes, N. D. Lawrence, and K. Q. Weinberger, Eds., Curran Associates, Inc., 2014, pp. 1592–1600.
- [115] X. Guo, X. Huang, L. Zhang, L. Zhang, A. Plaza, and J. A. Benediktsson, “Support tensor machines for classification of hyperspectral remote sensing imagery,” *IEEE Trans. Geosci. Remote Sens.*, vol. 54, no. 6, pp. 3248–3264, 2016.
- [116] J. A. Bengua, P. N. Ho, H. D. Tuan, and M. N. Do, “Matrix Product State for Higher-Order Tensor Compression and Classification,” *IEEE Trans. Sig. Proc.*, vol. 65, no. 15, pp. 4019–4030, 2016.

- [117] L. He, C.-T. Lu, G. Ma, S. Wang, L. Shen, S. Y. Philip, and A. B. Ragin, “Kernelized support tensor machines,” in *International Conference on Machine Learning*, 2017, pp. 1442–1451.
- [118] O. Jensen and L. L. Colgin, “Cross-frequency coupling between neuronal oscillations,” *Trends in cognitive sciences*, vol. 11, no. 7, pp. 267–269, 2007.
- [119] W. Liu, J. C. Principe, and S. Haykin, *Kernel Adaptive Filtering: A Comprehensive Introduction*. John Wiley & Sons, 2011, vol. 57.
- [120] C. K. Williams and C. E. Rasmussen, *Gaussian Processes for Machine Learning*. 2006, vol. 2.